ABSTRACT

Title of dissertation: PROBING THE CENTRAL REGIONS
OF ACTIVE GALACTIC NUCLEI

Anne Maria Lohfink, Doctor of Philosophy, 2014

Dissertation directed by: Professor Christopher S. Reynolds
Department of Astronomy

Active Galactic Nuclei (AGN) are one of the key players in the Universe. Their energy output can strongly affect the growth of their host galaxy and can promote or suppress star formation on galactic scales. Most of the processes that determine the power of an AGN as well as the form in which that power is released take place in the immediate surroundings of its supermassive black hole, a region that is still not entirely understood. A comprehension of these inner regions is, however, crucial to any ultimate understanding of the AGN's vast influence. This dissertation explores these close-in environments of the black hole using two approaches: X-ray spectroscopy and variability studies.

We begin by summarizing our current understanding of why AGN play such a significant role in galaxy formation. This is followed by a discussion of why X-ray spectroscopy is one of the best means to investigate them. We point out that, in particular, the X-ray reflection spectrum is interesting as it can directly probe parameters such as the black hole spin or the inclination of the accretion disk. Since the reflection spectrum is a broad band component, that usually only contributes a fraction of the total observed X-ray flux, the entire X-ray spectrum requires careful modeling.

To perform such modeling and gain access to the parameters of the reflection spectrum, we first select a target in which the spectral decomposition is simplified by the absence of absorption – the Seyfert 1 galaxy Fairall 9. We apply a multi-epoch fitting method that uses more than one spectrum at a time to get the best possible results on the parameters of the reflection spectrum that are invariant on human timescales. This technique enables us to tightly constrain the reflection parameters and leads us to conclude that Fairall 9 most likely possesses a composite soft X-ray excess, consisting of blurred reflection and a separate component such as Comptonization.

The reflection spectrum also provides a way to enhance our knowledge of jet formation. We present a multi-wavelength study of the broad line radio galaxy 3C120 centered around a study of the reflection spectrum from two *Suzaku* and one *XMM* observation. Our results confirm that jet formation is linked to changes in (and possibly the destruction of) the inner accretion disk, and the high measured spin suggests that the rotational energy could very well be the energy source required to launch the jet.

Finally, we present results from variability studies, which present another window into the processes taking place close to the black hole. A 10 year *RXTE* monitoring of Fairall 9 allows us to discover very rapid flux dips in the X-ray band which only last 5-15 days. While we are unable to determine the exact nature of the dips, we discuss a range of possible models, including the idea that the accretion disk in this radio-quiet AGN may be undergoing sporadic disruptions (via some yet-to-be-determined global instability) in much the same manner as is inferred to occur in 3C120 and other broad-line galaxies. Lastly we turn to the UV variability of Fairall 9 and its connection to the X-ray variability. From 2.5 months of *Swift* monitoring, we find that Fairall 9 shows significant variability on 4 day timescales, and the analysis of *XMM*-OM data shows that variability is present even on the time scales of hours. Folding in the X-ray variability, we determined that this fast UV variability can be explained as reprocessing of X-rays. We conclude by explaining how these studies fit into the field of AGN science as a whole and how they can be followed up with future observations.

PROBING THE CENTRAL REGIONS OF ACTIVE GALACTIC NUCLEI

by

Anne Maria Lohfink

Dissertation submitted to the Faculty of the Graduate School of the
University of Maryland, College Park in partial fulfillment
of the requirements for the degree of
Doctor of Philosophy
2014

Advisory Committee:
Professor Christopher S. Reynolds, Chair/Advisor
Professor Michael Boylan-Kolchin
Professor Jon M. Miller
Professor Richard F. Mushotzky
Professor Peter Shawhan
Professor Sylvain Veilleux

Preface

The work presented in Chapters 2 and 3 has been published in the *Astrophysical Journal*(Lohfink et al., 2012b, 2013), while Chapter 4 has been published in the *Astrophysical Journal Letters* (Lohfink et al., 2012a). The last Chapter has also been accepted for publication in the *Astrophysical Journal.* The *Suzaku* data mostly come from the AGN Spin Key Project (PI: Reynolds). The *Swift* data presented in Chapters 3 and 5 were obtained through the *Swift* ToO program. We were able to obtain the VLBA data of 3C120 through a collaboration with Alan Marscher from Boston University. Finally, all other data were taken from the HEASARC data archives.

To my family

Acknowledgments

As I sit here in front of my completed thesis, it is time to extend some thanks. I know I will forget someone, so if you're the one – I'm so sorry!

First of all, I am deeply grateful to my advisor, Chris Reynolds, without whom this thesis wouldn't have been possible. He taught me almost everything I needed to know about research, writing papers, and proposals, i.e. begging for money. His encouragement has been invaluable many times. He has given me enough freedom in my research to pursue my pet ideas[1], and has always remained graceful and professional even when presented with the dumbest ideas possible. He has sacrificed a lot of his travel money to let me go on adventures, which I will never forget. Honestly, there's so much more to say but other people also deserve their turn, so let's summarize: Thanks, Chris!!

Thanks also to Richard Mushotzky for lots of excellent advice and enough ideas to last for a good portion of my scientific career. I haven't forgotten about that *RXTE* data, it's on my list... I am also grateful to have had such encouraging advisors, in Katja Pottschmidt and Jörn Wilms, during my undergrad/early grad years, who not only introduced me to X-ray Astronomy research, but also sparked the flame of curiosity that carried me through the last few years of hard work. In general, every result presented in this thesis has benefited from the input of my collaborators and I would therefore like to thank all of them for sharing their great ideas with me. Special thanks to all the current and former members of UMd's 'X-ray group', who have made research more fun and helped me out so many times.

---

[1] Yes, little idea, your day will come soon... *stroke*

Many thanks to the rest of the Astronomy Department for providing such a welcoming environment and, especially, to my officemates, Ron Ballouz, Gabrielle Betancourt-Martinez, Jithin George, Kari Helgason, Taro Shimizu, and Ashlee Wilkins for enduring me during the thesis writing process. Thanks to all the now 5th years for fighting through the second year project and qualifier with me. Much appreciated are also the 'Espresso Time' and its usual participants. I would also like to thank the baby horse 'Pax' for much needed distraction.

Thanks to my roommates for many nice kitchen chats. Thanks to Camille and Mark Herrera for hosting the best Settlers of Catan parties ever, and for being good friends. Thanks also to Jon(athan) Fraine and Jithin George (again) for being such great friends and gym buddies/roommates/drivers/whatever.

I thank my family for the support and encouragement they have provided me throughout my entire life and, in particular, over the last five years.

Finally, I am very much indebted to Owen for making life a lot more enjoyable, keeping me calm during the last few weeks, cheering me up when I fell into the lava 50 times, lots of proof-reading and so much more.

Table of Contents

List of Tables

List of Figures

List of Abbreviations

R_g	gravitational radius
AGN	active galactic nuclei
BLR	broad-line region
BLRG	broad-line radio galaxy
ISCO	innermost stable circular orbit
NLR	narrow-line region
NLRG	narrow-line radio galaxy
RLAGN	radio-loud AGN
SED	spectral energy distribution
VLBA	Very Long Baseline Array
XRB	X-ray binary system

Chapter 1: Introduction

Supermassive black holes with masses of a few ten-thousands to a billion solar masses can be found in the center of many galaxies and provide the opportunity to study a wealth of physical phenomena. While only mass and angular momentum (black hole spin) are needed to describe an astrophysical black hole, the immediate surrounding of the black hole provides an ideal laboratory to study effects of plasma physics, general relativity and magnetohydrodynamics.

From an astrophysical standpoint, studying the surrounding of the supermassive black hole is a crucial first step in our exploration of how the black hole is able to affect the evolution of its host galaxy (§1.1) as it grows over time (§1.3).

When a supermassive black hole is accreting significant quantities of gas from its surroundings, the release of gravitational energy powers enormous radiative and kinetic luminosities. Such objects are called active galactic nuclei (AGN), and are the ideal places to study black holes and the black hole related processes that are important for galaxy evolution.

1.1 The Importance of AGN Feedback to Galaxy Evolution

One of the major open questions in Astrophysics today is how galaxies evolve through cosmic time. One of the ways that this question has been tackled is through large-scale, numerical computer simulations, which aim to reproduce the observable characteristics of the Universe today, by using the fluctuations in the microwave background as a starting point. One of the key observations that the simulations try to match is the observed galaxy stellar mass function (Fig. 1.1). It has been shown (e.g., Bower et al., 2006; Croton et al., 2006), that this is only possible when the interaction between the black hole and its galaxy is accounted for in the simulations. This process, referred to as AGN feedback, plays a crucial role in suppressing the high-mass end of the galaxy stellar mass function. Galaxy formation models that do not include AGN feedback vastly overproduce high mass galaxies, and furthermore, produce high mass galaxies that today are actively star forming (whereas massive galaxies in the real universe typically have very little ongoing star formation). These issues are solved by assuming that AGN inject energy into the most massive galaxies, suppressing cooling and star formation.

The AGN has several ways of interacting with its surrounding galaxy: radiation, outflowing winds and its powerful jets. There are two well known modes of AGN feedback, the kinetic mode and the radiative mode (Fabian, 2012). In the kinetic mode, which is mostly observed in giant ellipticals in the center of galaxy clusters, the jet plows into the ISM and blows large bubbles into it (Best et al., 2005; Rafferty et al., 2006; Fabian et al., 2011). The heating of the intra-cluster gas prevents cooling and so quenches star formation. The other well-established mode is the radiative mode, which dominates when the accretion rate is high and close to or at the Eddington limit. The high accretion rate produces a significant radiation pressure that pushes the dust and gas outward and regulates the infall of matter onto the black hole (Silk & Rees, 1998). Dust boosts the influence of the radiation pressure, enhancing the impact on the galaxy (Murray et al., 2005). This mode is most likely responsible for the observed $M - \sigma$ relation (Kormendy & Gebhardt, 2001) between the black hole mass and the stellar velocity dispersion. As part of the radiative mode, winds can be formed which can exceed those driven by stellar feedback in terms of speed and momentum (Veilleux et al., 2005; Feruglio et al., 2010; Sturm & et al., 2011; Higginbottom et al., 2014).

Recently, it has been suggested that there is possibly a positive jet-induced feedback, which triggers star formation (Silk, 2013). The observational evidence for this so far is sparse however (Croft et al., 2006; Dugan et al., 2014).

1.2 The Physics of AGN

Not all AGN are alike; AGN display a large variety of phenomena and properties (Singh, Shastri & Risaliti, 2011). The unified AGN model attempts to explain much of this diversity as a viewing angle effect (Antonucci, 1993; Urry & Padovani, 1995). Figure 1.2 shows the basic assumed structure and components of an AGN. The current paradigm is built around a supermassive black hole with an accretion disk surrounding it. Relatively dense gas clouds ($n_e \sim 10^9\,\mathrm{cm}^{-3}$) at distances of a

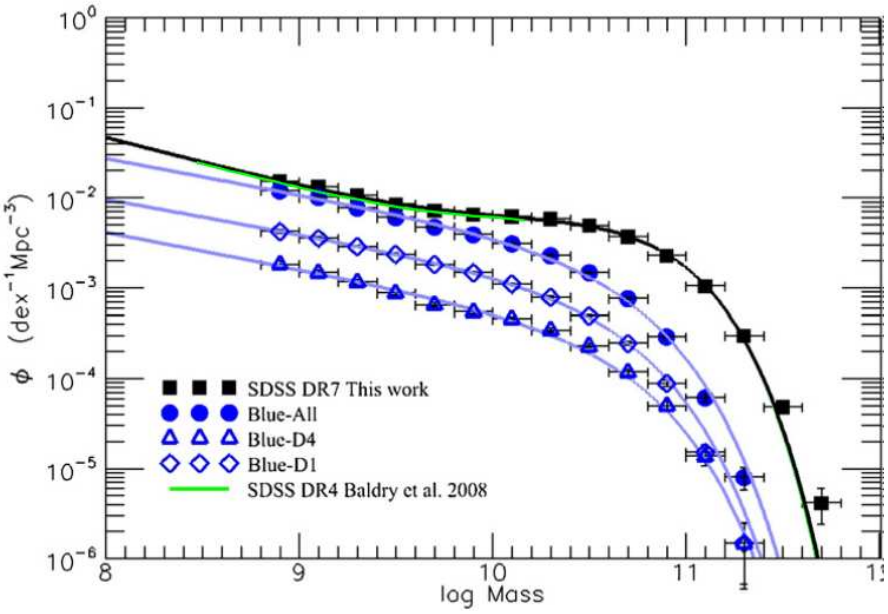

Figure 1.1: The galaxy mass function of all SDSS 7 galaxies [black line] from Peng et al. (2010) with a green line overplotted showing the results for the total galaxy mass function from Baldry et al. (2008). The blue lines indicate the galaxy mass function for only blue galaxies and their environments.

few thousand to ten thousand gravitational radii $\left(1\,R_{\rm g} = \frac{GM}{c^2}\right)$ produce the broad emission lines ($v \sim 1000 - 25,000\,\mathrm{km\,s^{-1}}$) seen in the UV–optical spectra of AGN (Peterson, 2006). This region is called the broad-line region (BLR). Further out there is a dusty torus that is opaque to most radiation. This torus can obstruct the accretion disk and broad-line region from the direct view of external observers in the torus plane. The torus absorbs radiation from the central source and reemits this energy in the infrared, i.e. reprocesses parts of the radiation. More recent results indicate that this torus is not one uniform structure but is of a clumpy nature (e.g., Nenkova et al., 2008; Mor et al., 2009). Narrow emission lines ($v \sim 500\,\mathrm{km\,s^{-1}}$) arise in low-density clouds ($n_e \sim 10^3\,\mathrm{cm^{-3}}$) at several parsecs, and beyond, that are photoexcited by the central engine (Peterson, 2006). This region is called the narrow-line region (NLR).

In addition to the structure described so far, some fraction of AGN possess relativistic jets that emerge along the disk axis. Given that these jets are powerful sources of radio emission, this property divides AGN into two possibly fundamental classes: radio-loud and radio-quiet (Kellermann et al., 1989).

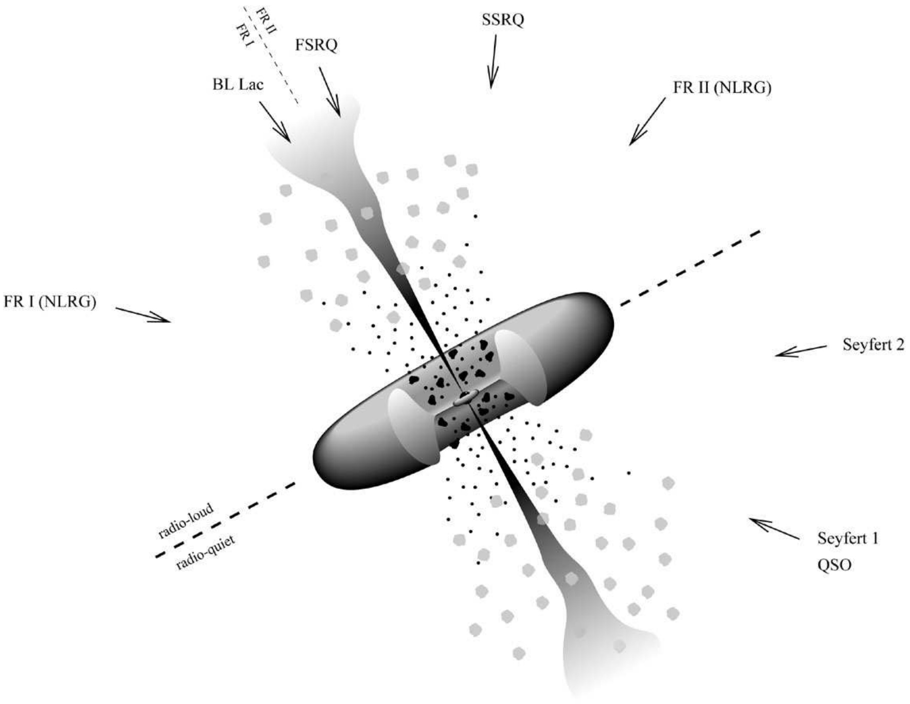

Figure 1.2: Standard Unified AGN model taken from `http://ned.ipac.caltech.edu/level5/March04/Torres/Torres2_4.html`, where the black blobs represent the broad line region and the grey ones the narrow line region.

The best known unification model is the one for Seyfert galaxies, which display two spectroscopic classes. There are those with both narrow and broad emission IR/optical/UV lines (Type 1) and those with narrow lines only (Type 2). The unification model says that Type 2s are intrinsically Type 1s whose continuum and broad-line emission is attenuated in the direction of the observer. In other words, Seyfert 2 galaxies are edge-on Seyfert 1 galaxies where the torus obscures our direct view of the broad emission-line region and the accretion disk, as illustrated in Figure 1.2. Direct evidence for this idea comes from the detection of broad lines in the spectrum of polarized (i.e. scattered) light from Seyfert 2s (Antonucci & Miller, 1985; Heisler, Lumsden & Bailey, 1997; Moran et al., 2000). The vast majority of Seyfert galaxies are mostly radio-quiet, i.e. do not show a strong jet, although an increasing number of weaker jets have been detected (Ho & Ulvestad, 2001; Abdo et al., 2009).

A similar unification scheme explains the difference between 'broad-line radio galaxies' (BLRGs), which might be described to first-order accuracy as radio-loud Seyfert 1s, and 'narrow-line radio galaxies' (NLRGs), which correspond to Seyfert 2s (Barthel, 1989). However, some NLRGs are thought to genuinely lack any kind of BLR.

Other unification schemes for different types of AGN exist but are not relevant for this thesis and shall therefore not be discussed here.

1.3 Studying the AGN & the Black Hole Spin

1.3.1 The X-ray spectrum

X-ray spectroscopy (and spectral variability) provides one of the best tools for studying the properties of astrophysical black holes and the regions very close to them.

In a normal Seyfert-type AGN most of the X-ray emission is thought to be produced by the inverse Compton scattering (Comptonization) of thermal, UV/optical photons from the accretion disk by hot electrons with temperatures of 10-100 keV. These hot electrons are part of the accretion disk corona (Haardt & Maraschi, 1991), whose nature, geometry, optical depth and temperature remain largely unknown to-date. Several geometries have been suggested: the corona could be located above and below the disk plane in a plane parallel slab geometry (Poutanen & Svensson, 1996; Beloborodov, 1999), it could be at the base of a possible jet (Markoff, Nowak, & Wilms, 2005), or of spherical shape inside a truncated disk (Dove et al., 1997). While the precise geometry is not known at current times, all observational evidence points at the corona being located very close to the black hole (Chartas et al., 2009; Reis & Miller, 2013). The thermal Comptonization produces a power law spectrum throughout the X-ray band and, at high energies, a quasi-exponential cut-off with $E_{\rm c} \sim 2-3 \times kT_{\rm e^-}$ is expected (Rybicki & Lightman, 1979). The recent launch of the focusing hard X-ray mission *NuSTAR* now enables us to obtain reliable measurements of the high energy cut-off, i.e. coronal temperature, from single observations. First results from *NuSTAR* (Brenneman et al., 2014; Matt et al., 2014) are consistent with previous results, which indicate that the AGN show a wide range of cut-off energies (e.g., Perola et al., 2002; Beckmann et al., 2008; de Rosa et al., 2012; Molina et al., 2013). The reason for this wide spread is currently unknown.

Of great interest is also the so-called X-ray "reflection", i.e. the backscattering of the hard X-rays and line emission that results when the hard X-ray continuum irradiates the accretion disk and the AGN's torus (Fabian et al., 1989; Reynolds & Nowak, 2003; Miller, 2007). The only well-developed technique at the current time for measuring the spin of a supermassive black hole utilizes the shape of this reflection spectrum and, in particular, of the iron Kα line at 6.4 keV, the most prominent feature in a reflection spectrum (Fig. 1.3). The basic X-ray spectral components of an AGN are pointed out in Figure 1.4. In addition to the primary continuum and reflection spectrum, another component of an AGN spectrum is the soft X-ray excess, which is observed below about 1 keV and whose origin is not understood to date (Dewangan et al., 2007). Over the last decades there has been a debate about what is producing this excess and there are many distinct ideas as to its physical nature. While the most popular ideas are blurred ionized reflection from the inner parts of the accretion disk (Gierliński & Done, 2004; Crummy et al., 2006) and additional Comptonization components (Ross et al., 1992) many more have been proposed. For radio-loud objects and narrow line Seyferts an additional power law or broken power law can describe the soft excess rather well (Kataoka et al., 2007). Physically this power law component can be associated with an optically thick Comptonization component (Papadakis et al., 2010) or a jet component (Chatterjee et al., 2009).

The determination of the exact nature of the soft excess is further complicated as the observed X-ray spectrum can be modified by the emission, scattering and absorption from accretion disk winds (or any other optically-thin plasma in the circumnuclear environment) on a range of spatial scales. Most dramatic are the warm absorbers seen in approximately 50% of local type-1 AGN (Reynolds, 1997;

George et al., 1998). These complex absorbing structures have led to considerable uncertainty in the detection of reflection in some sources (Gofford et al., 2011; Tatum et al., 2012; Miller & Turner, 2013), especially if partial covering of the X-ray emitting region by the absorber is permitted, as such models can be partially degenerate with disk reflection in the X-ray band below 10 keV.

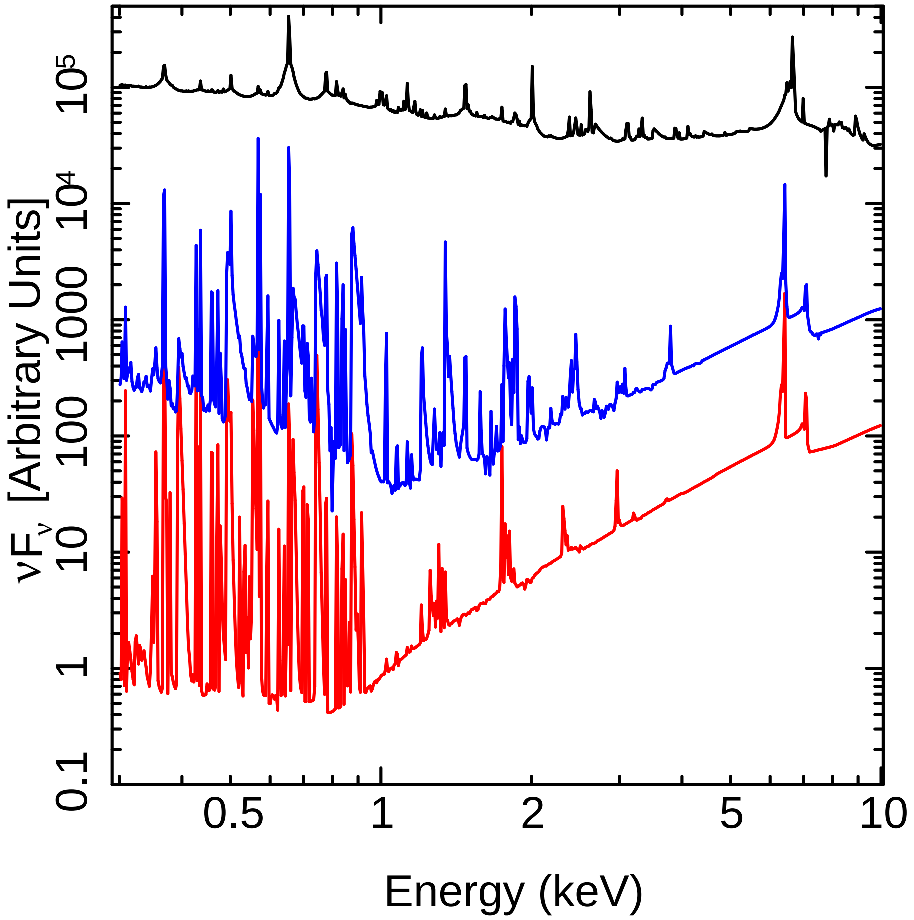

Figure 1.3: Exemplary X-ray reflection spectra are shown, as calculated by García et al. (2013), with solar abundances, an inclination angle of 45 degrees and varying ionization states ($\log(\xi) = 0.5, 1.5, 3.0$ [red, blue, black]). The normalization of the spectra is varied for better plot clarity.

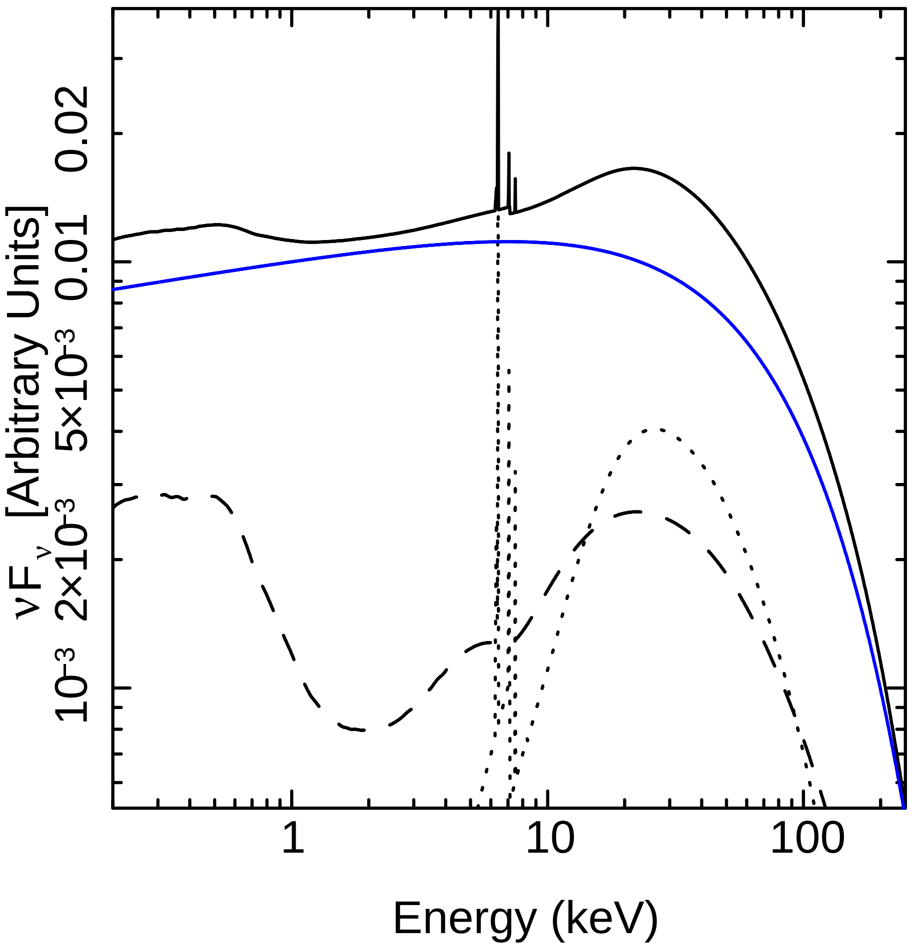

Figure 1.4: Exemplary X-ray spectrum of a Seyfert 1 galaxy, shown are the continuum Comptonization component [solid blue], the ionized reflection component from the inner accretion disk distorted by relativistic effects [dashed black], the cold reflection component from the torus [dotted black], and the complete model spectrum [solid black].

1.3.2 Features of the reflection spectrum

Although obtaining a precise measurement of the reflection spectrum is not easy, it is worthwhile because of the importance of the black hole spin. The spin is not only one of two fundamental parameters describing a black hole but it also provides the only major source of energy close to a black hole other than accretion.

Its magnitude is crucial to the understanding of, the creation of jets, which could be powered by the rotational energy (Blandford & Znajek, 1977). Moreover, the spin distribution in case of supermassive black holes might be a useful tool to probe galaxy evolution as the spin of a supermassive black hole can evolve over time, generally being spun-up by prolonged gas accretion and being spun-down by mergers and chaotic accretion (Volonteri, 2010; Volonteri et al., 2013).

Since the first detections of relativistically skewed iron lines, indicating the presence of ionized reflection from the inner accretion disk, with the *ASCA* satellite (Mushotzky et al., 1995; Tanaka et al., 1995), many sources were found to contain relativistic lines (Nandra et al., 1997, 2007). More recently even a broad iron L-line, which is harder to detect than the iron K-line, was discovered in the spectrum of 1 H0707-495 in addition to the iron Kα line (Fabian et al., 2009). Such high quality data allows a detailed study of the reflection spectrum and therefore black hole spin, described by the dimensionless spin parameter:

$$a = \frac{c\,J}{G\,M^2}\,, \tag{1.1}$$

where J is the angular momentum of the black hole and M its mass. The parameter can take values between a maximum prograde[1] spin of 0.998 and a maximum retrograde spin of -0.998 (Thorne, 1974). The constraint on the spin originates from the dependence of the innermost stable circular orbit (ISCO) of the black hole on the spin. The higher the spin the smaller the ISCO and for a maximally prograde spinning black hole $R_{\mathrm{ISCO}} = R_{\mathrm{g}}$. For the line profile, this is of importance as the

---

[1] Prograde spin means the accretion disk and the black hole rotate in the same direction.

ISCO determines the maximal gravitational redshift that the red wing of the line can have, or in other words, the ISCO determines how far the red wing of the line extends. This assumes the disk extends down to the ISCO at any given time and the radiation originates only from outside the ISCO and not from within the plunging region. Simulations of magneto-hydrodynamic accretion disks show this is mostly correct for astrophysical black holes (Reynolds & Fabian, 2008). The truncation of the blue wing of the broad line is determined by the inclination of the accretion disk. The emissivity profile of the disk can be estimated from the Novikov-Thorne disk model by assuming that the emissivity follows the radial dissipation profile of the disk; however the validity of the Novikov-Thorne profile for the coronal irradiation is uncertain and there are still a variety of uncertainties affecting our understanding of the accretion disk, so the emissivity profile is commonly modeled as a broken power law with the indexes q_1 and q_2. This leads to a model independent result. The emissivity index (in case of a power law) or even more generally the profile of the emissivity of the disk influences the strength of the two peaks of the iron line as well as their shape. If the emissivity index is low the outer parts of the disk have a greater weight than the central parts, i.e. the peaks appear more pointy. An example of a relativistic iron line, outlining its different parts, is shown in Fig. 1.5. Measuring the spin and other accretion disk parameters from the relativistic line is in principle a model-independent technique as the shape of the line is independent of the underlying continuum. However, in reality it is more complex as the very extended wings of the broad line can easily be mistaken to be continuum or vice-versa.

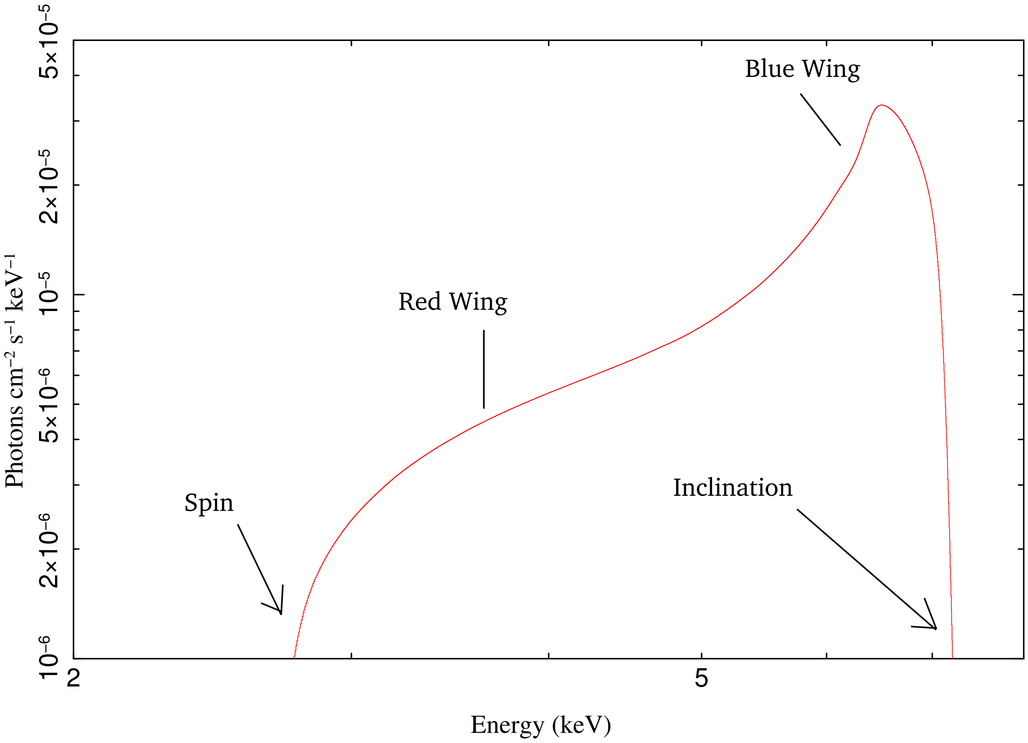

Figure 1.5: Unfolded sample model spectrum for a relativistic iron line, assuming a broken power law for the emissivity ($q_1 = 5.5$, $q_2 = 2.5$, $R_{\mathrm{break}} = 15\,R_{\mathrm{g}}$), a spin of 0.5 and an inclination of 45 degrees.

In recent years a number of black hole spin measurements, using this kind of modeling, have been published (e.g., Brenneman & Reynolds, 2006; Gallo et al., 2010; Miller et al., 2009; Miniutti et al., 2009; Schmoll et al., 2009; Brenneman et al., 2011; Fabian et al., 2013). These works have blazed the trail of supermassive black hole spin measurements, using full-up relativistically modified reflection models (rather than simple broad iron line models) to improve the robustness of the results. However, most of these works (Gallo et al. (2010) being a notable exception) base their spin results on single-epoch spectra. As will be expanded upon in Chapter 2, such studies can be affected by modeling degeneracies, that make it hard to recover the true shape of the reflection spectrum or even to detect it in the first place (Reeves et al., 2004; Guainazzi et al., 2010). These degeneracies can be reduced by the multi-epoch approach that we follow in Chapters 2 and 3.

Spectroscopic features are not the only implication of X-ray reflection. The X-ray reflection predicts a time delay (reverberation lag) between the direct X-ray continuum and the reflection component, and this delay is energy-dependent. In recent years several such lags have been detected (e.g. Fabian et al., 2009; Emmanoulopoulos, McHardy, & Papadakis, 2011; Alston, Vaughan & Uttley, 2013; De Marco et al., 2013), confirming the existence of reflection in these sources. An energy-lag spectrum is calculated by determining lags for different energies with respect to a given reference band (in this case the one, where the power law dominates) within a frequency range of interest. The frequency range of interest is rather high (a few $10^{-4}\,\mathrm{Hz}$) in the case of reflection as it is assumed to originate from very close to the black hole. A larger lag is expected in the energy bands where more reflection is observed with respect to the power law. Consequently the energy-lag spectrum looks similar to a broadened reflection spectrum (Zoghbi et al., 2013). With the quality of the data increasing, reverberation lags have even been detected within the Fe K region, giving another major boost to the existence of broad iron lines (Cackett et al., 2014; Kara et al., 2013).

1.4 Modeling the X-ray spectrum

A bulk of the work in this thesis involves extracting information from the X-ray spectrum through detailed broad band modeling. In X-ray Astronomy a variety of specific software packages exist to perform this task, most notable are ISIS (Houck & Denicola, 2000) and XSPEC (Arnaud, 1996). These programs are necessary because, for example, there are significantly fewer photons detected in the X-ray band, compared to visible and UV observations, which requires the careful use of statistics. In addition, the continuum emission plays a larger role in the X-ray band than in other wavebands, and it carries significant information. The general approach for X-ray spectral fitting is to select a parametrized model, fold the model through the instrument's response to incoming X-rays, and then to compare the folded model with the data. The fit statistic used to evaluate how well the model describes the data is usually χ^2-statistics. A detailed description how X-ray spectral fitting works can be found in Arnaud, Smith, & Siemiginowska (2011).

A large variety of models exist to describe X-ray spectra; those relevant for this thesis are briefly explained below:

Galactic Absorption:

The X-ray absorption by the ISM between us and the astronomical source is described by an improved version of the Tübingen-Boulder ISM absorption model (`TBnew`, Wilms, Allen & McCray, 2000). The model determines the absorption from the various atoms, ions, and molecules, calculating the total cross section as the sum of the individual cross sections weighted by their respective abundances. The magnitude of absorption is normalized to the hydrogen column density.

Continuum:

As described in §1.3.1, the continuum in the X-ray band can be roughly described by a simple power law $\left(N(E) \sim E^{-\Gamma}\right)$. More complex models describing the Comptonization more accurately also exist. For example, the `compTT` model treats the thermal Comptonization of soft photons for several geometries by an analytical approximation.

Warm Absorption & Photoemission:

The modeling of warm absorption and photoemission requires a code that incorporates the necessary atomic data; in this work we use the XSTAR code. XSTAR solves the thermal and ionization balance of a sphere of material irradiated by ionizing radiation in order to compute the transmitted, emitted and scattered spectrum. The user can specify the shape of irradiating continuum and many other parameters. While the XSTAR-based model `warmabs` allows the calculation of the radiative transfer on-the-fly while fitting, this slows down the fitting considerably. Therefore, we usually pre-calculate a set of synthetic spectra for a parameter range of interest and fit these pre-calculated spectra to the data. For the parameter space between the computed spectra interpolated spectra are used. Although not ideal, these tables are sufficient for our purposes and we use them to model the photoemission. For our warm absorber tables, we assume a typical typical ionizing spectrum (a power law with $\Gamma = 2$) and parametrize the tables by the column density of the gas and the ionization parameter ($\xi = \frac{L}{n\,R^2}$).

Reflection and its Relativistic Distortion:

X-ray reflection can either be cold (neutral) or ionized, each case has its own model. `Pexmon` (Nandra et al., 2007) describes the reflection from neutral material by irradiating it with an exponential cut-off power law continuum, the scattering is modeled as explained in Magdziarz & Zdziarski (1995) and the fluorescent lines were calculated in George & Fabian (1991). The ionized reflection is more difficult to determine due to the complex line spectrum that results. There are two popular models; `reflionx` (Ross & Fabian, 2005) and `xillver` (García et al., 2013), which both compute the reflection from irradiation of a slab of material with an exponentially cut-off power law. Close to the black hole this ionized reflection spectrum will be skewed by the effects associated with the presence of the black hole such as the relativistic Doppler effect, gravitational redshifting, and relativistic frame dragging. This is accounted for by applying a convolution model, such as `relconv` (Dauser et al., 2010), to the reflection spectrum.

1.5 Making progress – this thesis

The goal of this thesis is to explore the central regions in several AGN. First, by utilizing the reflection spectrum to probe the region very close to the black hole and then by using the variability of the radiation to learn about the processes taking place. In Chapter 2 we explore the X-ray spectrum of the unabsorbed Seyfert 1 galaxy Fairall 9, using high quality *Suzaku* and *XMM* data. We obtain a reliable measurement of the disk reflection parameters and our analysis suggests that the soft excess is a composite of several distinct spectral components, such as Comptonization from lukewarm material and the blurred ionized reflection, which is required to describe the prominent broad iron line in the source. The third chapter focuses on the formation of jets. We study the central engine in the broad-line radio galaxy 3C120 using a multi-epoch analysis of a deep *XMM* observation and two deep *Suzaku* pointings. In Chapter 4, we return to Fairall 9 reporting on the discovery of 4–7 day long flux dips in the source from a 10 year *RXTE* monitoring. This is followed by an investigation of the object's UV variability in Chapter 5. Taken together, these two Chapters highlight the existence of variability that is not readily accounted for in standard accretion disk models. Conclusions and a brief outlook are presented in Chapter 6.

Chapter 2: The black hole spin and soft X-ray excess of the luminous Seyfert galaxy Fairall 9

2.1 An Introduction to Fairall 9

With the amount of information to be gained from studies of the reflection spectrum, its study is rather popular as already outlined above. However, many of these previous studies have considered objects that show strong warm absorbers in their soft X-ray spectra. This has led some authors to suggest that the detection of relativistically broadened iron lines is an artifact of incorrectly modeling the absorption (Miller, Turner & Reeves, 2008). While arguments exist against these absorption dominated models (Reynolds et al., 2009), it is clearly interesting to study relativistic disk reflection in objects without any obvious absorption. Therefore, in this chapter, we study one of the brightest "bare" Seyfert galaxies to show relativistic disk reflection but no warm absorber – Fairall 9.

Fairall 9 is a well-studied Seyfert 1 galaxy ($z = 0.047$) that has never shown any imprints of a warm absorber in its X-ray spectrum (Reynolds, 1997; Gondoin et al., 2001; Schmoll et al., 2009; Emmanoulopoulos et al., 2011). The Galactic column in the direction of Fairall is also modest ($3.15 \times 10^{20}\,\mathrm{cm}^{-2}$; Kalberla et al., 2005), giving us an unobscured view of its soft X-ray continuum. Fairall 9 shows limited X-ray variability on both long and short timescales (Markowitz & Edelson, 2001) with the exception of occasional sudden dips that last one or two weeks (see Chapter 4). Studies with *ASCA* and an early *XMM-Newton* observation revealed a prominent narrow, neutral iron Kα line and a possibly broad iron line (Reynolds, 1997; Gondoin et al., 2001). An analysis of the 2007 *Suzaku* observation by Schmoll et al. (2009) confirms the presence of a moderately weak broad iron line and estimates the dimensionless spin parameter of the black hole to be $a = 0.6 \pm 0.07$ under the assumption that the emissivity profile of the X-ray reflection is an unbroken power law with an emissivity index constrained to be less than 5. More recently, Emmanoulopoulos et al. (2011) analyzed a moderately deep 2010 *XMM-Newton* pointing (130 ks), and found a weak spin constraint ($a = 0.39^{+0.48}_{-0.30}$) that spans the range from slowly spinning to rather rapid prograde spin. Worryingly, the disk inclination of $i = 64^{+7}_{-9}$ deg derived by Emmanoulopoulos et al. (2011) is strongly inconsistent with the value of $i = 44 \pm 1$ deg measured by Schmoll et al. (2009). Most recently, Patrick et al. (2011) have examined a deep 2010 *Suzaku* pointing obtained as part of the *Suzaku AGN Spin Survey* Key Project (PI Reynolds). They found the spin to be unconstrained when the spectrum is fitted by a blurred ionized disk spectrum, and determined yet a third value for the disk inclination, $i = 33^{+3}_{-5}$ deg.

In this *Chapter*, we aim to bring clarity to the question of the black hole spin and disk inclination in Fairall 9 by considering all available *XMM-Newton* & *Suzaku* pointings, including the long *XMM-Newton* pointing of 2010 and the *Suzaku* Key Project pointing of 2010. To obtain robust measurements of the accretion disk parameters and black hole spin it is crucial to understand the continuum and its variation to the highest precision possible. We highlight the importance of multi-epoch fitting techniques in breaking a modeling degeneracy resulting from the presence of narrow ionized iron lines, as well as uncovering evidence for a soft excess above and beyond that resulting from soft X-ray reflection from a uniformly ionized accretion disk. Using this methodology, we derive concordant values for black hole spin and disk inclination.

The outline of this chapter is as follows. First, we describe the datasets used in this work and briefly discuss data reduction techniques (§2.2). After a preliminary investigation of spectral fits to the individual data epochs, we perform a multi-epoch analysis in order to produce robust and concordant constraints on on the spin of the black hole and the inclination of the disk (§2.3). We end with a brief discussion of the lessons learned concerning methodologies for extracting black hole spin from X-ray spectra (§2.4).

2.2 Observations & Data Reduction

2.2.1 Data Reduction

2.2.1.1 Suzaku

A summary of the observations discussed in this chapter is presented in Table 2.1. All *Suzaku* data reduction was performed within Heasoft v6.11. The version 20110608 of the relevant *Suzaku* CALDB files were used. The *Suzaku* data were re-

Table 2.1: Overview of observations and exposures. Superscript$^{\mathrm{a}}$ denotes that XIS0/XIS1/XIS3 were used. All *Suzaku* data were obtained after the failure of XIS2.

Observatory	Instrument	Date	ObsID	Exposure [ksec]
Suzaku (B)	XIS$^{\mathrm{a}}$	2010/05/19	705063010	191
	PIN			162
Suzaku (A)	XIS$^{\mathrm{a}}$	2007/06/07	702043010	139
	PIN			127
XMM-Newton (B)	EPIC-pn	2009/12/09	0605800401	91
XMM-Newton (A)	EPIC-pn	2000/07/05	0101040201	16

duced following the standard procedure described in the "*Suzaku* ABC Guide[1]".

For the *Suzaku* X-ray Imaging Spectrometer (XIS; Koyama et al., 2007), all data were taken in the full window mode. The XIS data files were first reprocessed as recommended by the ABC Guide. For all operating XIS detectors (XIS0, XIS1, XIS3), the source extraction region was chosen to be a circle of radius of $\sim 4\,\mathrm{arcmin}$ and the background was taken from a region on the same chip. Individual spectra and response files for each detector and data mode were created using the tasks `xisrmfgen` and `xissimarfgen`. Finally, the spectra and response files of all data modes for a given detector were summed, weighted by exposure time, to yield one spectrum for each XIS. Lightcurves were also created from the reprocessed event files using `xselect`.

The Hard X-ray Detector (HXD; Takahashi et al., 2007) data were first reprocessed as recommended by the ABC Guide, and then filtered using `xselect` with the standard criteria. Only the PIN data is considered in this work as the GSO is

---

[1] http://heasarc.nasa.gov/docs/suzaku/analysis/abc/abc.html

not suitable for sources with the count rate as low as Fairall 9. For the PIN, the appropriate "tuned" background files were downloaded from the High Energy Astrophysics Science Archive Research Center (HEASARC). We then extracted source and background spectra from the "cleaned" event files using `hxdpinxbpi`.

In addition to the reduction steps outlined above, the May-2010 Fairall 9 *Suzaku* data had to be treated with special caution as it is affected by a variety of calibration/pointing problems. As one can see in Fig. 2.1, the pointing was unstable and the standard attitude solution was inaccurate during this observation, with the satellite wobbling back and forth between two positions separated by 1 arcmin. Although it is known that *Suzaku* is suffering from an attitude control problem and therefore a mild form of this is already accounted for in the calibration files delivered with the data, it appeared to be too strong to be properly removed with the standard correction (Suzaku memo 2010-05). The best results are achieved by creating a new, corrected attitude file using the tool `aeattcor.sl` [2] written by Mike Nowak; a detailed description of this tool can be found in Nowak et al. (2011).

Once corrected for, the wobble leaves three remaining imprints on the spectra. Firstly, since the wobble puts some of the source photons into a region of the image plane where the high-energy vignetting function is more poorly known, there are some deviations between the different XIS spectra above 8–9 keV. We choose to use XIS data up to 10 keV but must be cautious about interpreting spectral residuals at the highest XIS energies. Secondly, as is well known, the XIS spectra are contaminated by absorption from a hydrocarbon layer residing on the optical blocking

---

[2] http://space.mit.edu/CXC/software/suzaku/aeatt.html

filter. This contamination is monitored by the *Suzaku* team and corrected for in the construction of the effective area file. However, the contamination has spatial dependence and, for XIS0, it appears that the wobble during this observation has placed substantial numbers of source photons on parts of the image plane in which the contamination is poorly known. As a result, the XIS0 spectrum deviates from the other XIS spectra below 2 keV. This deviation is significant (reaching values as high as 50 %) and forces us to ignore XIS0 data below 2.3 keV. Lastly, due to the vignetting issue, there is no reason to suspect that the standard XIS/PIN cross normalization factor of 1.18 (nominal HXD aimpoint; Suzaku memo 2008-06) is appropriate for this dataset — the suppression of XIS flux by the additional vignetting would increase this cross normalization. We must allow this cross normalization to be a free parameter and, indeed, our best fit models suggest values of 1.3.

2.2.1.2 XMM-Newton

The two *XMM-Newton* datasets were reduced using the *XMM-Newton* Science Analysis System (SAS) version 10.0.0 and the CCF calibration file XMM-CCF-REL-270. We only consider EPIC-pn data for the analysis performed in this chapter, as MOS does not have enough signal-to-noise in the iron K region to contribute significantly to the constraints. The EPIC-pn data were reprocessed and screened using the tool `epchain`. The spectra for the EPIC cameras were then extracted using the tool `evselect`, selecting the default grade pattern. Source spectra are taken from a circular region and the background spectra from a region on the same

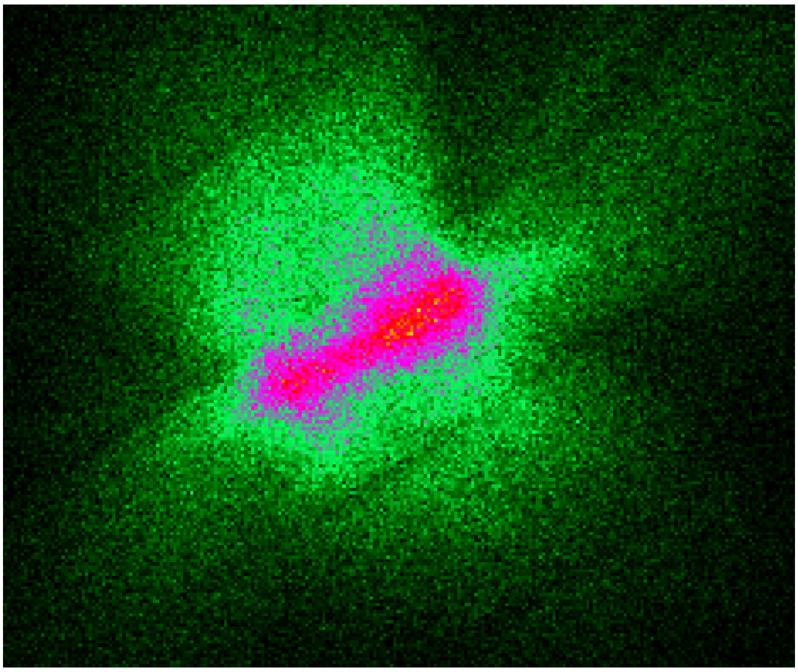

Figure 2.1: Image for XIS3 from uncorrected *Suzaku* pointing for Fairall 9.

chip. The effective area files were generated using the SAS task `arfgen`, and the redistribution matrices were produced using the task `rmfgen`.

2.3 Results

2.3.1 Initial Data Exploration and Model Construction

Unless explicitly stated otherwise, all XIS/EPIC-pn spectra are binned to a signal-to-noise ratio of 10. The considered energy ranges for fitting are 0.7-1.5 keV and 2.3-10 keV for *Suzaku*-XIS, with the energies around 2 keV being excluded because of known calibration issues around the mirror (gold) and detector (silicon) edges. The only exception to this is the XIS0 spectrum for the newest Fairall 9

Suzaku pointing; as already mentioned in §2.2.1.1 this spectrum suffers from uncorrected contamination at soft energies and, therefore, we ignore the region of this spectrum below 2.3 keV. EPIC-pn spectra are used in the 0.5-10 keV band. For all *Suzaku* pointings, PIN spectra were binned to a S/N of 5 and are used in the 16-35 keV band. As our spectral models include a convolution with a relativistic transfer function, which requires an evaluation of the underlying model outside of the energy range covered by the data, we extended all energy grids to energies far beyond the upper energy limit given by the highest data bin considered in fitting. The observations considered in this work span a duration of 10 years (Table 2.1), and hence give an idea of the long-term variability of the object. None of these observations show significant short-term (intra-observation) variability. Therefore, our spectral analysis considers only pointing averaged spectra.

As an initial exploration of these data, we fit a simple absorbed power-law to the 2.3–4.5 keV part of the spectrum; Figure 2.2 shows the ratio of the data in the 0.5–10 keV band to this simple model for all four datasets. All datasets show a prominent narrow, fluorescent iron Kα line (6.4 keV rest frame) as well as the blend of the Kβ/Fe XXVI lines (7.07 keV/6.96 keV rest frame). The spectrum shows clear concavity, revealing the presence of a soft excess and, possibly, Compton reflection. The two narrow fluorescent iron lines together with the reflection hump are clear evidence for cold reflection in the source, either from the torus or from the outer parts of the accretion disk. None of the spectra show any signs of warm absorption, as already discussed in §2.1. Despite these similarities, the spectral shape varies significantly throughout the years, with the *XMM-Newton* pointings (2000, 2009)

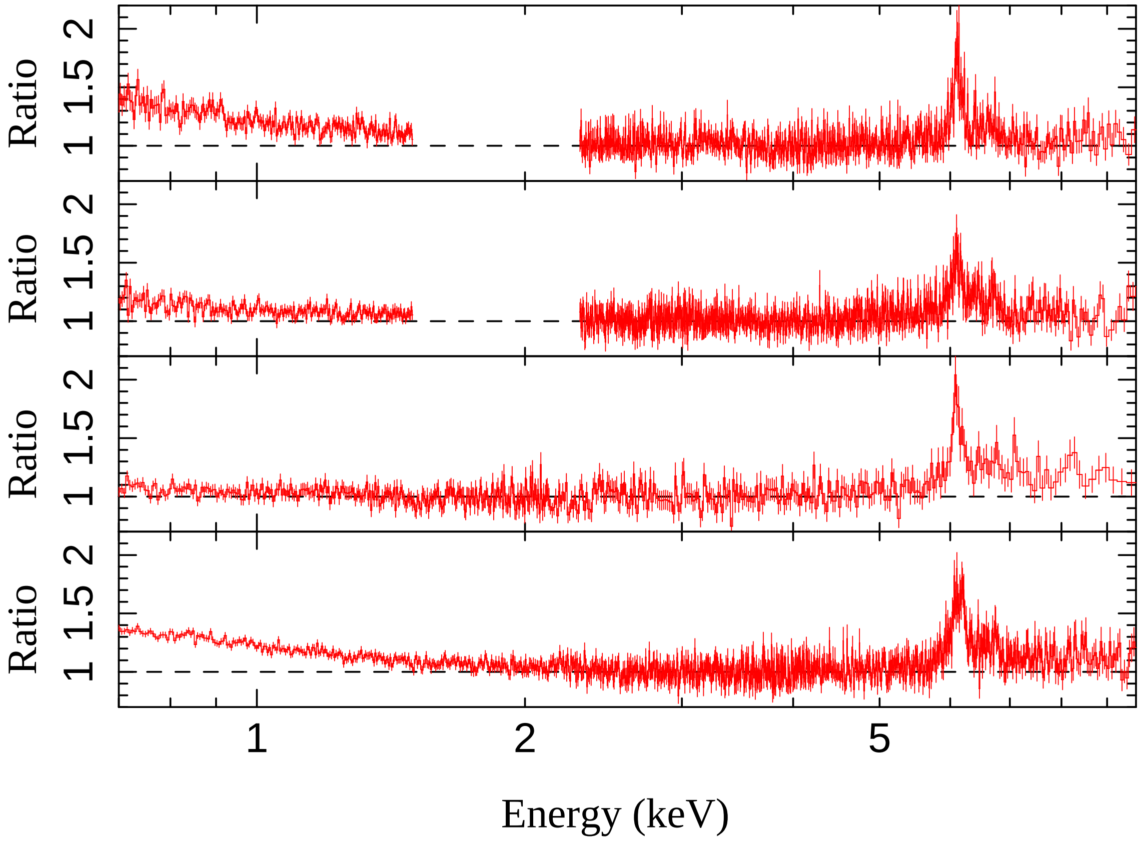

Figure 2.2: Ratio to a simple power law for Fairall 9 for Suzaku A [Top Panel], Suzaku B [Upper Middle Panel], XMM A [Lower Middle Panel], XMM B [Bottom Panel].

catching the source in a lower flux state. This variability is even more apparent when plotting the unfolded[3] spectra (Fig. 2.3). As the signal-to-noise in the short (2000) *XMM-Newton* pointing is significantly lower than in the other datasets we do not consider this pointing for the remaining part of this work.

Building upon previous works (Schmoll et al., 2009; Emmanoulopoulos et al., 2011), we construct a multi-component spectral model to describe our spectra. The

---

[3] The unfolding is performed by assuming a diagonal response matrix not making any assumptions about the description of the spectra.

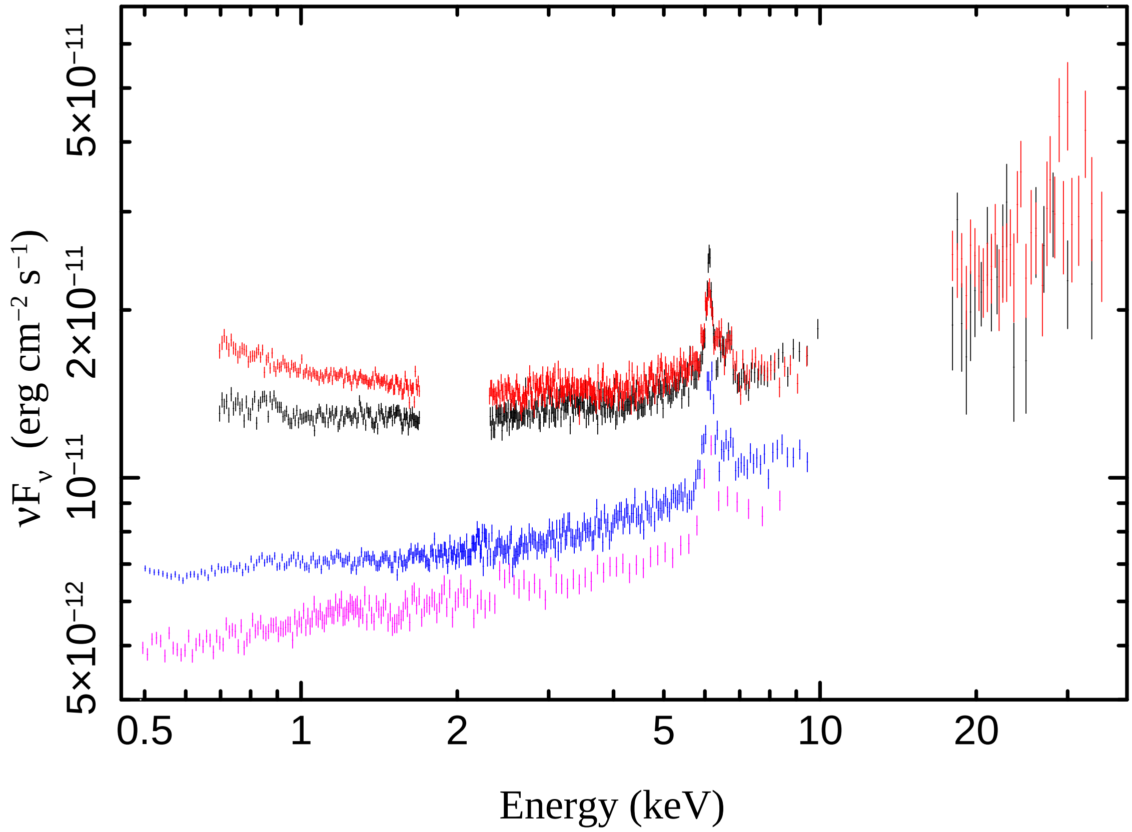

Figure 2.3: Unfolded spectra (Suzaku A [black], Suzaku B [red], XMM A [purple], XMM B [blue]) of Fairall 9 showing the spectral variability of the source. The spectra were rebinned for plotting.

underlying primary continuum is described by a powerlaw with photon index Γ. We use the model `pexmon` (Nandra et al., 2007) to describe the cold reflection of this powerlaw from distant material. In particular, `pexmon` self consistently models the strength of the narrow Fe Kα, Fe Kβ, and Ni Kα lines, the Compton shoulder of the Fe Kα line, and the Compton reflection continuum. The strength of the distant reflection is characterized by the usual reflection fraction R normalized such that $R = 1$ corresponds to a reflector that subtends half of the sky as seen from the X-ray source. As some parameters for `pexmon` cannot be determined from our fits we fix them to certain values; we fix the inclination to 60 degrees (most probable value for an isotropic distribution) and abundances to solar values. The high-energy cutoff of the continuum powerlaw is fixed to 300 keV.

To describe the ionized reflection associated with the inner accretion disk, we used a modified version of `reflionx` developed by Ross & Fabian (2005). Starting from the publicly available version, we redefined the normalization parameter (norm → norm/ξ) such as to statistically decouple the true flux normalization from the ionization parameter ξ. This definition results in a more rapid and robust convergence of the spectral fit. For the ionized reflection model, the iron abundance and ionization parameter are allowed to vary freely. The photon index of the irradiating continuum, however, is tied to the index for the continuum underlying the cold reflection. The ionized reflection component is then relativistically blurred using the model `relconv` (Dauser et al., 2010); this naturally gives rise to a relativistic iron line, blurred Compton reflection hump and a soft excess. The radial dependence of the emissivity of the reflection component is assumed to have a broken power-law form, breaking from r^{-q_1} to r^{-q_2} at a radius $R_{\rm break}$. The inner edge of the X-ray reflection regime is taken to be at the ISCO (Reynolds & Fabian, 2008), and the outer edge was fixed to $400\,R_{\rm g}$. Provided that $q_2 > 2$, the relativistic blurring kernel is only weakly dependent upon this outer radius. The accretion disk inclination i, and the black hole spin a were left as free parameters. In addition, photoelectric Galactic absorption is modeled with `TBnew`[4] a newer version of `TBabs` (Wilms, Allen & McCray, 2000) with cross sections set to `vern` and abundances set to `wilm`.

---

[4] http://pulsar.sternwarte.uni-erlangen.de/wilms/research/tbabs/

A careful examination of the residuals shown in Fig. 2.2, especially for observation Suzaku-B, reveals a line like feature between cold-FeKα and cold-FeKβ lines. While some or all of this emission may be associated with the blue peak of the broad iron line, another possibility is that we are seeing FeKα line emission from Fe XXV (which produces a complex at 6.7 keV). It therefore seems possible that the spectral model discussed above is missing an emission line system producing Fe XXV and possibly Fe XXVI line emission. Hence we include an additional photoionized emission component (Fig. 2.4); physically, this may be an accretion disk wind (warm absorber) which is out of our line of sight. The photoemission is parametrized by ionization parameter and norm. It is modeled using a table model calculated using `xstar2xspec` from the `XSTAR` model `photemis`[5], assuming irradiation by a power law $L_\varepsilon \propto \varepsilon^\alpha$ with α=-1 and a number density of $10^{10}\,\mathrm{cm}^{-3}$. At the ionization stages relevant for this work ($\log \xi > 3.6$) there is no dependence of the spectral shape on column density for the model, its value was therefore kept fixed at $10^{22}\,\mathrm{cm}^{-2}$. We note that the inclusion of this emission line component this does not preclude the possibility that the residuals at 6.7 keV are from the blue peak of the iron line, but it does allow the model to explore any degeneracy created by the superposition of the broad iron line and the narrow ionized line emission.

When applying this spectral model to the data, a cross calibration constant was introduced for *Suzaku* between XIS and PIN (and in case of the 2010 *Suzaku* pointing, also between the XISs). The constant was fixed to the values given in the *Suzaku* ABC Guide, 1.16 for XIS aimpoint and 1.18 for HXD aimpoint. An

---

[5] http://heasarc.nasa.gov/docs/software/xstar/xstar.html

exception to this is observation Suzaku-B; as mentioned above, due to the pointing issues, there is no expectation that the fiducial XIS/PIN cross normalization should be appropriate and hence it was left as a free parameter.

We begin with this model as our base model and, in §2.3.2, we fit this model to each dataset individually. After noting problematic issues associated with these fits, we perform simultaneous fits to data from different observations of Fairall 9, under the assumption that the most fundamental parameters of the system (spin, accretion disk inclination and iron abundance) do not change — this so-called multi-epoch fitting is presented in §2.3.3 and, as we shall see, yields insights into the spectral properties of this AGN.

Throughout this work, the spectral analysis were performed with the Interactive Spectral Interpretation System[6] (ISIS Version 1.6.0-7; Houck & Denicola, 2000) and the newest *XSPEC* 12.0 models are used (Arnaud, 1996). All uncertainties are quoted at the 90 % confidence level for one interesting parameter ($\Delta\chi^2 = 2.7$).

2.3.2 Independent fits to individual datasets

We begin by conducting independent fits of our base spectral model to the three remaining observations under consideration, XMM-Newton-B, Suzaku A and Suzaku B. Our base model provides a good description of the three datasets, with reduced-χ^2 values between 1.00–1.04 (Table 2.3.2). A sample spectrum with residuals is shown in Fig. 2.5 illustrating the good quality of the fit.

We argue below that these fits are incomplete and hence that the inferred

---

[6] http://space.mit.edu/cxc/isis

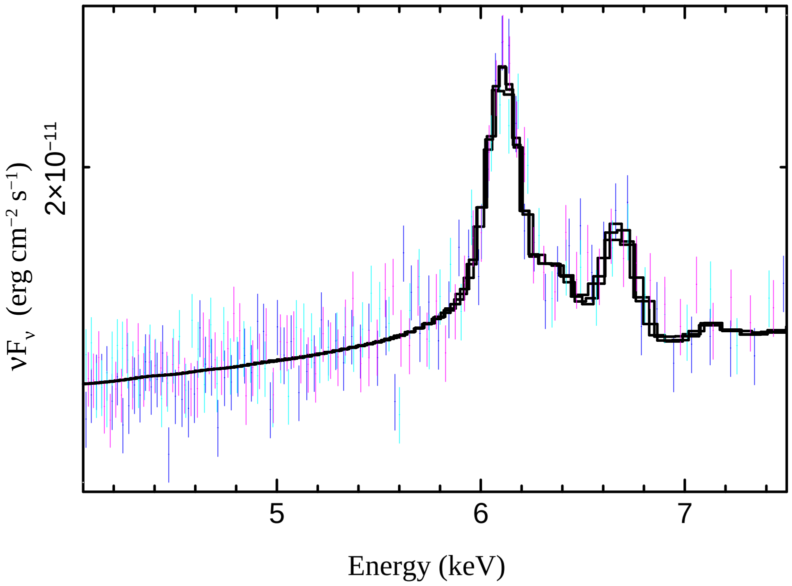

Figure 2.4: Unfolded spectra (rebinned for plotting), assuming a diagonal response, and model [black] of the iron line region for observation Suzaku-A fitted with the model including photoionized emission (see §2.3.1). The plot shows the energies in the observed frame.

parameters are thus not necessarily correct. However, it is instructive to compare our results from these fits (Table 2.2) with previously published works. For Suzaku A, our derived parameters are similar to those found by Schmoll et al. (2009) with the exception of black hole spin, disk inclination, and emissivity index. Schmoll et al. (2009) apply the constraint that the inner emissivity index q_1 should not exceed 5; if we impose the same constraint, we recover a very similar intermediate spin and inclination constraint. However, our base model allows the emissivity index to be much steeper (formally pegging at $q_1 = 10$) and we find, as a result, that the inferred black hole spin tends to high values. For Suzaku B, our fits are in agreement with Patrick et al. (2011) who find that the spin is unconstrained by this dataset. For XMM-Newton B, we find a spin parameter and inclination that

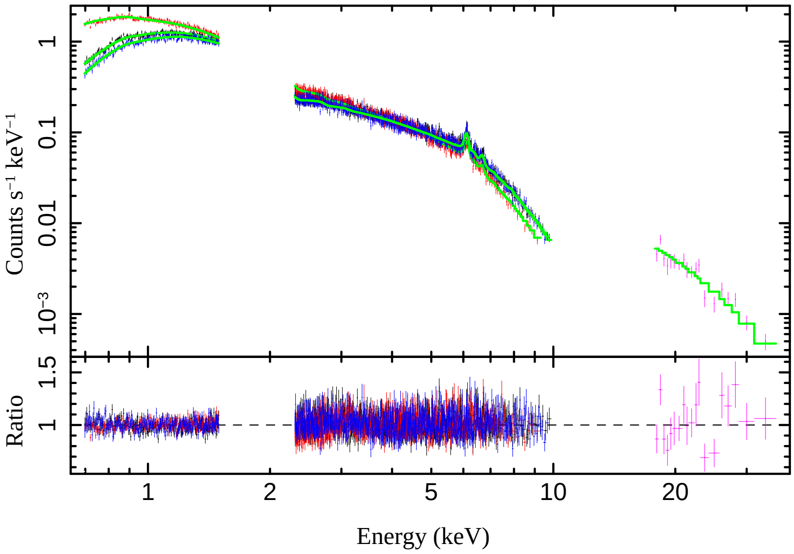

Figure 2.5: Spectra, model [green] and residuals for pointing Suzaku-A (XIS0 [black], XIS1 [red], XIS3 [blue], PIN [purple]) for the fit with the base model.

is strongly discrepant with those derived in Emmanoulopoulos et al. (2011). We attribute this difference to the inclusion of a photoemission component, a newer absorption model (`TBnew` vs. `wabs`) and a different model construction.

However, just looking at the results of our own uniform analysis, we find important and informative inconsistencies. Comparing the fit parameters derived from the different observations we find that the black hole spin, the disk inclination, and the iron abundance appear to have significantly different values between the three datasets (Table 2.2). Naturally we would expect these physical quantities to be constant on the time spanned by these observations.

Table 2.2: Spectral Parameters for Fairall 9 base model fits with additional photoionized emission; See the text for a description of the model. *Suzaku* Spectra are normalized to XIS0 data. The power law normalization is photons $\mathrm{keV}^{-1}\,\mathrm{cm}^{-2}\,\mathrm{s}^{-1}$ at 1 keV.

		Suzaku A	Suzaku B	XMM B
continuum & cold reflection	A_{pex} $[10^{-3}]$	$8.60^{+0.08}_{-0.08}$	$10.49^{+0.01}_{-0.08}$	$4.80^{+0.02}_{-0.02}$
	Γ	$2.11^{+0.01}_{-0.02}$	$2.11^{+0.01}_{-0.01}$	$2.11^{+0.03}_{-0.02}$
	R	$1.08^{+0.11}_{-0.11}$	$0.76^{+0.09}_{-0.09}$	$1.53^{+0.14}_{-0.13}$
ionized reflection	A_{reflionx} $[10^{-4}]$	$2.59^{+0.39}_{-0.20}$	$1.74^{+0.22}_{-0.22}$	$2.00^{+0.29}_{-0.31}$
	$Fe/Solar$	$1.30^{+0.16}_{-0.44}$	$1.35^{+0.61}_{-0.49}$	$0.50^{+0.08}_{-0.17}$
	ξ $[\mathrm{erg\,cm\,s^{-1}}]$	$12.1^{+7.2}_{-1.2}$	$1^{+0.01}_{-0}$	$1^{+1.34}_{-0}$
relativistic blurring	q_1	$10^{+0}_{-0.6}$	$10^{+0}_{-8.1}$	$9.1^{+0.9}_{-1.9}$
	q_2	$1.7^{+0.5}_{-0.3}$	$1.4^{+0.4}_{-0.9}$	$2.4^{+0.6}_{-0.8}$
	R_{break} $[R_{\mathrm{g}}]$	$4.6^{+2.1}_{-0.5}$	$8.3^{+83.5}_{-4.5}$	$6.5^{+0.2}_{-1.4}$
	a	$0.96^{+0.01}_{-0.02}$	$0.28^{+0.72}_{-1.28}$	$0.93^{+0.02}_{-0.01}$
	i [deg]	$35.0^{+3.4}_{-5.6}$	$62.5^{+5.5}_{-2.4}$	$5^{+9.9}_{-0}$
plasma	A_{phot} $[10^{-3}]$	$0.98^{+16.1}_{-0.73}$	$11.47^{+52.04}_{-4.04}$	$65.2^{+30990.48}_{-15.2}$
	$\log\xi$	$4.3^{+0.5}_{-0.4}$	$3.7^{+0.6}_{-0.0}$	$4.4^{+0.2}_{-0.1}$
cross calibration	$c_{\mathrm{XIS0-1}}$	1.00	$0.97^{+0.01}_{-0.01}$	. . .
	$c_{\mathrm{XIS0-3}}$	1.00	$0.92^{+0.01}_{-0.01}$	. . .
	$c_{\mathrm{XIS0-PIN}}$	1.16	$1.43^{+0.07}_{-0.07}$	. . .
	χ^2/dof	2593.1/[2500-13]	2538.1/[2559-16]	1129.8/[1110-13]
	p-value	0.07	0.52	0.25
	χ^2_{red}	1.04	1.00	1.02

As we show below, a multi-epoch analysis reveals the need for a new continuum component to describe the soft excess. Foreshadowing that discussion, we note that adding such a soft excess component to the model for each individual dataset results in unconstrained spin parameters and emissivity indices, i.e., the individual datasets do not possess the S/N to determine spin and inclination in the more complex models; there is a significant trade off between the parameters of the soft component and the spin and inclination for each individual data set. This also implies that that the extreme values of spin and q_1 found in a fit of the base model to Suzaku-A may arise due to a model which is (possibly falsely) attempting to fit a very smooth soft excess with an ionized reflection spectrum, necessitating extreme broadening.

2.3.3 Multi-epoch analysis

The inconsistencies resulting from independently fitting our base model to the individual pointings leads us to the use of multi-epoch fitting. In multi-epoch fitting, we assume that the source spectrum is always composed of the same principal physical components and that, when physical considerations demand, parameters are forced to have the same value for all epochs. In our case, we demand that the black hole spin parameter, the inclination of the disk, the iron abundance, and the strength of the photoionized emission component (believed to originate from an extended AGN wind) must have common values across the fits to all of the datasets. In all cases, these parameters are believed to remain fixed for any given AGN over human timescales. Aside from these additional constraints on the parameters, the model set-up is the same as for the fitting of the individual pointings. We allow the slope/normalization of the primary powerlaw, as well as the normalization, emissivity profile and ionization state of the disk reflection to float freely between datasets — these parameters depend upon the structure/geometry of the disk corona that can plausibly change on timescales that are (much) shorter than the inter-pointing spacing. Fitting in this manner we find that the broken power law emissivity profile is ill-constrained and a simple power law emissivity profile is sufficient to describe the data very well. Furthermore, to reduce the number of spectral bins in each dataset, we co-added the front-illuminated XIS data (XIS0 and XIS3); this eases the significant computational expenses of multi-epoch fitting.

Statistically, fitting this model to the full multi-epoch dataset produces a good fit, with reduced χ^2 of 1.06. The best fit parameters and errors are listed in Table 2.3. The best fitting spin is a little higher ($a = 0.71^{+0.08}_{-0.09}$) and the inclination a little lower ($i = 37^{+4}_{-2}$ deg) than found in the previous study of Schmoll et al. (2009) but, given the error bars, there is no strong discrepancy. The ionization parameter either takes rather low values (XMM, Suzaku A) or very high values (Suzaku B). This is directly tied to the fact that, apart from the iron line itself, there are no other strong features in the soft X-ray band that the reflection models are locking onto in the spectrum. One aspect of this fit that gives us pause is the high PIN/XIS cross normalization component, $C_{\rm XISf-PIN} \approx 1.74$. While we have already acknowledged that the pointing errors would render invalid the standard value of $C_{\rm XISf-PIN} = 1.18$, this measured value would imply a $\sim 30\%$ suppression of the net XIS count rate below the fiducial value, a significantly larger depression than is reasonably expected from the pointing problems. A more likely possibility is that the spectrum has curvature in the concave sense so that the true PIN-band flux is higher than predicted by our base spectral model.

Table 2.3: Spectral Parameters for Fairall 9 multi-epoch base model fit with additional photoionized emission; See the text for a description of the model. *Suzaku* Spectra are normalized to XIS0 data. The power law normalization is photons $\mathrm{keV^{-1}\,cm^{-2}\,s^{-1}}$ at 1 keV.

		Suzaku A	Suzaku B	XMM B
continuum & cold reflection	A_{pex} $[10^{-3}]$	$8.66^{+0.13}_{-0.07}$	$7.52^{+0.57}_{-1.10}$	$4.02^{+0.07}_{-0.07}$
	Γ	$2.07^{+0.02}_{-0.01}$	$2.05^{+0.01}_{-0.01}$	$1.93^{+0.01}_{-0.01}$
	R	$0.96^{+0.08}_{-0.08}$	$0.95^{+0.14}_{-0.09}$	$1.47^{+0.12}_{-0.12}$
ionized reflection	A_{reflionx} $[10^{-4}]$	$1.51^{+0.28}_{-0.15}$	$0.53^{+0.09}_{-0.09}$	$0.34^{+0.03}_{-0.03}$
	$Fe/Solar$		$\mathbf{0.67}^{+0.08}_{-0.08}$	
	ξ $[\mathrm{erg\,cm\,s^{-1}}]$	$6.1^{+3.2}_{-3.8}$	$1739.2^{+1142.6}_{-509.2}$	$500.0^{+18.5}_{-107.9}$
relativistic blurring	q	$2^{+0.23}_{-0}$	$2.57^{+0.47}_{-0.40}$	$8.61^{+1.39}_{-1.88}$
	a		$\mathbf{0.71}^{+0.08}_{-0.09}$	
	i [deg]		$\mathbf{37}^{+4}_{-2}$	
plasma	A_{phot}		$\mathbf{24.85}^{+46.51}_{-24.77}$	
	$\log\xi$		$\mathbf{6.7}^{+0.3}_{-2.4}$	
cross calibration	c_{XISf}	1.00	1.00	. . .
	c_{XIS1}	1.00	$0.99^{+0.01}_{-0.01}$	. . .
	$c_{\mathrm{XISf-PIN}}$	1.16	$1.74^{+0.08}_{-0.08}$	. . .
individual contributions	χ^2/dof	2228.29/[2106-11]	2071.272/[2060-13]	1447.278/[1100-11]
	p-value	0.02	0.35	0.00
	χ^2/dof		5544.218/[5276-25]	
	p-value		0.002	
	χ^2_{red}		1.06	

Partly motivated by these considerations, but also guided by the known phenomenology of AGN, we explore the hypothesis that we are missing another component that can contribute to the soft excess (above and beyond any soft excess emission from the blurred uniformly ionized reflection, that models the broad iron line). A common phenomenological model for the soft excess is a simple blackbody component. Adding a blackbody component to the spectral model does not yield improved fits — none of the datasets show the strong curvature representative of the Wien tail of a blackbody. However, significant improvements in the goodness of fit are achieved using a soft excess model consisting of a "warm" thermal Comptonization component. In detail, we add a thermal Comptonization component described by the `comptt` model (Titarchuk, 1994) with a seed photon temperature of 40 eV (representative of the expected thermal emission from the AGN disk), an optical depth τ and an electron temperature kT.

When applied to the multi-epoch data, the inclusion of this soft excess component leads to an improvement in the goodness of fit by $\Delta\chi^2 = 198$ for nine additional parameters. The best fit parameters and corresponding errors can be found in Table 2.3. As compared with the base model above, the best-fit spin has slightly decreased to $a = 0.52^{+0.19}_{-0.15}$ and the best-fit inclination has increased to $i = 48^{+6}_{-2}$ deg. While the change in spin between the two models is within the error bars, the inclination change is significant and brings the results into line with the conclusions of Schmoll et al. (2009). We find that the ionization state of the inner accretion disk is significantly higher at lower flux states. The biggest surprise is that, once we include the explicit soft excess component, the iron abundance of the accretion disk is pushed towards the maximum value tabulated in the model, $Z = 10Z_\odot$. The formal 90% lower limit on iron abundance is $Z > 8.2Z_\odot$. From a modeling perspective, such a high iron abundance means simply that the iron line is strong in comparison to the Compton hump.

Table 2.4: Spectral Parameters for Fairall 9 multi-epoch fit with additional photoionized emission and soft excess component; See the text for a description of the model. *Suzaku* Spectra are normalized to XIS0 data. The power law normalization is photons $\mathrm{keV^{-1}\,cm^{-2}\,s^{-1}}$ at 1 keV.

		Suzaku A	Suzaku B	XMM B
continuum & cold reflection	$A_{\rm pex}$ $[10^{-3}]$	$6.71^{+0.53}_{-0.78}$	$3.59^{+1.55}_{-1.62}$	$3.60^{+0.17}_{-0.18}$
	Γ	$1.90^{+0.04}_{-0.05}$	$1.71^{+0.15}_{-0.09}$	$1.85^{+0.02}_{-0.02}$
	R	$0.84^{+0.07}_{-0.07}$	$0.79^{+0.13}_{-0.17}$	$1.08^{+0.11}_{-0.11}$
ionized reflection	$A_{\rm reflionx}$ $[10^{-4}]$	$0.57^{+0.12}_{-0.12}$	$0.99^{+0.34}_{-0.18}$	$0.13^{+0.02}_{-0.02}$
	$Fe/Solar$		$\mathbf{10}^{+0}_{-1.77}$	
	ξ $[\mathrm{erg\,cm\,s^{-1}}]$	$20.9^{+14.8}_{-8.8}$	$10.1^{+60.4}_{-9.1}$	$3513.5^{+381.0}_{-393.7}$
relativistic blurring	q	$2^{+0.23}_{-0}$	$9.5^{+0.5}_{-3.4}$	$2^{+0.33}_{-0}$
	a		$\mathbf{0.52}^{+0.19}_{-0.15}$	
	i [deg]		$\mathbf{48}^{+6}_{-2}$	
Comptonization	$A_{\rm compTT}$ $[10^{-3}]$	$4.01^{+0.90}_{-1.88}$	$5.17^{+0.01}_{-0.95}$	$3.65^{+18626.63}_{-1.65}$
	kT [keV]	$20.52^{+49.09}_{-9.53}$	$26.08^{+1.40}_{-1.77}$	$35.28^{+11.29}_{-33.28}$
	τ	$0.52^{+0.37}_{-0.22}$	$0.63^{+1.07}_{-0.36}$	$0.01^{+0.15}_{-0}$
plasma	$A_{\rm phot}$		$\mathbf{8.58}^{+41.89}_{-8.56}$	
	$\log\xi$		$\mathbf{6.33}^{+0.67}_{-1.68}$	
cross calibration	$c_{\rm XISf}$	1.00	1.00	. . .
	$c_{\rm XIS1}$	1.00	$0.99^{+0.01}_{-0.01}$	. . .
	$c_{\rm XISf-PIN}$	1.16	$1.26^{+0.07}_{-0.06}$	. . .
individual contributions	χ^2/dof	2232.56/[2106-11]	1985.06/[2060-13]	1128.64/[1100-11]
	p-value	0.02	0.83	0.20

continued on next page

continued from previous page

		Suzaku A	Suzaku B	XMM B
joint goodness of fit	χ^2/dof	5346.275/[5276-34]		
	p-value	0.16		
	χ^2_{red}	1.02		

However, another possibility is that the reflection from the inner accretion disk is characterized by multiple ionization components (Nardini et al., 2011) and a highly blurred, high-ionization reflection component can account for the soft excess in a similar fashion than the additional Comptonization component. To explore this model, we refit the multi-epoch data with two disk reflection components, each of which has its own ionization parameter and emissivity index. The only other difference to the multi-epoch fit above is that the iron abundance is assumed to be the same for all reflection components included in the model. Such a model leads to a fit solution of almost comparable quality than that employing the Comptonization-based soft excess component (Table 2.4). In order to describe the smooth soft excess, one of the disk reflection components adopts a high ionization state ($\xi_a \sim 1000$) and a very steep emissivity profile ($q_{\rm a} > 8$) and the black hole spin parameter becomes large ($a > 0.96$). At the same time, much less broadening/blurring is needed in order to describe the broad iron line, and so the other disk reflection component adopts a low ionization ($\xi_b \sim 1 - 10$) and a shallow emissivity profile ($q \lesssim 2.2$). This solution avoids the extreme iron abundance, with an inferred iron abundance of 0.68–0.85 $Z_\odot$.

Table 2.5: Spectral Parameters for Fairall 9 multi-epoch fit with additional photoionized emission and two ionized reflection components; See the text for a description of the model. *Suzaku* Spectra are normalized to XIS0 data. The power law normalization is photons $\mathrm{keV}^{-1}\,\mathrm{cm}^{-2}\,\mathrm{s}^{-1}$ at 1 keV.

		Suzaku A	Suzaku B	XMM B
continuum & cold reflection	A_{pex} $[10^{-3}]$	$8.02^{+0.31}_{-0.38}$	$9.84^{+0.37}_{-1.66}$	$4.81^{+0.02}_{-1.23}$
	Γ	$2.07^{+0.01}_{-0.01}$	$2.17^{+0.01}_{-0.01}$	$2.09^{+0.04}_{-0.04}$
	R	$1.33^{+0.21}_{-0.19}$	$0.95^{+0.23}_{-0.16}$	$1.89^{+0.11}_{-0.16}$
ionized reflection 1	A_{reflionx} $[10^{-4}]$	$0.51^{+0.00}_{-0.12}$	$0.41^{+0.36}_{-0.28}$	$0^{+0.02}_{-0}$
	$Fe/Solar$		$\mathbf{0.75}^{+0.10}_{-0.07}$	
	ξ $[\mathrm{erg\,cm\,s^{-1}}]$	$627.7^{+924.7}_{-411.3}$	$1091.9^{+5908.1}_{-685.2}$	100^{+6900}_{-0}
relativistic blurring 1	q	$10.0^{+0.0}_{-1.0}$	$10.0^{+0.0}_{-2.3}$	$10.0^{+0.0}_{-8.0}$
	a		$\mathbf{0.97}^{+0.02}_{-0.01}$	
	i [deg]		$\mathbf{36}^{+3}_{-3}$	
ionized reflection 2	A_{reflionx} $[10^{-4}]$	$1.00^{+0.32}_{-0.35}$	$2.35^{+0.59}_{-0.43}$	$1.52^{+0.39}_{-1.02}$
	ξ $[\mathrm{erg\,cm\,s^{-1}}]$	$12.1^{+8.6}_{-5.9}$	$1^{+1.2}_{-0}$	$1^{+30.6}_{-0}$
relativistic blurring 2	q	$2^{+0.2}_{-0}$	$2.1^{+0.3}_{-0.1}$	$5.6^{+4.4}_{-1.1}$
plasma	A_{phot}		$\mathbf{0.09}^{+0.36}_{-0.03}$	
	$\log\xi$		$\mathbf{4.3}^{+0.7}_{-0.0}$	
cross calibration	c_{XISf}	1.00	1.00	. . .
	c_{XIS1}	1.00	$0.99^{+0.01}_{-0.01}$	. . .
	$c_{\mathrm{XISf-PIN}}$	1.16	$1.43^{+0.07}_{-0.08}$	. . .
individual contributions	χ^2/dof	2208.44/[2106-11]	2012.66/[2060-13]	1168.47/[1100-11]
	p-value	0.04	0.67	0.05

continued on next page

continued from previous page

		Suzaku A	Suzaku B	XMM B
joint goodness of fit	χ^2/dof	5389.6/[5276-34]		
	p-value	0.08		
	χ^2_{red}	1.02		

2.4 Summary and discussion

The X-ray spectrum of Fairall 9 is one of the cleanest known in terms of having no discernible intrinsic absorption. Fairall 9 has also been the subject of multiple pointings by *XMM-Newton* and *Suzaku*. This makes it an interesting target for a detailed study of the relativistic reflection features including an assessment of the robustness of the derived parameters with respect to assumptions and choices made in the spectral modeling.

A simple application of our base spectral model to the individual *XMM-Newton* and *Suzaku* pointings produces unphysical results, with inconsistent values for black hole spin, disk inclination and iron abundance being derived for each pointing. We identify several factors that are at play. We clearly see (and hence include in our base model) high ionization, narrow iron emission lines, presumably from optically-thin photoionized plasma in the circumnuclear environment. When viewed with CCD-resolution ($E/\Delta E \sim 50-100$), these narrow lines can blend with the blue wing of the broad iron line from the accretion disk, inducing strong degeneracies between the strength of the photoionized emission component and the accretion disk parameters. This degeneracy is particularly strong for objects with intermediate inclination (35–60 deg) since, in these cases, the blue wing/edge of the iron line overlays the FeXXV Kα line complex.

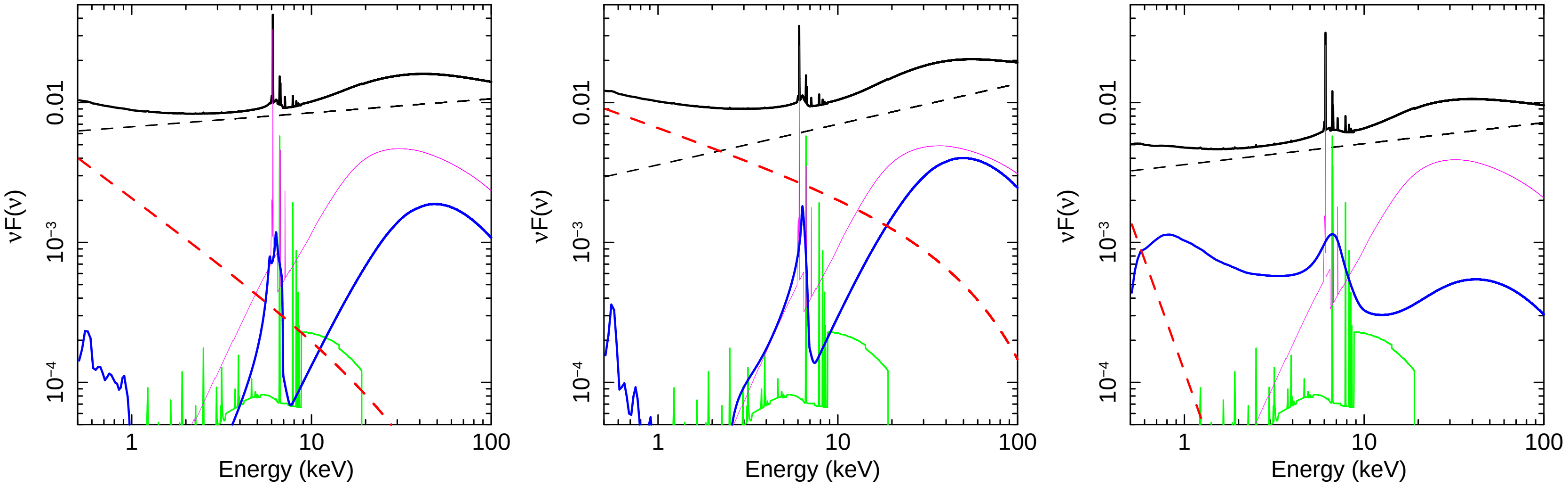

Figure 2.6: Best fitting multi-epoch model (including the additional soft continuum source) for the Suzaku A (left), Suzaku B (middle) and XMM-Newton B (right) observations. Shown here is the total model (solid-thick black line), the primary power-law continuum (dashed black line), warm Comptonization component (dashed red line), the relativistically blurred ionized disk reflection (thick solid blue line), the distant reflector (thin solid magenta line), and the photoionized emission component (green line).

When we generalize our models to include composite soft excesses, we find that individual datasets yield strongly degenerate solutions. To cut through some of this degeneracy, we make the assumption that the photoionized emission component is constant over the three years that span observations Suzaku-A, XMM-Newton-B, and Suzaku-B. We then employ a multi-epoch analysis, fitting our spectral model to these three datasets simultaneously — the black hole spin, accretion disk inclination, iron abundance, and photoionized emission component are assumed constant across all three pointings, but all other spectral parameters and normalizations are allowed to float freely between pointings. Since there is, indeed, significant flux variability between the three pointings, this approach is remarkably successful at breaking the degeneracy with the photoionized emission component and allowing us to constrain model values for the black hole spin and disk inclination. Of course, it must be highlighted that the constancy of the photoionized emission component is an *assumption* which could be violated if the emitting wind is compact (sub-parsec). This assumption must be tested by future high-resolution observations using the *Chandra* High Energy Transmission Gratings (HETG) or the *Astro-H* Soft X-ray Spectrometer (SXS).

In addition, we find that the multi-epoch spectral fit is significantly improved by the addition of another spectral component. Our analysis therefore highlights the practical importance of modeling the soft excess. The nature of the soft excess is still a matter of debate, and the soft Comptonization component that we attempt first is just one of the possible models discussed in the context of AGN spectra. In the case of Fairall 9, we have already excluded a soft excess that arises solely from inner disk reflection with a single ionization parameter, and have shown that an additional blackbody component is also rejected.

We first consider the scenario in which the soft excess is identified with an additional Comptonization component. As explicitly shown in Fig. 2.6, this additional Comptonization component is the main contributor to the soft excess during our two Suzaku observations while ionized disk reflection dominates during the XMM-Newton B pointing. The inclusion of this soft continuum has a small effect on the best fitting black hole spin and disk inclination (with our final values being $a = 0.52^{+0.19}_{-0.15}$ and $i = 48^{+6}_{-2}$ deg), but has a dramatic effect on the inferred iron abundance of the accretion disk ($Z > 8.2Z_{\odot}$). With an expected abundance value of only 2-3$Z_{\odot}$ (Groves, Heckman & Kauffmann, 2006), such a high iron abundance implies an unusual star formation history in the galactic core, or some process that preferentially differentiates iron into the photosphere of the inner disk (e.g., see discussion of Reynolds et al. 2012).

It is interesting that, in our fiducial multi-epoch fit (Table 2.3), the Suzaku-B dataset requires a high emissivity index, $q > 6$. Such high emissivity indices are normally attributed to the action of extreme light bending focusing X-rays onto the innermost regions of the disk or, alternatively, the dissipation of work done by strong torques at the ISCO. Both of these explanations would require a black hole that is spinning rapidly ($a > 0.9$), as opposed to the intermediate spin ($a \approx 0.5$) that we infer (Fabian et al., 2012). A possible resolution of this contradiction comes from the vertical geometry of the accretion disk. Fairall 9 is a luminous source accreting with an Eddington ratio of $\mathcal{L} \approx 0.15$ (Chapter 4). Standard disk theory (Shakura

& Sunyaev, 1973) tells us that the inner regions of the accretion disk will be very radiation pressure dominated and, away from the inner boundary, will have a disk thickness $h = (3\mathcal{L}/2\eta)R_g \approx 2.3R_g$ where we have taken the radiative efficiency of the disk to be $\eta = 0.1$. As the disk approaches the ISCO (at $r_{\rm isco} \approx 4.5\,R_g$ for $a = 0.5$) the thickness diminishes and, within the ISCO, the accretion flow forms a thin sheet that spirals into the black hole. This gives the photosphere of the inner disk the geometry of shallow bowl. If the X-ray source is located very close to the black hole (e.g. in a spin-powered magnetosphere) or on the inward facing surface of this bowl, the region close to the ISCO can be strongly irradiated while the disk surface at large distance may receive very little irradiation — this would manifest itself in our spectral analysis as a steep emissivity profile. Alternatively, the high emissivity index may be a mirage induced by a steep iron abundance gradient. Specifically, if the high iron abundance is due to radiative-levitation in the disk photosphere (Reynolds et al., 2012), it will have a strong radial gradient which would appear in our fits as a steep emissivity index.

Alternatively, this steep emissivity profile could be the artifact of incorrect modeling of contamination in the spectrum. As outlined in § 2.2.1.1, this *Suzaku* pointing is certainly affected by strong contamination in XIS0 below 1 keV. We assumed for this analysis that the other two detectors were correct below 1 keV, but the steep profile could be an indication that this assumption is not justified.

The alternative scenario that we consider for the soft excess in Fairall 9 is a model including two ionized reflection components with different ionization states. This double-ionized reflection solution does present difficulties, however, when we attempt to interpret it with physical models. There are two classes of models in which multiple ionization states may be present in the disk reflection spectrum. Firstly, at any given radius, the density of the disk photosphere may be patchy leading to mixed regions of high and low ionization. In such a scenario, we would expect the two ionization components to share approximately the same emissivity index since they respond to the same irradiation profile. This disagrees with the fact that we see very different emissivity indices between these two components and allows us to reject this patchy disk model. Secondly, we may expect the ionization parameter of the disk surface to have a strong radial gradient due to the radial dependence of both the irradiating flux and the disk density. The fact that we see a high-ionization component which is highly blurred (coming from the smallest radii) and a low-ionization component which is more weakly blurred (coming from substantially larger radii) fits in with this picture. However, preliminary theoretical calculations of the reflection from a disk with a radial ionization gradient reveals that the intermediate ionization states should also imprint strong soft X-ray features which we do not see (García et al., 2012).

Fundamentally, however, it is difficult to distinguish these two scenarios (new Comptonization continuum or second disk reflection component) with existing data. Although the models do not differ significantly in quality of their description of the data, the physical interpretations are quite distinct. Plotting the models to energies well above the PIN energy range (Fig. 2.7) points out how future hard X-ray studies with *Nustar* or *Astro-H* could break this degeneracy. The hard X-ray flux predicted by the double reflection scenario is substantially smaller than the one predicted by

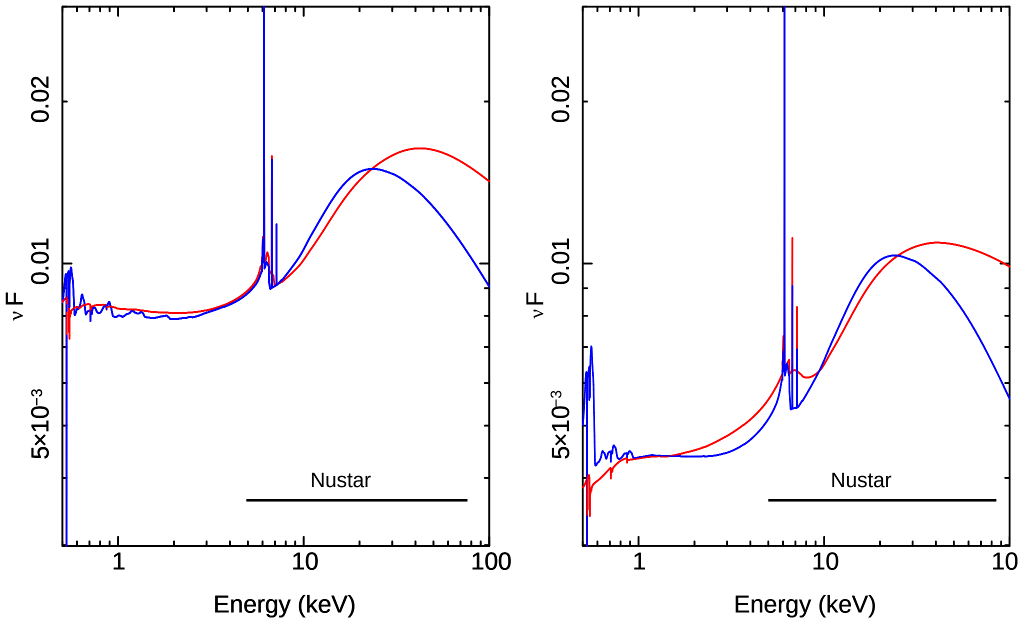

Figure 2.7: A comparison of the two best fitting spectral models, the double reflection model (blue) and the one with additional Comptonization soft excess (red), for the first *Suzaku* pointing (left) and the *XMM* pointing (right). The models differ significantly in the *Nustar* energy range marked with the black bar.

the model including the additional Comptonization component. In addition, the high spectral resolution will help in the soft X-ray part putting firm constraints on the smoothness of the X-ray excess.

Fairall 9, with its absence of warm absorption, is an interesting target to study the properties of the soft excess. This enables us to test possible scenarios explaining the soft excess in the spectrum, as well as the time variability of this component. We note that the shape of the additional soft excess seems to change as the source becomes dimmer (Fig 2.6). The dimmer the source the steeper the additional component. As the contribution of the additional component decreases, the lower ionized reflection starts to dominate. A more detailed analysis of this phenomenology could lead to more insight into the nature of this additional component but requires more high quality pointings and is therefore subject to future studies.

As a final comment, we highlight that the Suzaku-B pointing needs to treated carefully and the cross normalization between XIS and HXD-PIN cannot be expected to be at normal value but instead is found to be higher (1.3). We note that the reported discovery by Tatum et al. (2012) of a new spectral component that only reveals itself in the PIN-band of this particular dataset (and interpreted as a transitory marginally Compton-thick absorber) may be affected by this incorrect cross-normalization.

Chapter 3: An X-ray View of the Jet-Cycle in the Radio Loud AGN 3C120

3.1 Generation of jets in Broad Line Radio Galaxies – The jet cycle

One of the most enduring questions surrounding AGN is the origin of powerful, relativistic, radio-emitting jets in some AGN. A closely related question concerns the extent to which we can draw an analogy between jets from stellar-mass black hole systems (particularly the Galactic microquasars, see below) and AGN. In recent years it has become clear that many aspects of black hole accretion and jet formation are directly comparable between AGN and the lower-mass (about $10\,M_{\odot}$) black holes in X-ray binary systems (XRBs) (Merloni et al., 2003; McHardy et al., 2006; Fender et al., 2007). This is to be expected given the very simple scalings with mass for black holes in general relativity, although there is likely to be a larger diversity of environments and fueling mechanisms in AGN compared with XRBs. XRBs can be observed as they cycle (secularly) through different accretion states, and we find that the properties and even the existence of the jets is closely tied to the accretion state (characterized by the spectral and timing properties of the X-ray emission) (Belloni, 2010). Importantly, it has been shown that XRB jets manifest themselves in two types depending upon the spectral state of the XRB. The first kind of jet is seen in the hard (corona dominated) spectral state as a continuous low-power outflow (Remillard & McClintock, 2006). The second type of jet, which is similar to the jets seen in broad line radio galaxies, is launched when a low-mass XRB undergoes a transient outburst (Fender, Belloni & Gallo, 2004). The jet is usually observed close to the time of outburst maximum, as the source moves from the hard state to the soft (disk dominated) state (Fender et al., 2009; Miller-Jones et al., 2012). Low-mass black hole XRBs displaying these powerful jets are called microquasars (Mirabel & Rodríguez, 1999).

Assuming that these transient XRB jets and those from BLRGs are fundamentally the same phenomenon, the study of jets in AGN and XRBs give us different and complementary views of the physics. One major result learned from studying XRB jets is that the jet power, as well as the radiative efficiency of the accretion flow, can change dramatically in the same source at the same overall radiative luminosity on timescales far shorter than those associated with significantly changing black hole mass or angular momentum (Corbel et al., 2013). On the other hand, the much longer timescales displayed by AGN allow us to follow the complex relationships between individual jet-ejection events and the accretion disk, something which is difficult in XRBs.

It is now recognized that both Galactic microquasars and luminous radio-loud AGN (RLAGN) display complex cycles. In BLRGs, as first found by Marscher et al. (2002) in 3C120, major jet ejection events are preceded by strong dips in the X-ray luminosity. Since the X-ray emission in BLRGs is thought to be dominated by the corona of the inner accretion disk, as shown for 3C120 by Marshall et al. (2009), this X-ray/radio connection conclusively demonstrates a link between changes in accretion disk structure and powerful ejection events. This behavior, which has parallels in the phenomenology of Galactic microquasars, is one of the few observational clues that we have to the origin of radio jets. For example, GRS 1915+105 has been found to launch a relativistic jet knot as the inner edge of the accretion disk moves all the way to the ISCO (Fender, Belloni & Gallo, 2004). This general idea has been confirmed in much more extensive monitoring campaigns of 3C120 and 3C111 by Chatterjee et al. (2009, 2011) who also show that an observed correlation between the X-ray and optical flux can be explained in terms of the (inward or outward) radial propagation of powerful disturbances within the accretion disk (McKinney & Blandford, 2009). We note that Tombesi et al. (2011, 2012) recently reported a possible disk-outflow connection from a *Suzaku* spectral analysis of 3C111 and compared this to events in the radio jet.

On the basis of these BLRGs studies, the current picture is that the jet and disk are linked via a “jet cycle”, summarized in cartoon form in Fig. 3.1. The cycle starts with a full accretion disk extending all the way to the ISCO (Step 1). Some instability, possibly associated with a breakdown in the inertial confinement of the magnetic flux bundle threading the black hole (Reynolds, Garofalo & Begelman, 2006; McKinney, Tchekhovskoy & Blandford, 2012), destroys the innermost regions of the disk and ejects matter out of the disk plane (Step 2), causing an X-ray dip. This triggers a powerful relativistic mass/energy ejection along the jet which, with a time delay corresponding to propagation and optical depth effects, results in a radio flare and the creation of a new jet knot/shock (Step 3). One possibility is that this ejection event is triggered by the re-accretion of open magnetic field lines onto the rotating event horizon. Lastly, the inner accretion disk refills (Step 4) and the cycle repeats.

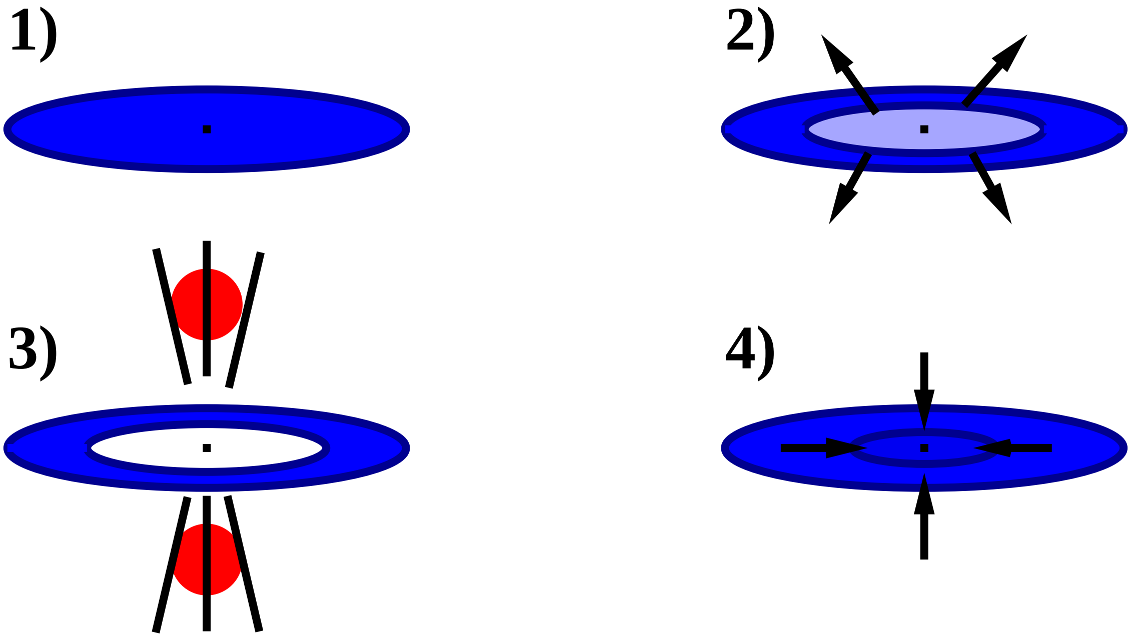

Figure 3.1: Summary of our current understanding of the four steps of the jet cycle; 1) the accretion disk is full, 2) inner disk becomes instable, 3) jet is formed, 4) disk refills. A more detailed description of the jet cycle can be found in the text.

Relativistic X-ray reflection and, in particular, the broad iron line gives us a powerful tool to study the inner regions of AGN accretion disks (Tanaka et al., 1995; Fabian et al., 1995; Reynolds & Nowak, 2003; Reynolds et al., 2012). If our hypothesis of the jet-cycle in BLRGs is correct we would expect to see relativistic disk reflection during periods when the inner accretion disk is filled. When the inner disk is destroyed, we should see indications for a truncation of the disk. Confirming this prediction would provide a major boost to the current jet formation scenario. Measuring the inner radius of the accretion disk during several phases of the jet cycle will help to anchor this scenario.

In this work we study 3C120, a nearby ($z = 0.033$) and X-ray bright BLRG with a bulge dominated host, showing signs of a recent merger (García-Lorenzo et al., 2005). It is known to harbor a black hole with a mass of $(5.7 \pm 2.7) \times 10^7\,\mathrm{M}_\odot$ (Pozo Nuñez et al., 2012). 3C120 has been studied in detail at many wavelengths (e.g., Chatterjee et al., 2009) and is well known to show a one sided superluminal jet. It also exhibits a prominent jet cycle (Marscher et al., 2002), that has been previously studied multiple times in the X-ray range. Earlier *XMM* observations analyzed by Ballantyne, Fabian & Iwasawa (2004) and Ogle et al. (2005) find that the X-ray spectrum above 3 keV can be well described by a power law and cold reflection, when accounting for neutral intrinsic absorption in the object. At soft energies they found a soft excess, which can be described by bremsstrahlung, or a power law. Kataoka et al. (2007) used *Suzaku* data from 2006 and found indications for relativistic disk emission in the X-ray spectrum. These are confirmed by Cowperthwaite & Reynolds (2012), who find evidence for a truncation of the accretion disk in a re-analysis of the same dataset with updated models and calibration.

From radio observations of superluminal motion and modeling of the recollimation shock, the jet angle has been estimated to be about 16 degrees (Agudo et al., 2012). With the caveat that the truncation of the thin disk may influence the ability of GR torques to align the inner disk, we assume a Bardeen-Petterson alignment of the jet and the inner accretion disk (Bardeen & Bardeen, 1975) implying that the jet inclination can also be taken as the inner disk inclination. This, together with the fact that the UV/optical flux seems to mostly originate from the accretion disk (Ogle et al., 2005), makes 3C120 very suitable for studying potential changes in the accretion disk as expected from a disk-jet connection. It is also important to note that 3C120 was detected with *Fermi*, allowing a tentative decomposition of the radio-to-γ spectral energy distribution (SED) into jet and disk components (Kataoka et al., 2011). This very simple decomposition suggests that the jet completely dominates the radio and γ-ray emission as expected, but is only a $\sim 10\%$ contributor to the optical, UV and X-ray emission. Given that the tentative decomposition suggests that $10\,\%$ of the X-ray flux comes from the jet, the much more careful treatment we undertake is needed to determine whether the jet's flux can be ignored in fitting the X-ray spectrum or not.

In this chapter, we test the jet-cycle picture using a detailed spectral analysis in the X-ray band supported by a multi-wavelength analysis in the optical/UV and radio. A multi-epoch analysis of *XMM-Newton* and *Suzaku* spectra shows that, judged on purely statistical grounds, there are degenerate phenomenological interpretations of the X-ray spectrum, one of which does not require any relativistic disk reflection component. However, physical considerations lead us to prefer a model in which the soft X-ray excess is a mixture of (steep) jet-emission and blurred ionized disk reflection. Within the context of this model, we do indeed find evidence for changes in the inner accretion disk structure in the sense expected from the jet-cycle picture. Additionally, we investigate the X-ray spectral variability on the timescale of a few hours, enabling us to tap into timescales comparable to the orbital time of the inner accretion disk and unobservable in X-ray binaries. We suggest that the observed rapid X-ray spectral variability corresponds to magnetically mediated disturbances propagating from the disk (and/or disk corona) into the jet flow.

The chapter is organized as follows: First, we describe the datasets used in this work and briefly discuss the data reduction techniques (§3.2). After placing the observations in the context of the jet cycle (§3.3) and performing a preliminary, basic investigation of spectral shape of the individual data epochs, a multi-epoch analysis is used to investigate the nature of the X-ray spectrum (§3.4). We then investigate the short-term variability and spectral energy distribution to further enhance our understanding of the processes driving the production of X-ray radiation in this AGN. We end with a brief discussion of the implications for jet formation that can be drawn from the observations (§3.6). Throughout this chapter, luminosities and distances are calculated using a ΛCDM cosmological model with $H_0 = 71\,\mathrm{km\,s^{-1}\,Mpc^{-1}}$, $\Omega_\Lambda = 0.73$ and $\Omega_M = 0.27$ (Komatsu et al., 2011). For a redshift of $z = 0.033$, this results in a luminosity distance to 3C120 of 143 Mpc and an angular size distance of 134 Mpc.

3.2 Observations & Data Reduction

The goal of this chapter is a detailed analysis of the physical processes operating in the central engine of 3C120. To obtain this complete picture we conduct sensitive spectroscopy with *XMM-Newton* and *Suzaku*, which is placed in context by *RXTE*, *Swift* and VLBA monitoring data. Below we describe the datasets that are considered and how they were reduced.

Table 3.1: Overview of observations and exposures.. Superscript^{a} denotes that XIS0/XIS3 were used. All *Suzaku* data were obtained after the failure of XIS2.

Observatory	Instrument	Date	ObsID	Exposure [ksec]
Suzaku (B)	XIS^{a}	2012/02/14	706042020	181.4
Suzaku (A)	XIS^{a}	2012/02/09	706042010	280.2
XMM-Newton	EPIC-pn	2003/08/26	0152840101	89.2

3.2.1 Data Reduction

3.2.1.1 Suzaku & XMM

The datasets analyzed in this chapter are from deep pointings by *XMM-Newton* and *Suzaku*. The *XMM* data have already been analyzed by Ballantyne, Fabian & Iwasawa (2004) and Ogle et al. (2005). A summary of the observations (re-)analyzed here is presented in Table 3.1. The two *Suzaku* pointings were taken as part of the *Suzaku AGN Spin Survey*, a cycle 4–6 Key Project (PI Reynolds).

The Suzaku data were reduced with HEASOFT v6.12 and calibration files dated 2009 September 25. During our observations, XIS was operated in full-window mode. In preparing the XIS spectra, we first reprocessed and screened the data using `aepipeline` and the standard screening criteria, as listed in the *Suzaku* ABC Guide. We then created individual spectra using `xselect` and response files using `xisrmfgen` and `xissimarfgen` tools for each detector and data mode combination.

The regions used for source and background are circular with radii of 3.8' and 1.7' respectively for Suzaku A and 4.2' and 1.6' for the Suzaku B observation. Later the spectra of different data modes were combined for each XIS. While this is the recommended standard procedure to create XIS spectra, one additional complication needs to be accounted for in our case. XIS spectra are contaminated by absorption from a hydrocarbon layer residing on the optical blocking filter and we must take measures to correct for this contamination. The contamination is monitored by the *Suzaku* team, and a correction is part of the construction of the standard effective area file. At the time of our analysis, this contamination model was in the process of being updated due to inconsistencies with recent XIS observations. We were able to use a test version of the contamination model in our analysis; for observations after 2010, this version is identical to the model incorporated in the CALDB files ae_xi?_contami_20120719.fits, released by the XIS team as part of the 20120902 CALDB release[1].

For the *Suzaku* data considered in this work, we found that we were unable to utilize data from the PIN detector due to the increased thermal noise caused by an increase in the leakage current. While the problem is most apparent for temperatures above -11 C, we already notice the effect (in terms of a distortion of the lower energy portion of the PIN spectrum) at temperatures of about -14 C, the PIN temperature during our observation.

The *XMM-Newton* dataset was reduced using XMMSAS 11.0.0. The EPIC data were first reprocessed, using the calibration files as of February 2012. The

---

[1] http://heasarc.gsfc.nasa.gov/docs/suzaku/analysis/xis_contami2012.html

spectra were then extracted using the tool `evselect`, selecting the default grade pattern. Source spectra are taken from a circular region with radius 41.2" centered on the source and the background spectra from an also circular region on the same chip with radius 28.9". The effective area files were generated using the XMMSAS task `arfgen`, and the redistribution matrices were produced using the task `rmfgen`. The EPIC detectors were operated in small window mode during the observation to reduce possible pile-up. During the observation, MOS1 was operated in timing mode. MOS2 alone has only ~1/3 the effective area of EPIC-pn in the iron K region. Assessing possible pile-up effects using the single, double, triple and quadruple event pattern versus the predicted fractions utilizing `epatplot`, shows that EPIC-pn is not affected by pile-up while EPIC-MOS is influenced by pile-up. Considering these facts, we only consider EPIC-pn data for the analysis performed in this chapter, as MOS2 would not significantly contribute to any constraints. The average observed net pn and MOS source count rates are $14.2\,\mathrm{cts\,s^{-1}}$ and $5.8\,\mathrm{cts\,s^{-1}}$ respectively.

For the spectral analysis, all XIS/EPIC-pn spectra were binned to a signal-to-noise ratio of 10. The considered energy ranges are 0.7-1.7 keV and 2.3-10 keV for *Suzaku*-XIS, with the energies around 2 keV being excluded because of known calibration issues around the mirror (gold) and detector (silicon) edges. The EPIC-pn spectrum is used in the 0.5-10 keV band. We extended all energy grids to energies far beyond the upper energy limit given by the highest data bin considered in fitting, in order to enable a proper model evaluation of the relativistic blurring.

In any detailed spectral analysis such as is presented in this chapter, we must be cognizant of the possibility of instrumental calibration errors. Such errors would directly lead to systematic errors in our spectral fits. The absolute flux calibration of X-ray observatories can be uncertain to $\sim 10\%$, but *our* physical conclusions derive purely from the *shape* of the spectrum and hence we need only be concerned with the relative calibration. As already mentioned, our *Suzaku* spectra are clearly inflicted by significant unmodeled calibration features around the silicon K-edge and the gold M-edge; we remove these energies from consideration by masking data in the 1.7–2.3 keV band. Our choice of low-energy cutoffs (0.5 keV and 0.7 keV in *XMM-Newton* and *Suzaku* respectively) is also driven by the need to exclude more poorly calibrated regions of the spectrum. However, due to the lack of a practicable approach for propagating calibration uncertainties into the systematic error budget for our complex (large parameter space) spectral models, no further attempt is made in this chapter to account for calibration uncertainties. We note that the relevant calibration errors are thought to be small — at the time of writing, the *XMM*/EPIC has a maximum error in the relative effective area of 5 % (with an rms error that is rather smaller) and a maximum error in the absolute energy scale of 10 eV [2]; for *Suzaku* the maximum error on the energy scale is also 10 eV and the effective area uncertainty is small outside of the mirror edges [3].

3.2.1.2 RXTE

A primary goal of this chapter is to investigate changes in the accretion disk structure during the jet-cycle in 3C120. Hence, we require monitoring data to

---

[2] http://xmm.vilspa.esa.es/docs/documents/CAL-TN-0018.pdf

[3] http://web.mit.edu/iachec/meetings/2012/Presentations/Miller.pdf

diagnose the state of the source at the time of the deep spectroscopic observations by *XMM-Newton* and *Suzaku*. For the period 2002–2008, this monitoring was provided by *RXTE*. The average cadence of the monitoring over this period is 4 days, with the exception of a 2-month period each Spring when 3C120 lies too close to the Sun. We have obtained these data from the HEASARC archives and reduced them exactly as described in Chatterjee et al. (2009). Only data from the top layer of proportional counter unit 2 were used. For each pointing, we produce a background-subtracted PCA spectrum using the appropriate epoch-dependent background/response files. The fluxes quoted below were obtained from the spectra for each pointing, assuming a simple power-law continuum with a neutral absorption column of $1.23 \times 10^{21}\,\mathrm{cm}^{-2}$ (Elvis et al., 1989). We do not consider any *RXTE* intra-pointing variability in this work. The resulting *RXTE* lightcurve is shown in Fig. 3.2.

3.2.1.3 Swift

Monitoring from *RXTE* is not available after 2008. Thus, we established a monitoring campaign with *Swift* to support the 2012 *Suzaku* pointings. XRT and UVOT data from this campaign are used in this chapter. The source can achieve X-ray flux levels that would lead to significant photon piled up in the XRT if operated in photon counting mode. To reduce the impact of pile-up we preferred to use the windowed timing mode data when available and otherwise excluded the central region of the PSF to mitigate pile-up. The *Swift*-XRT data were first reprocessed to apply the newest calibration (XRT Calibration Files: 20120830). From the resulting

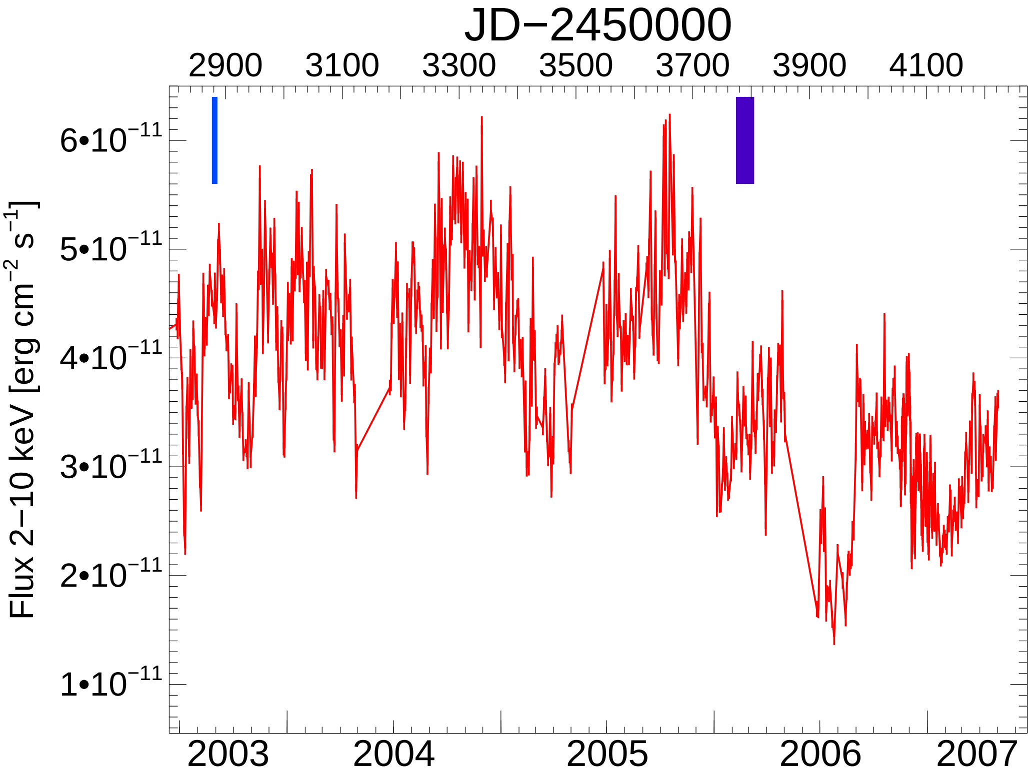

Figure 3.2: Long term *RXTE*-PCA monitoring for the 2–10 keV flux, marked are the positions of the 2003 *XMM* pointing and the position of the 2006 *Suzaku* pointings.

event file, a spectrum was extracted using XSELECT following a standard extraction for the windowed timing mode as described in the "XRT User's Guide"[4]. To properly account for the rolling of the satellite during the pointings (especially important in windowed timing mode), a spectrum is reduced for each good time interval with a different roll angle. Finally, these good time interval spectra are summed to yield the final spectrum for each pointing. As with the *RXTE* monitoring, X-ray fluxes are derived on the basis of a simple power-law continuum with a neutral absorption

---

[4] http://heasarc.nasa.gov/docs/swift/analysis/xrt_swguide_v1_2.pdf

column of $1.23 \times 10^{21}\,\mathrm{cm}^{-2}$.

The UVOT analysis is based on level II products. Each individual UVOT filter data file contains, in general, a number of exposures which were summed using the tool UVOTIMSUM. The UVOTSOURCE tool was then used to extract magnitudes from simple aperture photometry. Source and background regions were created for this purpose, with the position of the source region being obtained from the NASA Extragalactic Database (NED) in the first instance. The required source region and background region where both circular with a 4.8 arcsec radius.

The resulting UV and X-ray lightcurves from *Swift* are shown in Fig. 3.3.

3.2.2 VLBA

We observed 3C120 nine times with the Very Long Baseline Array (VLBA) between 2012 January 27 and 2013 January 15 at a frequency of 43 GHz. The observations, part of the Boston University γ-ray blazar monitoring program (www.bu.edu/blazars) included ten 3-5 minutes scans on 3C120 at each epoch. The raw data were recorded at each antenna and correlated at the National Radio Astronomy Observatory's Array Operations Center in Socorro, NM. The resulting data on the *uv*-plane were edited, calibrated (including sky opacity corrections and fringe fitting), and imaged in a standard manner with routines from the Astronomical Image Processing System and Difmap software packages. This involved an iterative procedure alternating imaging the CLEAN algorithm with self-calibration of both phases and intensities, which eventually converged to the final images. The resulting images, with an an-

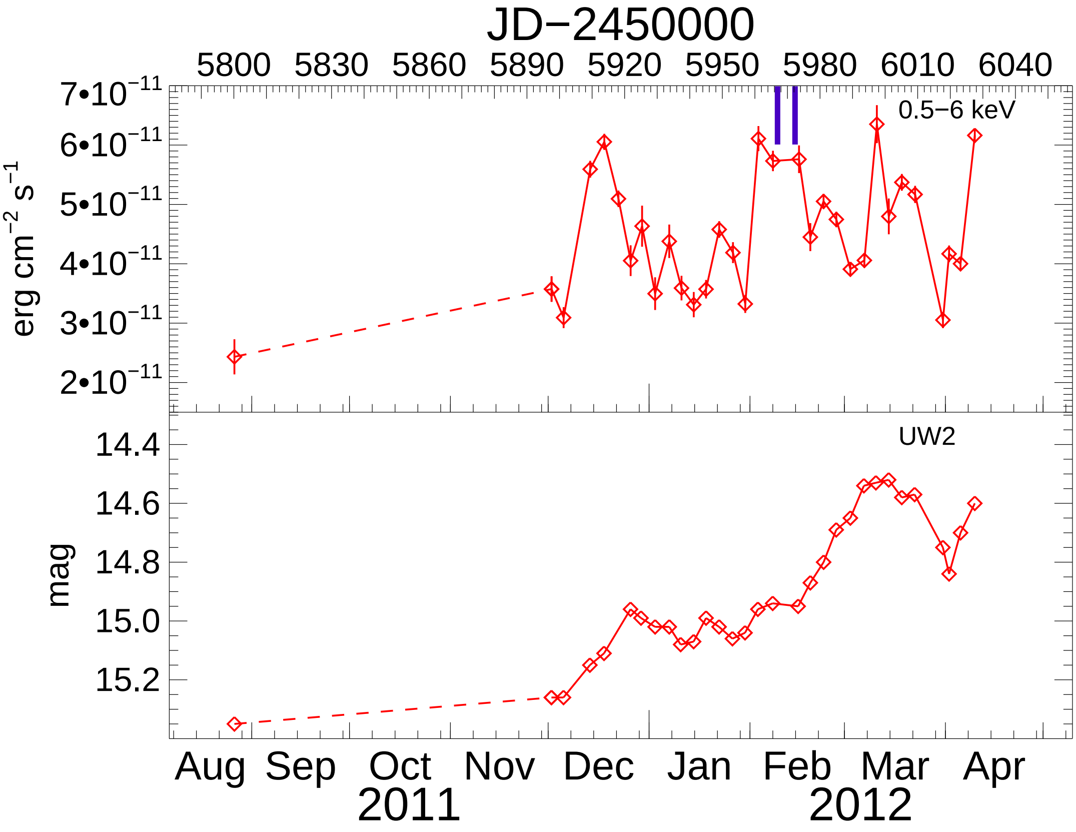

Figure 3.3: *Swift* monitoring of 3C120: X-ray and UV (UW2 filter) results. The markers point out the beginning of the two parts of the deep *Suzaku* stare.

gular resolution of 0.14 milliarcsec along the direction of the jet, are displayed in Figure 3.4. They reveal the appearance of a new superluminal knot, which we designate *K12*, with a proper motion of 1.14 ± 0.22 milliarcsec yr^{-1}, corresponding to $2.6 \pm 0.5c$ at the distance of 3C120. The centroid of the knot crossed the centroid of the “core” (the bright, presumed stationary feature at the eastern end of the jet) on JD 2456001 ± 10 (March, 14th 2012). Another development is the enhanced brightness of the jet between 0.2 and 0.5 milliarcsec from the core that is apparent starting with the 2012 August 13 image. This feature is either stationary or moving subluminally.

3.3 The Observations in Context

As outlined above, we need to estimate the placement of each of our spectroscopic observations in the jet-cycle. The long-term lightcurve taken by *RXTE*, previously published by Chatterjee et al. (2009), clearly shows the pattern of X-ray dips and recovery associated with the jet cycle (Fig. 3.2). We mark on Fig. 3.2 the time of the *XMM* pointing considered in this work. This reveals that the pointing was on the peak of the flux sequence, corresponding, according to the model, to a radiatively-efficient disk extending down close to the black hole (Step 1 of Fig. 3.1). Also marked is the position of the 2006-*Suzaku* observation as analyzed by Kataoka et al. (2007) and Cowperthwaite & Reynolds (2012) which occurred during a period of rising X-ray flux. As it was already re-analyzed recently we decide to not include it in our spectral analysis. This rising flux may correspond to a refilling accretion disk (Step 4 of Fig. 3.1), in line with the truncated accretion disk ($r_{\text{in}} \sim 10R_g$) found by Cowperthwaite & Reynolds (2012).

The *Swift* monitoring campaign supported the new 2012-*Suzaku* pointings. The monitoring (Fig 3.3) shows that the general trend in the UV band was a rising flux, with some temporary stalling of the rise. The X-ray variability is less coherent, showing indications for short-lived flux dips, but appears to show a rising trend. The X-ray flux is estimated by fitting an absorbed power law with the absorption column fixed to $3.1 \times 10^{21}\,\text{cm}^{-2}$ (a value similar as the one found later for the best fit to the *Suzaku* pointings). Similar short-timescale X-ray variability appears when zooming into the *RXTE* X-ray monitoring; see Figure 1 of Marshall et al. (2009).

The VLBA monitoring also helps to place the 2012-*Suzaku* observations into context. The superluminal knot appears approximately one month after our *Suzaku* pointing. However, the work of Chatterjee et al. (2009) shows that there is approximately a 2 month delay between the probable time of the physical ejection from close to the black hole and the appearance of a new VLBA knot, most likely corresponding to the propagation time of the ejector between the black hole and the VLBA core. Accounting for this time delay, we estimate that the actual ejection occurred approximately one month prior to the *Suzaku* pointings. Hence, the prediction is that *Suzaku* should find a truncated/refilling accretion disk.

In summary, on the basis of the *RXTE*, *Swift* and VLBA monitoring together with the jet-cycle hypothesis, the 2003-*XMM* pointing should show a filled accretion disk extending all the way to the ISCO. During the two *Suzaku* pointings on the other hand we expect the accretion disk to be still truncated but be in a stage of refilling.

3.4 Spectral Analysis

We begin by discussing our detailed analysis of the deep spectral *XMM-Newton* and *Suzaku* data. Our main technique is a "multi-epoch analysis" in which all spectral data are fitted together, tying together parameters that must (on physical grounds) be common across all epochs. However, we begin by discussing an initial exploration of the spectra and the construction of the spectral models. Throughout this work, the spectral analysis was performed with the Interactive Spectral Interpretation System[5] (ISIS Version 1.6.0-7; Houck & Denicola, 2000) using the newest *XSPEC* 12.0 models (Arnaud, 1996). All uncertainties are quoted at the 90 % confidence level for one parameter of interest ($\Delta\chi^2 = 2.7$). Systematic errors arising from the physical assumptions made in the models used for describing the spectra are not included in the given errors.

3.4.1 Initial Data Exploration and Model Construction

Investigating the spectral variability by looking at the hardness evolution within each *XMM* and *Suzaku* pointing, we find it is mild, and therefore ignore it in this Section. The short-term variability that we do find will be discussed in §3.5. To get a first look at the spectral shape, we fit a simple absorbed power law to the 2–4.5 keV data and then extend to the full energy range of the observation (Fig. 3.5). This reveals an iron line and an upturn at higher energies indicative of the presence of reflection in the spectra. Below 2 keV, additional absorption beyond

---

[5] http://space.mit.edu/cxc/isis

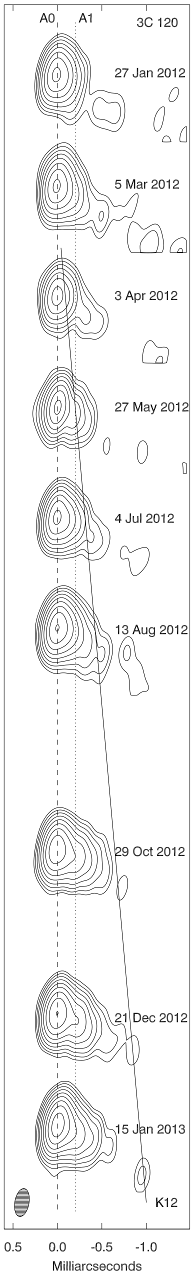

Figure 3.4: Time sequence of VLBA images at 43 GHz of 3C120 at nine epochs. Contours correspond to 0.5, 1, 2, ..., 64, and 90% of the maximum intensity of 1.8 Jy beam^{-1} (reached on 2013 January 15). The easternmost feature, the "core," is presumed to be stationary. Knot *K12* is marked, with a mean trajectory (shown by line) correponding to an apparent speed of $2.6 \pm 0.5\,c$ and an "ejection" date (when the brightness centroid of *K12* coincided with that of the core) of 2012 March 15 ± 10. The elliptical Gaussian restoring beam of FWHM dimensions 0.34×0.14 milliarcsec along position angle $-10°$ is displayed in the bottom left corner.

the Galactic column that is already accounted for is apparent.

Building upon this knowledge and previous works (Kataoka et al., 2007; Cowperthwaite & Reynolds, 2012), we construct three multi-component spectral models to describe our spectra. Common to all of these models is a primary powerlaw continuum with photon index Γ together with cold, distant reflection of that powerlaw described by the model `pexmon` (Nandra et al., 2007). The reflection fraction R and the iron abundance characterizing this reflection are left as free parameters. As some parameters for `pexmon` cannot be determined from our fits we need to fix them to certain values. We assume that the high-energy cutoff of the continuum powerlaw is 300 keV, which is well out of our fitting range. Since `pexmon` strictly models reflection from a planar surface, we also need to fix the inclination parameter of the `pexmon` model. The most likely geometries for the material producing the cold/distant reflection features are either cloud-like or a large-scale torus, and thus a range of inclinations will contribute to the observed spectrum. Assuming that this can be approximated as reflection from isotropically oriented planar segments, the most likely inclination angle is 60°. Thus, we set the inclination of the `pexmon` component to 60°. We have verified that this assumption does not drive any of the conclusions reached in this chapter — in particular, repeating the analysis presented in §3.4.2.3 using a `pexmon` inclination of 30° yields best fitting parameters that are within the statistical error bars of our canonical analysis, with the exception of the reflection fraction.

Also common to all of our spectral models is a photoionized emitter producing, most notably, Fe XXV/Fe XXVI iron-Kα lines. The photoionized emission

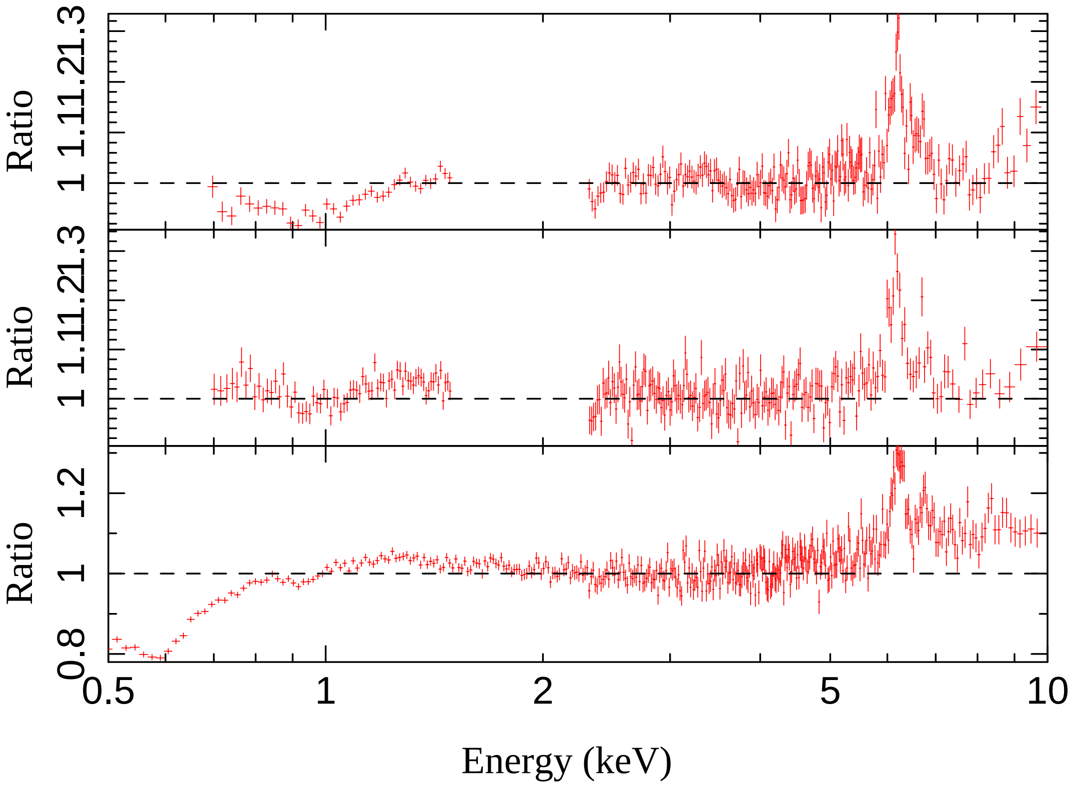

Figure 3.5: Residuals to a simple absorbed power law (*Suzaku* I [Top Panel], *Suzaku* II [Middle Panel] and *XMM* [Bottom Panel]) fitted from 2-4.5 keV; spectra are rebinned for plotting.

is parametrized by ionization parameter and normalization. It is described using a table model calculated using `xstar2xspec` from the `XSTAR` model `photemis`[6], assuming irradiation by a power law with $\Gamma = 2$ and a number density of $10^{10}\,\mathrm{cm}^{-3}$. The `xstar` model requires an assumed column density; we fix this to be $10^{22}\,\mathrm{cm}^{-2}$, noting that there is only a very weak dependence of the spectral shape on this column density. As noted in Chapter 2 there can be a strong degeneracy between Fe XXV and the blue wing of the broad iron line, therefore the inclusion of this component is crucial. Finally, photoelectric Galactic absorption ($N_{H,Gal} = 1.1 \times 10^{21}\,\mathrm{cm}^{-2}$, the

---

[6] http://heasarc.nasa.gov/docs/software/xstar/xstar.html

average value for 3C120 from HEASARC's nH Tool) is modeled with `TBnew`[7] a newer version of `TBabs` (Wilms, Allen & McCray, 2000) with cross sections set to `vern` and abundances set to `wilm`. We also account for intrinsic cold absorption in the source using `TBnew` with column density as a free parameter.

Our first spectral model is a "disk reflection model". To the above base model, we add a component describing relativistic reflection from the innermost regions of an ionized accretion disk. To describe the ionized reflection associated with reflection of the inner accretion disk, we used a modified version of `reflionx` developed by Ross & Fabian (2005), see Chapter 2 for details. The iron abundance is fixed to that characterizing the distant reflection (thus we assume a chemically homogeneous central engine; see Reynolds et al. 2012), and the photon index of the continuum irradiating the disk is tied to the one for the primary powerlaw. The ionized reflection component is then relativistically blurred using the model `relconv` (Dauser et al., 2010); this naturally gives rise to a relativistic iron line, blurred Compton reflection hump and a soft excess. The radial dependence of the emissivity of the reflection component is assumed to have a power-law form with index q. The inner edge of the X-ray reflection regime can be at the ISCO (Reynolds & Fabian, 2008) or further out, and the outer edge was fixed to $400\,R_{\rm g}$. Provided that $q > 2$, the relativistic blurring kernel is only weakly dependent upon this outer radius. The accretion disk inclination i and the black hole spin a were left as free parameters.

For a radio-loud AGN relativistic disk reflection is not the only possible origin for the soft X-ray excess. A contribution from the jet emission could also produce

---

[7] http://pulsar.sternwarte.uni-erlangen.de/wilms/research/tbabs/

an excess flux at soft energies. Thus, our second spectral model is a “jet model”. To the base model, we add a second (steep) powerlaw component with photon index Γ_S to characterize a possible contribution from the jet. As compared with the disk reflection model, this decouples the soft excess from the iron-K band structure. This is motivated by similar treatments in Kataoka et al. (2007) and Ballantyne, Fabian & Iwasawa (2004).

The final spectral model is the “disk+jet model” in which we include both a relativistic disk reflection component and a steep power-law.

3.4.2 Multi-Epoch Fitting

3.4.2.1 Relativistic disk reflection model

We fitted the disk reflection model to the *XMM-Newton* and *Suzaku* data employing multi-epoch fitting — all spectra are fitted together, tying together the black hole spin, accretion disk inclination, and iron abundance that on physical grounds should be constant across epochs. The ionization state and normalization of the photoionized emitter are also tied across epochs since it is believed that this component originates from a spatially extended structure. As a first approach, we assume that the inner radius of the accretion disk is fixed to the ISCO. We find an acceptable fit overall ($\chi^2/\mathrm{dof} = 4067/3875$ [1.05]) and report the spectral parameters in Table 3.2 (ordered by the flux sequence established in §3.3). As the source brightens in flux, the ionization state of the inner disk rises from $\xi \sim 10$ to $\xi \sim 5900$. Along with the ionization state, the contribution of ionized reflection

Table 3.2: Spectral Parameters for 3C120 multi-epoch disk-reflection model with inner disk radius fixed at the ISCO; see the text for a detailed description of the model. *Suzaku* spectra are normalized to XIS0 data. The power law normalization is photons $\mathrm{keV}^{-1}\,\mathrm{cm}^{-2}\,\mathrm{s}^{-1}$ at 1 keV. Bold values are the ones which are constrained by all observations as they are assumed to be constant.

		Suzaku A	Suzaku B	XMM
absorption continuum & cold reflection	$N_\mathrm{H}[10^{22}\,\mathrm{cm}^{-2}]$	$0.59^{+0.05}_{-0.08}$	$0.41^{+0.11}_{-0.08}$	$0.74^{+0.01}_{-0.02}$
	$A_\mathrm{pex}\ [10^{-3}]$	$14.34^{+0.11}_{-0.08}$	$15.38^{+0.15}_{-0.09}$	$1.27^{+0.09}_{-0.05}$
	Γ	$1.85^{+0.01}_{-0.01}$	$1.92^{+0.01}_{-0.01}$	$1.50^{+0.01}_{-0.00}$
	R	$0.37^{+0.06}_{-0.06}$	$0.39^{+0.08}_{-0.08}$	$2^{+0}_{-0.33}$
ionized reflection	$A_\mathrm{reflionx}\ [10^{-4}]$	$1.19^{+0.34}_{-0.33}$	$1.47^{+0.40}_{-0.41}$	$2.87^{+0.07}_{-0.05}$
	$Fe/Solar$		$\mathbf{0.96}^{+0.13}_{-0.08}$	
	$\xi\ [\mathrm{erg\,cm\,s^{-1}}]$	$10.0^{+7.7}_{-7.3}$	$10.0^{+3.7}_{-7.2}$	$5886.1^{+31.9}_{-85.3}$
relativistic blurring	q	$2.0^{+0.1}_{-0}$	$2.0^{+0.2}_{-0}$	$10^{+0}_{-5.4}$
	a		< 0.29	
	i [deg]		$\mathbf{60}^{+0}_{-2}$	
plasma	A_phot		$\mathbf{8.29}^{+38.85}_{-0.39}$	
	$\log\xi$		$\mathbf{6.2}^{+0.8}_{-0.0}$	
individual	χ^2/dof	1023.1/943	1199.6/1404	1844.1/1522
	χ^2/dof		4066.9/3875	
	χ^2_red		1.05	

to the X-ray spectrum increases from 2 % to 85 % based on the unabsorbed model fluxes in 0.7-10 keV. While, taken at face value, this makes the *XMM* spectrum reflection dominated, the actually visible absorbed flux is still dominated by the cold reflection and power law continuum. The accretion disk inclination determined from this fit is high and not consistent with the radio measurements ($\sim$ 16 deg), possibly highlighting a mis-modeling of the data. Another problem is the tremendous difference in the normalization of the corona between the *Suzaku* pointings and the *XMM* pointing, a factor of 10 seems physically hard to explain. This, in combination with

Table 3.3: Spectral Parameters for 3C120 multi-epoch disk-reflection model with free inner disk radius; see the text for a description of the model. *Suzaku* Spectra are normalized to XIS0 data. The power law normalization is photons $\mathrm{keV}^{-1}\,\mathrm{cm}^{-2}\,\mathrm{s}^{-1}$ at 1 keV. Bold values are the ones which are constrained by all observations as they are assumed to be constant.

		Suzaku A	Suzaku B	XMM
absorption	$N_{\mathrm{H}}[10^{22}\,\mathrm{cm}^{-2}]$	$0.63^{+0.07}_{-0.06}$	$0.51^{+0.07}_{-0.08}$	$2.32^{+0.07}_{-0.06}$
continuum &	$A_{\mathrm{pex}}\ [10^{-3}]$	$12.82^{+0.17}_{-2.51}$	$15.55^{+0.15}_{-0.11}$	$12.30^{+0.11}_{-0.15}$
cold reflection	Γ	$1.81^{+0.01}_{-0.01}$	$1.92^{+0.01}_{-0.01}$	$2.37^{+0.02}_{-0.01}$
	R	$0.41^{+0.03}_{-0.03}$	$0.40^{+0.09}_{-0.06}$	$1.83^{+0.13}_{-0.21}$
ionized reflection	$A_{\mathrm{reflionx}}\ [10^{-4}]$	$0.31^{+0.03}_{-0.07}$	$1.52^{+0.22}_{0.41}$	$27.18^{+1.33}_{-4.44}$
	$Fe/Solar$		$\mathbf{0.81}^{+0.01}_{-0.03}$	
	$\xi\ [\mathrm{erg\,cm\,s^{-1}}]$	$1998.9^{+563.5}_{-135.8}$	$14.2^{+6.1}_{-6.1}$	$196.78^{+5.33}_{-8.07}$
relativistic blurring	q	$10.0^{+0.0}_{-8.0}$	$2.4^{+0.2}_{-0.2}$	$6.97^{+0.09}_{-0.21}$
	a		$\mathbf{0.966}^{+0.003}_{-0.003}$	
	i [deg]		$\mathbf{5}^{+4}_{-0}$	
	R_{in}	$84.3^{+14.2}_{-42.4}$	$1^{+2.0}_{-0.0}$	$1^{+0.1}_{-0.0}$
plasma	A_{phot}		$\mathbf{4.6e\text{-}5}^{+7.96e-06}_{-7.4e-06}$	
	$\log\xi$		$\mathbf{1.0}^{+0.03}_{-0.005}$	
individual	χ^2/dof	1007.4/942	1199.6/1403	1647.2/1521
	χ^2/dof		3854.3/3872	
	χ^2_{red}		1.00	

the poor quality of the fit for the *XMM* spectrum and the low spin value ($a < 0.29$), could be an indication for a time variable recession of the accretion disk.

With these hints, we then allowed the inner radius of the accretion disk to vary across epochs (with the constraint that it is no smaller than the ISCO). Such a fit yields a significantly better goodness-of-fit ($\chi^2/\mathrm{dof} = 3854/3872$ [1.00]; $\Delta\chi^2 = 214.6$) while at the same time leading to more consistent results. The inclination is now limited to $i < 7$ degrees, more in line with the radio determination of $i <$

16 degrees. The inner radius clearly shows a flux state dependence with it being further out as the X-ray flux becomes smaller. However, it is surprising that the changes in the inner disk radius and disk ionization are of such a magnitude for the two *Suzaku* pointings considering the fact that they are separated by less than a week. The photon indices also show a trend with flux: the higher the flux the steeper the X-ray spectrum. Again, the contribution of ionized disk reflection to the X-ray spectrum increases from 8 % to 50 % based on the unabsorbed model fluxes in 0.7-10 keV. The determined spin parameter is high ($a > 0.96$). Similar to the fit with fixed inner radius, the iron abundance is sub-solar. The results are consistent with Cowperthwaite & Reynolds (2012), who for the earlier *Suzaku* pointings (also at time of rising flux) found a possibly recessed disk with high black hole spin. It is curious that the fit requires a significantly variable neutral absorption column, with an especially heavy column during the *XMM-Newton* pointing that absorbs a particularly strong soft excess originating from the ionized blurred disk reflection. See §3.6 for more discussion.

3.4.2.2 Jet model

A multi-epoch fit of the jet model gives $\chi^2/\mathrm{dof} = 3835/3881$ (0.99), a slightly better quality fit than obtained for the variable-R_{in} disk-reflection model. For the resulting spectral parameters (Table 3.4), we find that they are consistent with constant power law ($\Gamma = 1.97$) and reflection fraction ($R \approx 1.15$). In addition to this stable hard component the absorption in the Galaxy is also stable at about

Table 3.4: Spectral Parameters for 3C120 multi-epoch fit of the jet model; see the text for a description of the model. *Suzaku* Spectra are normalized to XIS0 data. The power law normalization is photons $\mathrm{keV^{-1}\,cm^{-2}\,s^{-1}}$ at 1 keV. Bold values are the ones which are constrained by all observations as they are assumed to be constant.

		Suzaku A	Suzaku B	XMM
absorption	$N_\mathrm{H}[10^{22}\,\mathrm{cm}^{-2}]$	$0.23^{+0.08}_{-0.08}$	$0.25^{+0.10}_{-0.11}$	$0.28^{+0.02}_{-0.02}$
continuum &	$A_\mathrm{pex}\ [10^{-3}]$	$16.20^{+0.60}_{-0.56}$	$17.01^{+0.76}_{-0.67}$	$15.31^{+0.45}_{-0.46}$
cold reflection	Γ	$1.96^{+0.03}_{-0.03}$	$2.01^{+0.04}_{-0.04}$	$1.97^{+0.03}_{-0.03}$
	R	$1.13^{+0.16}_{-0.15}$	$1.17^{+0.21}_{-0.19}$	$1.29^{+0.17}_{-0.16}$
	$Fe/Solar$		$\mathbf{0.28}^{+0.03}_{-0.03}$	
soft excess	Γ_S	$6.14^{+1.09}_{-0.38}$	$5.59^{+0.61}_{-0.33}$	$4.83^{+0.18}_{-0.19}$
	$A_\mathrm{pow}\ [10^{-3}]$	$2.86^{+2.49}_{-1.88}$	$4.99^{+3.49}_{-3.42}$	$7.15^{+0.58}_{-0.60}$
plasma	A_phot		$\mathbf{0.05}^{+3.24}_{-0.04}$	
	$\log\xi$		$\mathbf{4.2}^{+0.6}_{-0.0}$	
individual	χ^2/dof	988.1/946	1194.2/1406	1651.4/1523
	χ^2/dof		3834.5/3881	
	χ^2_red		0.99	

$2.5\times10^{21}\,\mathrm{cm}^{-2}$. The only variable part in the spectrum is the soft power law which changes from a slope of $\Gamma_S = 6.14^{+1.09}_{-0.38}$ to $\Gamma_S = 4.83^{+0.18}_{-0.19}$. The normalization at 1 keV also approximately doubles towards higher fluxes. This model does not include a disk reflection component. Within the context of this model, the "broad iron line" feature is described by a combination of the iron-K band "wedge" in the distant reflection component and the photoionized emission.

There are appealing as well as problematic aspects of this spectral solution. On the positive side, the intrinsic absorption is consistent with being constant ($N_H \approx 2.8\times10^{21}\,\mathrm{cm}^{-2}$) as is the reflection fraction ($R \approx 1.15$). More worryingly, the extremely steep soft powerlaw ($\Gamma_S \sim 5-7$) represents a fine-tuning problem. This is a steep component that strongly diverges just below our observed low-energy cutoff (0.7 keV for XIS and 0.5 keV for EPIC-pn). Although such an interpretation is not supported by the SED decomposition of Kataoka et al. (2011), one possible interpretation of such a steep continuum component is that we are catching the extreme (exponentially cut-off) end of the jet synchrotron spectrum. The question then becomes why this component cuts off at precisely this energy — a slightly lower cut-off energy would render it invisible in our X-ray spectrum whereas a high cut-off energy would cause it to completely dominate our soft X-ray spectra. Another troublesome issue is the low iron abundance implied by this fit ($Z \approx 0.28 Z_{\odot}$). It would be very surprising if the gas in the central regions of this evolved galaxy were not enriched to at least solar levels. Indeed, in many luminous Seyfert galaxies, central engine abundance enhancements to several times solar are inferred (Warner, Hamann & Dietrich, 2004; Nagao, Maiolino & Marconi, 2006).

3.4.2.3 Jet+disk model

Driven by the potential deficiencies of the "pure-bred" spectral models discussed above, we explore a mixed model in which we include both a jet component (i.e. an additional steep powerlaw continuum) and reflection from a relativistic disk. As must be the case (since this model-space completely encompasses the previous models), the goodness of fit parameter shows improvement, $\chi^2/\mathrm{dof} = 3802/3867$ (0.98); this improves on the jet-model by $\Delta\chi^2 = 32$ (for 14 additional parameters), and the disk-reflection model by $\Delta\chi^2 = 52$ (for 6 additional parameters). An ex-

Table 3.5: Spectral Parameters for 3C120 multi-epoch fit with the jet+disk model; see the text for a description of the model. *Suzaku* Spectra are normalized to XIS0 data. The power law normalization is photons $\mathrm{keV}^{-1}\,\mathrm{cm}^{-2}\,\mathrm{s}^{-1}$ at 1 keV. Bold values are the ones which are constrained by all observations as they are assumed to be constant.

		Suzaku A	Suzaku B	XMM
absorption	$N_\mathrm{H}[10^{22}\,\mathrm{cm}^{-2}]$	$0.14^{+0.02}_{-0.02}$	$0.18^{+0.05}_{-0.03}$	$0.28^{+0.01}_{-0.01}$
continuum &	A_pex $[10^{-3}]$	$10.16^{+0.89}_{-1.24}$	$13.19^{+0.62}_{-4.98}$	$7.25^{+1.48}_{-0.88}$
cold reflection	Γ	$1.70^{+0.75}_{-0.20}$	$1.81^{+0.03}_{-0.04}$	$2.40^{+0.01}_{-0.02}$
	R	$0.26^{+0.03}_{-0.04}$	$0.25^{+0.04}_{-0.06}$	$2.00^{+0.00}_{-0.23}$
ionized reflection	A_reflionx $[10^{-4}]$	$0.76^{+0.19}_{-0.16}$	$0.59^{+0.27}_{-0.20}$	$58.39^{+7.48}_{-7.41}$
	$Fe/Solar$		$\mathbf{1.67}^{+0.01}_{-0.08}$	
	ξ $[\mathrm{erg\,cm\,s^{-1}}]$	$199.7^{+9.8}_{-14.4}$	$123.5^{+40.9}_{-52.7}$	$199.0^{+8.3}_{-20.1}$
relativistic blurring	q	> 3.5	> 2.8	$7.8^{+0.3}_{-0.2}$
	a		$\mathbf{0.994}^{+0.002}_{-0.003}$	
	i [deg]		$\mathbf{5}^{+13}_{-0}$	
	R_in	$38.1^{+16.8}_{-20.4}$	$39.5^{+32.1}_{-26.2}$	$1.0^{+0.1}_{-0.0}$
soft excess	Γ_S	$2.64^{+0.11}_{-0.14}$	$3.80^{+0.37}_{-0.27}$	$3.56^{+0.14}_{-0.21}$
	A_pow $[10^{-3}]$	$5.47^{+0.45}_{-1.09}$	$5.89^{+1.18}_{-0.79}$	$6.23^{+0.04}_{-0.83}$
plasma	A_phot		$\mathbf{6.4e\text{-}5}^{+1.03e-05}_{-1.0e-05}$	
	$\log\xi$		$\mathbf{1.0}^{+0.04}_{-0.0}$	
individual	χ^2/dof	991.6/940	1185.0/1401	1625.8/1519
	χ^2/dof		3802.4/3867	
	χ^2_red		0.98	

ample of how the different components of this model are able to describe the data is shown in Fig. 3.6 for the first *Suzaku* pointing as well as the *XMM* pointing. We note that the broadening of the disk spectrum in case of *XMM* is so severe that the exclusion of the narrow 1.7-2.3 keV band from our *Suzaku* spectra does not strongly affect a possible detection of such a disk component.

Especially when comparing the jet model with the jet+disk model, an F-test shows that the improvement in the fit is not statistically significant. However, this mixed model solves most of the fine-tuning and physical-inconsistencies that have been noted for the pure-bred models. In this spectral solution, the jet component has a more modest photon index ($\Gamma_S \sim 2.5 - 4.0$), alleviating the fine tuning problem noted in §3.4.2.2. The disk component fits to an almost face-on inclination ($i < 18$ degrees) and the implied ionization state of the disk is approximately constant, alleviating the problems with the pure disk-reflection model. In particular, the large jump in the ionization state of the disk between Suzaku-A and Suzaku-B that was seen in the disk-reflection model is no longer present. This is straightforward to reconcile. As is evident in Fig. 3.5, there is a subtle but significant change in the soft excess between these two pointings. In the disk-reflection model, the soft excess is modeled as blurred ionized reflection and so this spectral change drives a strong change in the inferred disk ionization (even though the rest of the spectrum is very similar). In the mixed model, the soft excess change is entirely described by a change in the slope of the soft (jet) powerlaw, allowing the accretion disk parameters to remain almost unchanged.

More noteworthy is the fact that, in this mixed model fit, the intrinsic neutral absorption approximately halves (from $2.8 \times 10^{21}\,\mathrm{cm}^{-2}$ to $1.5 \times 10^{21}\,\mathrm{cm}^{-2}$) between the *XMM-Newton* observation in 2003 to the two *Suzaku* pointings in 2012. If we equate this nine year timescale with the dynamical time in the black hole potential $\left(t_{\mathrm{dyn}} = (R^3/GM)^{1/2}\right)$, this implies that the variable absorbing structures are at $10^4 R_g$, suggestive of the optical BLR.

In this scenario, the *XMM-Newton* spectrum is formally reflection dominated, with the ionized reflection from the inner accretion disk dominating the primary

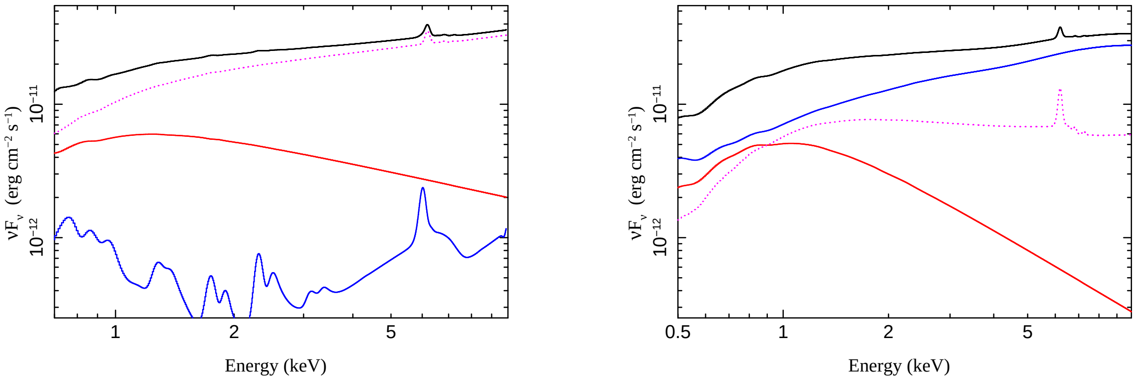

Figure 3.6: Examples for the spectral decomposition in the jet+disk model as found to be the best fit for the first *Suzaku* observation (left) and the *XMM* observation (right). Shown here is the total model (solid-thick black line), the primary power-law continuum and cold reflection (dotted magenta line), jet component (solid red line) and the relativistically blurred ionized reflection component (solid blue line).

continuum across most of the band. At the same time, the inner edge of the accretion disk is strongly constrained to be at the ISCO, the black hole is constrained to be rapidly spinning, and the emissivity index q becomes extremely steep ($q \approx 7.8$). All of this behavior is consistent with the extreme light bending of a primary X-ray source on the spin axis and very close to a rapidly spinning black hole (Miniutti & Fabian, 2004).

3.5 Short-Term X-ray Spectral Variability

After investigating the global long-term variability using long-term lightcurves (§3.3) and multi-epoch fitting (§3.4), it is important to note that there is shorter timescale (intra-observation) variability. The only significant short-timescale variability observed during the pointings considered in this chapter was found in the first *Suzaku* pointing, around the beginning of 12-Feb-2012 (Fig 3.7), in the form of a sudden increase in the count rates below 4 keV.

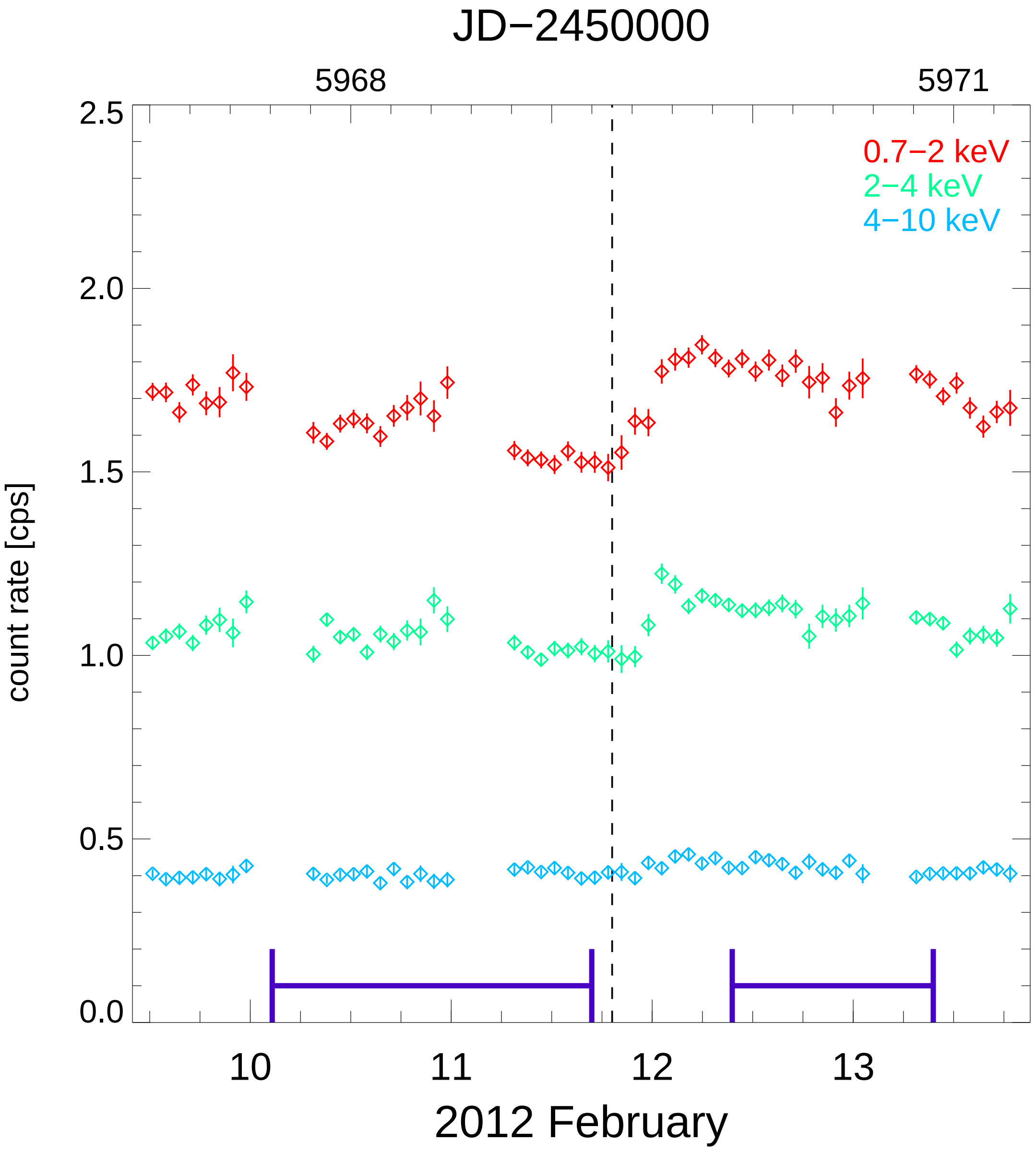

Figure 3.7: Zoom into parts of the XIS3 lightcurve of the the first Suzaku pointing in different energy bands. Blue lines represent the times from which the low and high state spectrum where constructed. The dashed line marks the approximate onset of the count rate jump in 0.7-2 keV.

To explore the nature of this variability we examine the development of the

4–10 keV/0.7–2 keV hardness ratio (Fig. 3.8). We see clear indications for spectral changes, starting even before the sudden count rate increase. A significant hardening of the source is observed in the time preceding the count rate jump. An examination of Fig 3.7 shows that the 4–10 keV flux jumps before the 2–4 keV flux which, in turn, peaks before the 0.7–2 keV band. This increase of the 4-10 keV count rate before the increase of the softer bands explains the observed hardening. Two possibilities for this sudden hardening and subsequent softening come to mind. Either the absorption column suddenly increases and then progressively decreases (successively uncovering softer energies) or there is a real change in the continuum shape (with the soft energies lagging the hard band). To investigate the nature of the variability in more detail, we construct pre-jump and post-jump spectra. The portions of the lightcurve used for pre-jump and post-jump are indicated in Fig. 3.7. The spectra can be described by an absorbed power law with a gaussian line as neutral iron K. The quality of the data does not allow us to constrain the absorption and the spectral slope to a degree where we could know which of the two is changing. However, varying only one of the two options we find that adjusting only the absorption leads to a worse fit than allowing for a change in photon index. This is also apparent from the contour plot (Fig. 3.9) of N_{H} versus Γ which suggests that the continuum slope is varying.

As discussed in §3.4.2, acceptable spectral models attribute at least some of the soft excess to a steep powerlaw-like component from a jet. Thus, while difficult to prove from this one event, we may be witnessing the propagation of a disturbance from the inner accretion disk into the jet. We discuss this possibility further in §3.6.

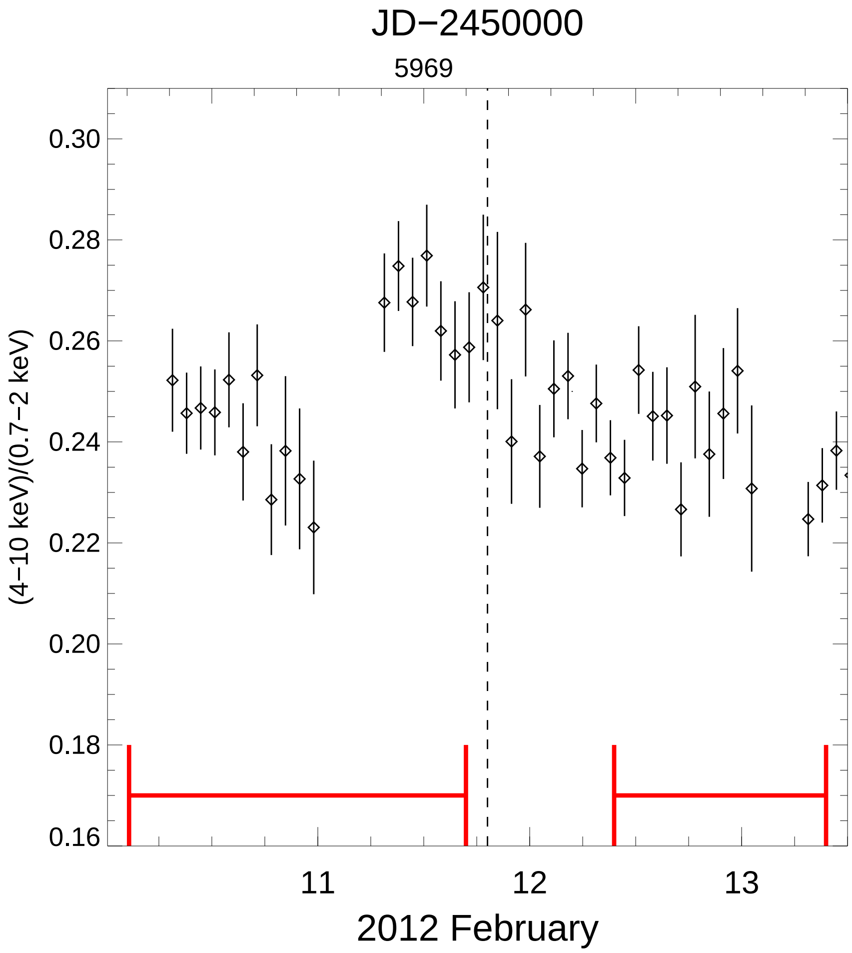

Figure 3.8: Hardness evolution ((4-10 keV)/(0.7-2 keV)) during the count rate jump in the *Suzaku* I pointing. The red lines represent the times from which the low and high state spectrum where constructed. The dashed line marks the approximate onset of the count rate jump in 0.7-2 keV.

3.6 Discussion

3.6.1 Evidence for a Disk-Jet Connection in 3C120?

Our preferred spectral model to describe the multi-epoch *XMM-Newton* and *Suzaku* data is the jet+disk model (see discussion in §3.4.2.3). The fits of this model to the data directly support the predictions of the jet-cycle model. We find a recessed accretion disk ($R_{\rm in} \approx 20 - 70 R_{\rm isco}$) during the 2012-*Suzaku* observations when the X-ray flux is on a rising trend and the jet-cycle picture would suggest a refilling accretion disk. This scenario is supported by a rising trend in the UV flux. It is likely that most of UV/optical flux in 3C120 is coming from the disk as the measured polarization is low (Chatterjee et al., 2009), so again the UV rise suggests a refilling accretion disk. On the other hand, we find that the disk extends all of the way to the ISCO and is strongly irradiated by a compact source close to the black hole during the *XMM-Newton* observation when the X-ray flux is at a peak. To fit this *XMM-Newton* spectrum, we require a rapidly rotating black hole. The formal limits indicate a truly extreme spin $a > 0.991$. However, our methodology implicitly assumes a razor-thin accretion disk (this assumption enters via the termination condition for the ray-tracing underlying the `relconv` relativistic transfer function, see Dauser et al. 2010). For such rapid spins, the ISCO is very close to the event horizon and finite disk-thickness effects must come into play. While more work is needed on this issue, a first attempt to explore the systematic errors introduced by finite-thickness effects was made by Reynolds & Fabian (2008) (see their Fig. 5). This suggests that the formal result of $a > 0.991$ may weaken to $a \gtrsim 0.95$ once finite disk thickness and emission within the ISCO is considered.

Our overall picture is supported by the appearance of a new superluminal knot in the jet in the VLBA images about one month after the 2012-*Suzaku* pointings and two months following the middle of the X-ray dip between JD 2455915 (December, 19th 2011) and 2455960 (February, 2nd 2012). The latter delay is similar to the mean

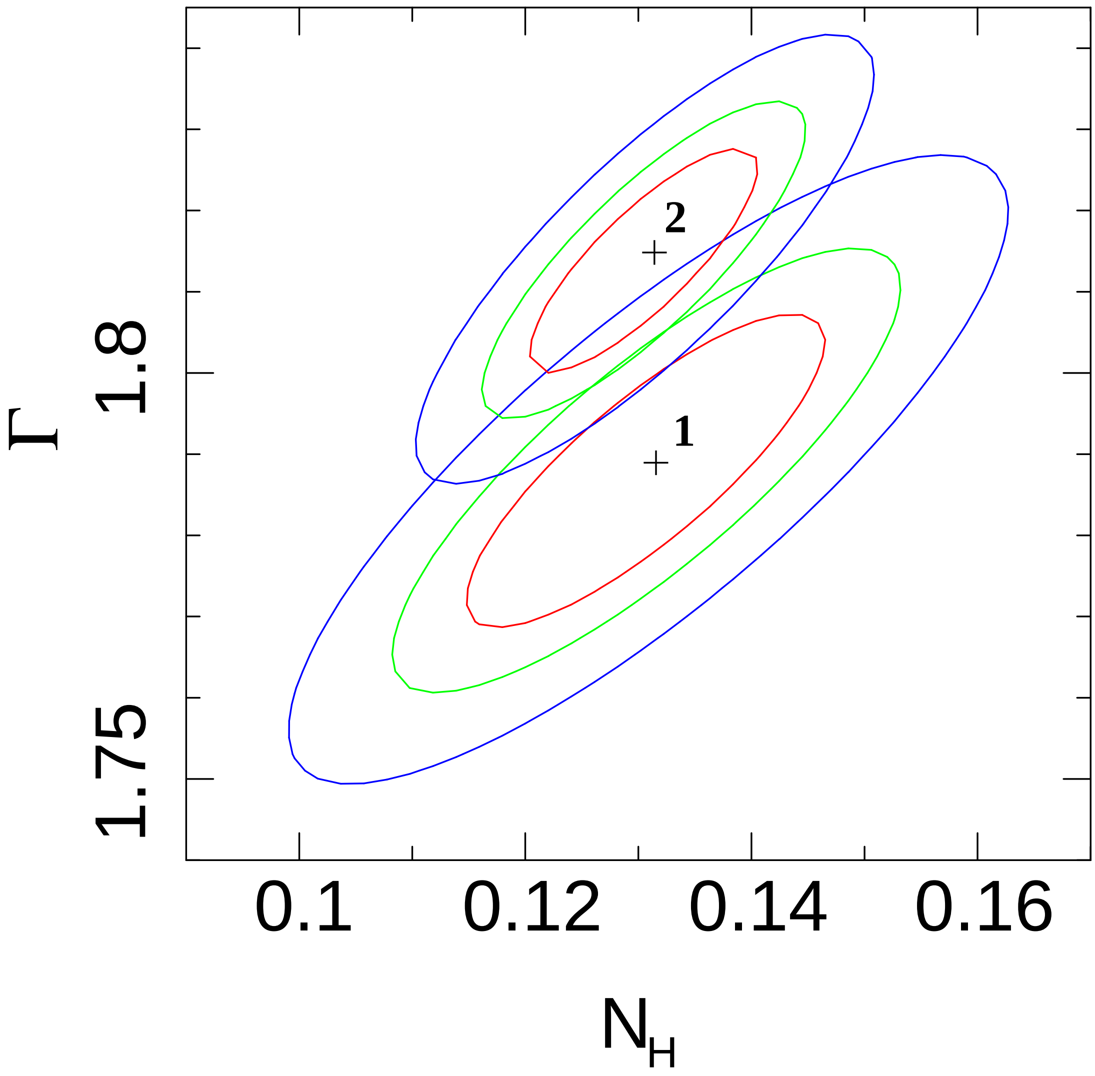

Figure 3.9: Contours of Γ and N_H (in units of $10^{22}\,\mathrm{cm}^{-2}$) for the pre-jump (1) and post-jump (2) spectra of the *Suzaku* I pointing.

value of 0.18 ± 0.14 yr observed over five years of *RXTE* and VLBA monitoring of 3C120 (Chatterjee et al., 2009). Marscher et al. (2002) and Chatterjee et al. (2009) interpret the delay as the travel time of a disturbance in the jet flow from the base of the jet near the accretion disk to the 43 GHz "core" about 0.5 pc away. The enhanced emission 0.2-0.5 mas from the core — and ~ 1 pc from the central engine — starting in 2012 August is too bright to be caused by "trailing shocks" (Agudo et al., 2001) behind the superluminal knot. A more likely explanation is either the establishment or strengthening of multiple standing shocks. Such shocks are set up by pressure imbalances with the external medium (Daly et al., 1988), which can occur when the energy density injected into the jet varies significantly with time (Gómez et al., 1997). Jorstad et al. (2005) detected such a stationary feature, designated *A1*, 0.2 milliarcsec from the core in 3C120 between 1998 and 2001. Figure 3.4 marks the location of *A1*, which is still present in 2012. The brightening of the core, which could be the first in a series of standing shocks, suggests that the rate of injection of energy did indeed increase starting in July 2011. Another apparently stationary emission feature appeared after this about 0.4 milliarcsec from the core. Unfortunately, our X-ray, UV, and optical observations ended several months before this occurred, hence we cannot determine whether a variation in the disk and corona emission heralded this change in the jet.

In our preferred X-ray spectral model, the soft excess is a combination of ionized reflection from the inner disk and a steep ($\Gamma = 2.5 - 4$) jet continuum. Within the context of standard jet emission models, such steep continua suggest that we are seeing the cut-off region of the jet synchrotron spectrum. Using the *XSPEC* model `srcut`, we have verified that our X-ray spectra would not have been sensitive to the curvature of this synchrotron spectrum since the jet dominates a narrow band at the lowest accessible X-ray energies. Extrapolating the synchrotron model to lower energies reveals that, in $\nu F(\nu)$ terms, the jet component should be approximately one order of magnitude brighter in the optical-UV band than the soft

X-ray. This is inconsistent with the SED of Kataoka et al. (2011); however, this SED was constructed from non-simultaneous data and hence must be viewed with caution. A simultaneous optical/UV/X-ray SED can be constructed from *Swift* UVOT+XRT data. Vasudevan & Fabian (2009) present exactly such a *Swift* SED, showing indeed that the optical/UV flux exceeds the X-ray flux by a factor of $10-20$. The existence of a broad-band spectral component extending from the optical/UV into the soft X-ray band is supported by the detection of a correlation between the UV/optical and soft X-ray flux within the *XMM* pointing (Ogle et al., 2005). Similarly, a weak correlation between the (1320 Å-1420 Å) band and the soft X-ray band (0.3-2 keV) has also been found previously by Maraschi et al. (1991) from simultaneous IUE-*Exosat* observations. This UV-soft X-ray correlation makes a Comptonization model for the soft excess similar to the one recently discovered in bright Seyferts (Lohfink et al., 2012b; Petrucci et al., 2012) also a possibility in 3C120, while at the same time ruling out a solely reflection-based soft excess. In our UV monitoring, we do not find a correlation between the UV flux and the 1-2 keV/0.3-1 keV X-ray hardness ratio (Fig. 3.10), as would be expected from a broad-band component. This absence could be explained in two ways: Firstly, a correlation on the timescales of the monitoring (one week) is not necessarily expected. Secondly, the average *XMM-OM* UW1 (2910 Å) flux was $6.6 \times 10^{-14}\,\mathrm{W\,m^{-2}}$, while our maximum UVOT-U flux (3465 Å) is only $2.9 \times 10^{-14}\,\mathrm{W\,m^{-2}}$ implying that the average flux values must be much lower. If part of this UV/optical flux is in fact a broad-band component its flux contribution could be too low during our monitoring to be detectable.

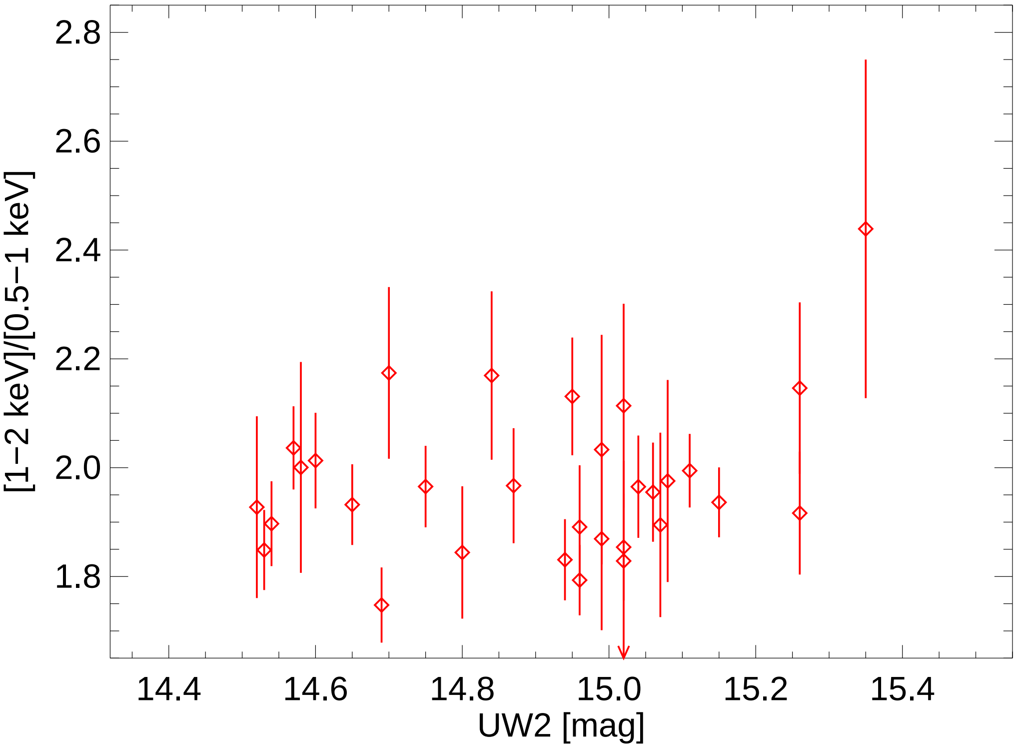

Figure 3.10: Soft X-ray hardness ((1-2 keV)/(0.3-1 keV)) versus UV magnitude in the UW2 band. No strong correlation is apparent between the two.

3.6.2 Variability

While the spectral analysis enables us to study the spectral components at any given time, variability studies can provide valuable additional information and put constraints on emission regions and the structure of the central accretion flow. Previous analysis of the long-term *RXTE* lightcurve by Chatterjee et al. (2009) showed that its PSD is similar to radio-quiet AGN, implying the origin of the X-rays may be similar. In agreement with this hypothesis, the spectrum softens as the source brightens (Ogle et al., 2005; Chatterjee et al., 2009), as is well established for Seyfert galaxies (e.g., see Chiang et al., 2000).

While this is all well-known, the considered timescales are rather long, making changes in the accretion rate a likely origin. However the *Swift* and *RXTE* monitorings also indicate short-timescale variability with a timescale of less than a few days. For example, we find a 35% decrease in the 2–10 keV count-rate between 1-Dec-2011 and 4-Dec-2011. However, we find even faster variability in the first of the *Suzaku* pointings. The sudden increase of flux (on a timescale of 12 hours) starts in the hard band and propagates into the soft-band. Let us examine the classical timescales characterizing the accretion disk. For a black hole mass of $\sim 6 \times 10^7\,\mathrm{M}_\odot$ the dynamical timescale is $t_{\rm dyn} \sim \Omega^{-1} \sim r^{3/2}/(G\,M)^{1/2} \sim 2.6\,\mathrm{hrs}$ at $10\,R_g$. Changes in the local structure of the accretion disk are governed by the thermal timescale which is $t_{\rm th} \sim t_{\rm dyn}/\alpha \sim 1\,\mathrm{day}$ at $10\,R_g$ if we assume a disk viscosity parameter of $\alpha = 0.1$. Accretion rate changes occur on the viscous timescale, $t_{\rm visc} \sim t_{\rm dyn}/[\alpha(h/R)^2]$ where h is the disk thickness. If the radiatively-efficient part of the disk really truncates at $R > 20R_g$ during this pointing, as suggested by our preferred spectral fit, the flow at $10R_g$ would be a hot, advection-dominated, geometrically-thick structure ($h \sim R$) implying that $t_{\rm visc} \sim t_{\rm th} \sim 1\,\mathrm{day}$. In the light of these timescales, we can see that the short timescale *Suzaku* event must have originated from the advection dominated flow close to the black hole (within $10R_g$). Furthermore, given that the onset of the event in a given band is very rapid ($< 6\,\mathrm{hours}$), it seems unlikely that the event is driven by changes in accretion rate (viscous timescale) or local disk structure (thermal timescale).

As already alluded to in §3.5, the *Suzaku* event may be revealing a short-term connection between the accretion disk and the jet. We will discuss this in the context of our preferred jet+disk spectral model. The *Suzaku* event starts as a jump in the hard (4–10 keV) band that, in our spectral model, is associated with X-ray emission from the disk corona. Over the next 0.5 day, it then propagates to the soft (0.7–2 keV) band that, in our model, has a significant jet component. If this is the correct interpretation, it gives us a rare look at the short timescale coupling between the disk and the jet. This coupling is almost certainly magnetic in nature (Blandford & Znajek, 1977; Blandford & Payne, 1982), and introduces a new timescale into the system — the magnetic timescale. The magnetic timescale is the timescale on which the poloidal magnetic fields in the disk can spontaneously align in portions of the disk, potentially changing the dissipation in the disk and its coupling to the jet. This magnetic timescale is hard to estimate (ultimately relating to the dynamo problem) but could be very fast (Livio, Pringle & King, 2003; King et al., 2004), especially in geometrically-thick flows expected within $R_{\rm in}$.

3.7 Summary

In this chapter, we present a detailed spectral analysis of deep *XMM-Newton* and *Suzaku* pointings of the BLRG 3C120. These observations are placed into the context of the hypothesized jet-cycle through the use of *RXTE*, *Swift* and VLBA monitoring campaigns. Our main findings are:

1. Using the monitoring data and the jet-cycle picture, we expect that the 2003-

XMM-Newton spectrum (taken at a time of peak X-ray flux) should show a complete accretion disk extending down to the ISCO, whereas the 2012-*Suzaku* observations should show truncated, refilling accretion disks.

2. A multi-epoch analysis of the *XMM-Newton* and *Suzaku* pointings finds three statistically acceptable spectral models, a disk-reflection model, a jet-model, and a jet+disk model. While they cannot be distinguished on purely statistical grounds, the disk-reflection model strongly violates the radio constraints on the jet/inner-disk inclination and cannot explain the observed UV-soft X-ray flux correlation. At the same time the jet-model suffers a severe fine-tuning problem. On the other hand, the jet+disk model appears physically reasonable in all respects.

3. Adopting this jet+disk model as our preferred solution, we do indeed find truncated disks during the two *Suzaku* pointings and a complete accretion disk at the time of the *XMM-Newton* observation. This is exactly in line with expectations from the jet-cycle picture. The ejection of a new superluminal knot about two months after an X-ray flux dip further supports this scenario.

4. We detect a rapid event in our first *Suzaku* pointing that starts in the hard band (4–10 keV) and propagates to the soft spectrum (0.7–2 keV). We interpret this as a disturbance which propagates from the inner (advective) disk into the jet on a timescale of $6 - 12$ hours, and suggest that this timescale is set by the dynamics of the magnetic field.

5. Our preferred spectral solution has a rapid black hole spin. Formally, our spectral fit yields a spin limit of $a > 0.991$. However, for such rapid spins, finite disk thickness effects must be important and will weaken the limit. Employing the toy-model of Reynolds & Fabian (2008) to assess the role of these effects suggests a true limit $a \gtrsim 0.95$.

Chapter 4: X-ray dips in the Seyfert Galaxy Fairall 9: Compton-thick "comets" or a failed radio galaxy?

4.1 AGN Variability

The previous chapters illustrate how X-ray spectroscopy is an effective tool to probe the accretion physics close to black holes. However, studies of X-ray spectral variability can be a particularly powerful diagnostic. For example, combined spectral and timing analyses have led to the discovery of distinct hardness/flux states in X-ray binaries (Tanaka & Shibazaki, 1996) which almost certainly correspond to distinct accretion modes. Spectral variability also facilitates the decomposition of a complex spectrum into physical components that would be degenerate in a single spectrum.

Detailed studies of long term (year+) X-ray variability in AGN have been possible since the launch of *RXTE* but a relatively small number of sources have been targeted for detailed study (Markowitz et al., 2003; Rivers, Markowitz & Rothschild, 2011). These studies are crucially important as they probe timescales comparable to the viscous timescale on which the true mass accretion rate would be expected to vary. More typical X-ray observations of AGN probe timescales of hours-to-days, characteristic of dynamical or thermal timescales but much shorter than the viscous timescales. Long-term studies are also important for uncovering rare/transient phenomena that may give unique windows into the physics and structure of AGN.

In this chapter, we report the discovery of an unusual pattern of X-ray variability in Fairall 9, which we already studied in Chapter 2, using the long-term monitoring data from pointed *RXTE* observations. Rather than displaying the usual "flary" lightcurve with a log-normal flux distribution (Gaskell & Klimek, 2003; Uttley, McHardy & Vaughan, 2005), Fairall 9 shows long-timescale modulations punctuated by strong and sudden *dips*. This behavior was apparent but not commented upon when the monitoring was first presented by Markowitz et al. (2003). Using the latest background models and calibration files, we analyze all available *RXTE* data and confirm the presence of these dips in the *RXTE* lightcurve. We discuss their possible origins, including the possibility that they correspond to eclipses of the X-ray source by clouds in the BLR. Alternatively, the dips may result from a genuine accretion disk instability, suggesting an interesting parallel between Fairall 9 and broad line radio galaxies.

4.2 Observations

The observations considered in this analysis are all those of Fairall 9 with public *RXTE*/PCA data, a total of 744 pointings spanning the period from late 1996 until early 2003. This gives an average time resolution of about 4 days with an average pointing length of 1.1 ks. Only data from the top layer of proportional

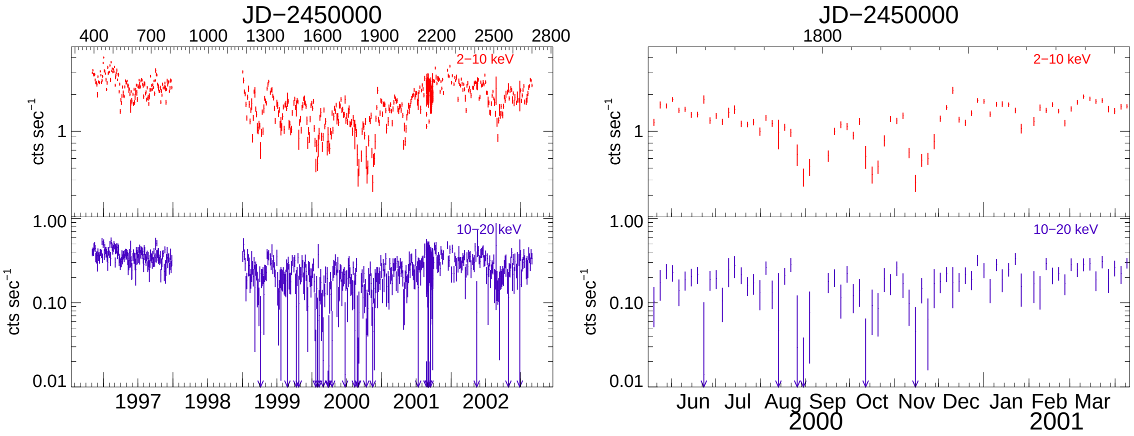

Figure 4.1: *Left :* Long term *RXTE*-PCA lightcurves for 2–10 keV (top panel) and 10–20 keV (lower panel). *Right :* Zoom-in on the *RXTE*-PCA lightcurves for mid 2000 until 2001 April.

counter unit 2 were used. The data were reduced as outlined in Wilms et al. (2006), using HEASOFT 6.10. For each pointing, we produce a background-subtracted PCA spectrum using the appropriate epoch-dependent background/response files. The count rates quoted below were obtained from the spectra for each pointing. We do not consider any intra-pointing variability in this work.

4.3 Results

4.3.1 Lightcurves and confirmation of dipping

The long-term lightcurve in the 2-10 keV and 10-20 keV band is plotted in Figure 4.1 (left). This lightcurve displays the unusual behavior already noted in the introduction; long timescale flux modulations punctuated by short and intense dips. These dips consist of a rapid flux decline by a factor of 2–4 in 5–10 days and then a recovery to the pre-dip level with an entire dip-duration of 10–20 days (Fig. 4.1

right). The existence of these dips introduces a low-flux tail to the flux distribution, skewing it strongly away from log-normal (Fig. 4.2). To the best of our knowledge, these unusual dips in Fairall 9 have not been commented upon previously.

On longer timescales the source is experiencing a flux decline from early 1999 reaching its low in the fall of 2000 and then recovering to a higher flux value towards the middle of 2001. There is clearly a greater propensity to dip during the lower-flux state. The average flux in 2–10 keV for the object is $(2.16\pm0.63)\cdot10^{-11}\,\mathrm{ergs\,s^{-1}\,cm^{-2}}$. Both the long term and short term variability seem to be of similar nature in the two different bands. In particular, while the dips are most clearly seen in the 2–10 keV lightcurve due to the higher signal-to-noise, they are also present in the 10–20 keV lightcurve.

4.3.2 Spectral Evolution

To further explore the nature of the variability, we perform flux resolved spectroscopy. We choose to use the 2–5 keV flux as our flux discriminator since this will be dominated by the primary power-law rather than a soft excess component or reflection. We define a "high state" as $F_{2-5\,\mathrm{keV}} > 1\times10^{-11}\,\mathrm{ergs\,s^{-1}\,cm^{-2}}$ and, by summing the data for all pointing which exceed this flux, form a "high state spectrum". Similarly, we define a "low state spectrum" ($F_{2-5\,\mathrm{keV}} = (0.5-1.0)\times10^{-11}\,\mathrm{ergs\,s^{-1}\,cm^{-2}}$). A flux of $10^{-11}\,\mathrm{ergs\,s^{-1}\,cm^{-2}}$ in 2–5 keV corresponds to a 2–10 keV count rate of about 1.45 counts per second. A "dip state spectrum", with a dip defined as a count rate drop of a factor of 1.5 in 2–10 keV, with respect to the

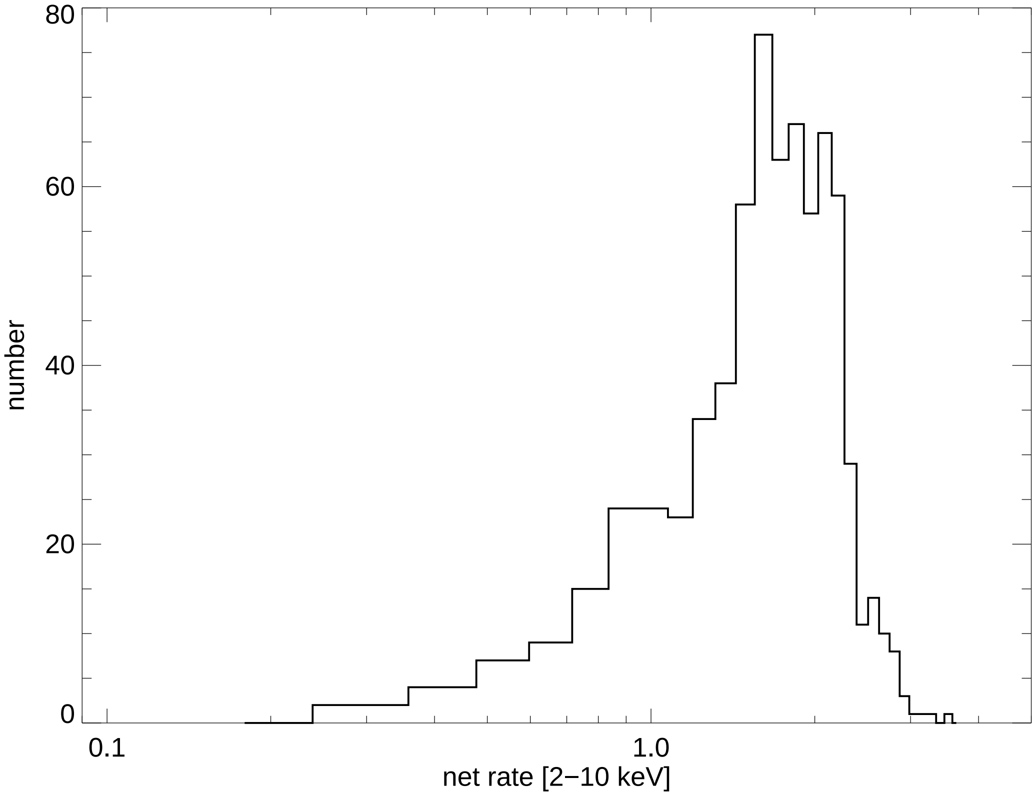

Figure 4.2: Histogram of 2–10 keV count rate

rate right before the dip and the two pointings following the drop, is also defined. The pointings considered to be part of a dip were excluded from high and low states.

Previous studies have shown that, to first order, the spectrum can be well described by a continuum, originating from a comptonizing corona, and cold reflection. We model this scenario using the `pexmon` model (Nandra et al., 2007), which consists of a power law continuum plus the cold reflection continuum and associated iron Kα/Kβ fluorescent lines (with a self-consistent strength). The quality of the data does not allow constraints on all parameters in the model, therefore the abundances are assumed to be solar and the inclination of the reflector is fixed to 60 degrees (the most probable value, assuming a random orientation). We also include cold Galactic absorption with a column density $N_{\mathrm{H}} = 3.1 \times 10^{20}\,\mathrm{cm}^{-2}$, modeled by `TBnew`[1] a newer version of `TBabs` (Wilms, Allen & McCray, 2000) with cross sections set to `vern` and abundances set to `wilm`. The reflection fraction R is left free to vary.

Table 4.1 shows the spectral fitting results for these three flux-sorted spectra. The spectra are well described by the model, see Fig. 4.3, except for the high state spectrum where a residual line in the iron K region remains. This feature can be modeled with an additional iron line at the redshift of Fairall 9, with an equivalent width of $35 \pm 8\,\mathrm{eV}$. The uncertainties in the energy of this additional line span both neutral and H-like iron. Beyond that required by the reflection component, an additional line with this strength is rejected by both the low-state and dip-state spectra. Thus, it appears that the additional iron line component is exclusively displayed by the high state spectrum. We comment on the nature of this spectral feature in Section 4.4.

In agreement with previous studies of Seyfert galaxies (e.g., see Chiang et al., 2000), the continuum softens (Γ increases) from the low- to the high-state (Fig. 4.4). We also see a reflection fraction which is inversely proportional to the continuum flux; i.e., the X-ray reflection is consistent with being a constant flux contribution. The most obvious interpretation is that a significant component of the reflection is from a distant structure. Given that the modulation betwen high- and low-flux states occurs on timescales of $\sim 1\,\mathrm{year}$, we infer that the distant reflector is situated at least a light year from the central X-ray source. We note that X-ray

---

[1] http://pulsar.sternwarte.uni-erlangen.de/wilms/research/tbabs/

reflection from the inner accretion disk is also expected to be present (Schmoll et al., 2009; Emmanoulopoulos et al., 2011, Chapter 2) and, given the error bars on R, its presence is consistent with these data.

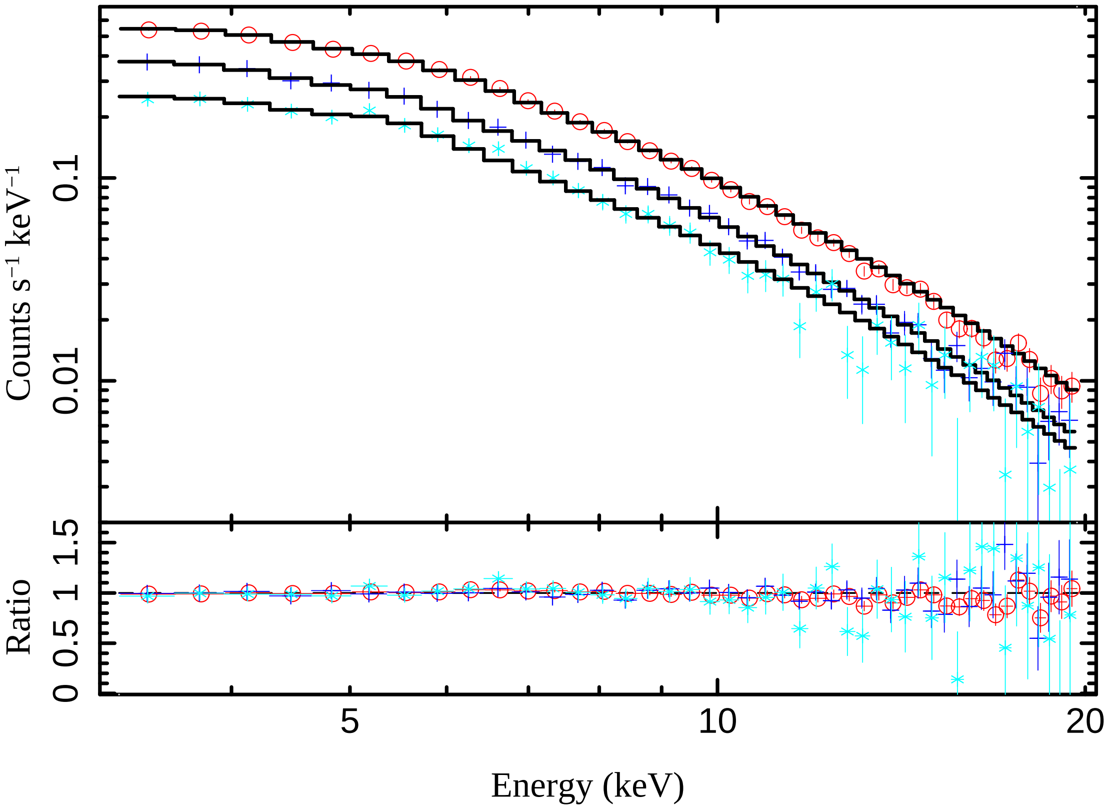

Figure 4.3: Spectra (high state [dots], low state [crosses], dip state [stars]), model [solid line] and residuals for the PCA summed flux resolved spectra for the fit with the cold reflection model.

Although flux resolved spectroscopy is a powerful tool, it does not offer the possibility to study the actual spectral evolution in time. Higher time resolution can be achieved by looking at X-ray flux-flux plots in different bands. Figure 4.4 shows the 2–5 keV/5–10 keV flux-flux plot; a positive correlation is apparent, although it is clearly non-linear as can be seen by a comparison with a spectral variability

Table 4.1: Spectral Parameters for cold reflection fits, see text for details on the model set-up.

Flux State	Γ	R	Flux [2–10 keV]	χ^2/dof
high	$2.00^{+0.03}_{-0.03}$	$1.3^{+0.2}_{-0.2}$	$2.7 \cdot 10^{-11}$	73.3/42
high w line	$1.90^{+0.03}_{-0.03}$	$0.5^{+0.2}_{-0.2}$	$2.7 \cdot 10^{-11}$	16.5/41
low	$1.91^{+0.04}_{-0.04}$	$1.1^{+0.3}_{-0.2}$	$1.8 \cdot 10^{-11}$	38.9/42
dip	$1.98^{+0.14}_{-0.13}$	$2.1^{+1.3}_{-1.0}$	$1.2 \cdot 10^{-11}$	32.0/42

model possessing a flux variable power law with a constant hard component (i.e. constant cold reflection). At high fluxes, the non-linearity appears dominated by a genuine softening of the primary continuum. This was already seen in earlier studies for Fairall 9 and other Seyfert 1 galaxies (Markowitz & Edelson, 2001; Sobolewska & Papadakis, 2009). At the lowest fluxes (corresponding to the dip state) there is a change in the nature of this non-linearity, with the lowest few 2–5 keV flux points having an almost constant 5–10 keV flux. This signals a significant spectral hardening during the deepest parts of the (2–5 keV) dips. However, the spectrum is never dominated by reflection.

We do note that this non-linearity calls into question the use of y-intercepts in extrapolated flux-flux diagrams to determine constant components in AGN spectra (e.g., see Noda et al., 2011).

4.4 Discussion and Conclusion

In this chapter, we studied the X-ray variability of Fairall 9 on timescales of a few days to five years. On the long timescales studied by the flux resolved spec-

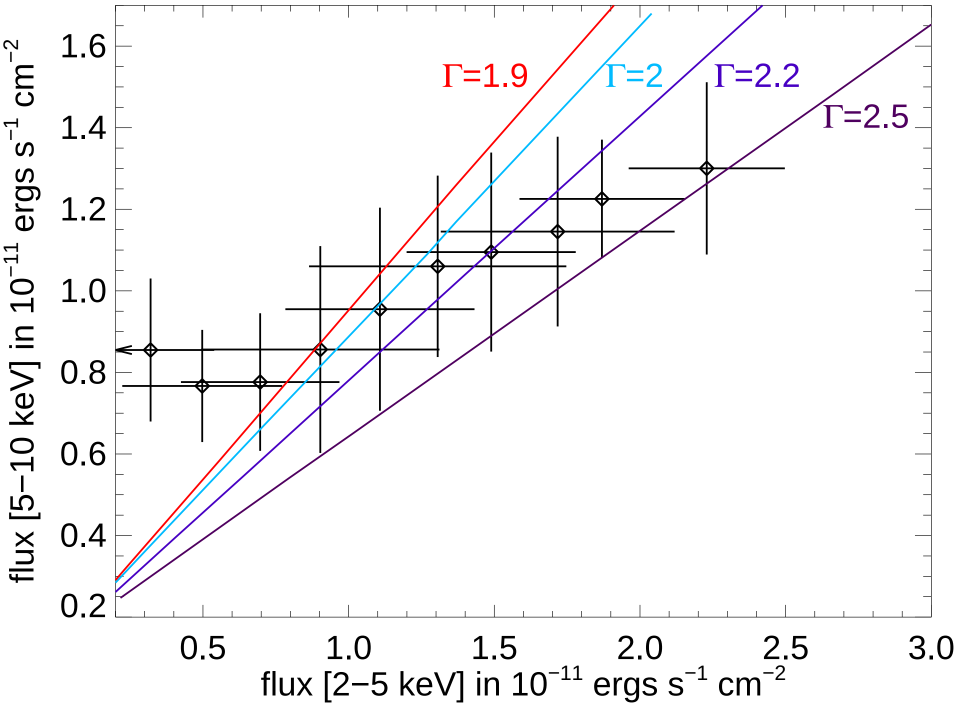

Figure 4.4: Flux-flux plot for the 2–5 keV and the 5–10 keV band binned for plotting, showing the non-linearity of the flux-flux relation, as well as model lines for a constant hard component with a flux-variable power law for a set of photon indexes.

troscopy, a significant fraction of the reflected X-rays appear to maintain a constant normalization, suggesting that potentially a significant fraction of the X-ray reflection might originate from a structure at least a light year across. The excess iron emission line (above and beyond that associated with the reflected component) in the high-state spectrum suggests that, in this state, there might be an appreciable increase in the amount of Compton-thin material intercepting the primary X-ray continuum. This material must be out of our line of sight since we see no iron absorption edge in the high-state spectrum. A possible identification for these feature is iron line emission (fluorescence or radiative recombination) from a radiatively-driven disk wind that forms in the high-flux state. The spectral resolution of the PCA prevents us from constraining the charge state of the additional iron line and hence the ionization state of this additional material.

The most unusual finding is the discovery of strong and sudden dips in the observed X-ray flux from Fairall 9. In the rest of this section, we discuss the nature of these dips. There are two fundamentally different interpretations; transient absorption events (i.e. eclipses) of the inner accretion disk, or a genuine turning-off of X-ray emission from the inner disk.

We begin by addressing the absorption possibility. At least upon the immediate onset of a dip, both the 2–10 keV and 10–20 keV fluxes drop by similar magnitudes requiring that the absorber be Compton-thick ($N_H > \mathrm{few} \times 10^{24}\,\mathrm{cm}^{-2}$). Suppose that the radius of an absorbing "cloud" has radius $r = xR_{\rm g}$ (as defined in Chapter 1) and it is situated $R = X\,R_g$ from the black hole. Assuming Keplerian motion, the velocity of the cloud is $v = X^{-1/2}c$ and hence the eclipse of the inner disk by the cloud with a duration $\Delta t \sim 2r/v = 2xX^{1/2}(R_{\rm g}/c)$. For a black hole mass of $M \approx 3 \times 10^8\,M_\odot$ (Peterson et al., 2004), this gives $\Delta t \sim 3000xX^{1/2}$ s. The observed 2–10 keV dips have a duration $\Delta t \approx 2 \times 10^6$ s, implying that $xX^{1/2} \approx 700$. Assuming that the X-ray source has a size of $r_X = 1\,0R_{\rm g}$, we must have $x \gtrsim 10$ ($r \gtrsim 5 \times 10^{14}$ cm) in order for the cloud to be able to block the source and create a strong dip, implying $X \lesssim 5000$ and $v \gtrsim 4300\,\mathrm{km\,s^{-1}}$. Thus, the absorbing clouds are consistent with being at BLR distances. For a cloud with radius $r \sim 10^{15}$ cm to be Compton-thick, it must have a density exceeding $n \sim \mathrm{few} \times 10^9\,\mathrm{cm}^{-3}$. Thus, these absorbing clouds also have a density consistent with that of BLR clouds (e.g., see Korista & Goad, 2000)

X-ray eclipses by putative BLR clouds have been found recently in some other AGN, notably NGC 1365 (Maiolino et al., 2010) and Mrk 766 (Risaliti et al., 2011). There are some important differences between the Fairall 9 events and the events in these other sources. Firstly, in NGC 1365, even the non-eclipse spectrum shows significant absorption. By contrast, the non-dip state of Fairall 9 is notable for being so clean, having *no* discernible cold or ionized absorption seen in any of its previous *ASCA* (Reynolds, 1997), *XMM-Newton* (Gondoin et al., 2001; Emmanoulopoulos et al., 2011) or *Suzaku* (Schmoll et al., 2009) observations. Secondly, the eclipsing clouds in NGC 1365 and Mrk 766 are generally Compton-thin with strong evidence that the column density spikes up and then steadily decreases during the event. This led to the notion of BLR "comets" (Maiolino et al., 2010) with high column density heads followed by lower column tails. By contrast, the Fairall 9 clouds must be Compton-thick, at least at the beginning of the dip event. However, a "comet" scenario would predict a Compton-thick to Compton-thin transition, leading to a recovery of the hard band lightcurve before the soft band dip ends. The signal to noise of the current data is insufficient to detect such an early hard-band recovery. Future studies with *Suzaku*, *NuSTAR* or *Astro-H* are required to test these predictions.

The presence of well-defined Compton-thick clouds in an otherwise extremely clean environment raises questions about cloud confinement and, more generally, the nature of these clouds (Kallman & Mushotzky, 1985; Snedden & Gaskell, 2007).

A detailed discussion of the physics of such clouds is beyond the scope of this chapter. We do however note that the properties of these clouds (Compton-thick and $r \sim 10^{15}\,\mathrm{cm}$) are consistent with the irradiated envelopes of circumnuclear stars (i.e., "bloated stars", Edwards, 1980; Penston, 1988). Bloated stars have been ruled out as a viable model for the broad emission lines themselves on the basis of the smoothness of the Hα profile (Arav, Laor, & Blandford, 1997; Laor et al., 2006). However, especially in high-mass systems such as Fairall 9, bloated stars may nevertheless be present and could readily eclipse the X-ray source producing dips.

Could the dips be intrinsic to the accretion process, i.e., signal a genuine "turning-off" of X-ray emission from the inner accretion disk? It will be useful to delineate a few characteristic timescales for the inner regions of this AGN. The light crossing time of the inner X-ray emitting regions of the accretion disk (say, out to $r = 10\,R_{\rm g}$) is $t_{\rm lc} \approx 30\,\mathrm{ks}$, and the dynamical timescale of the disk at $r = 10\,R_{\rm g}$ is $t_{\rm dyn} \approx 50\,\mathrm{ks}$. Assuming an angular momentum transport parameter $\alpha \approx 0.1$, the thermal timescale at this radius is $t_{\rm th} = t_{\rm dyn}/\alpha \approx 500\,\mathrm{ks}$. Finally, we consider the viscous timescale, $t_{\rm visc} = t_{\rm th}/(h/r)^2$ where h is the geometric thickness of the accretion disk. With an average 2–10 keV flux of $2.2 \times 10^{-11}\mathrm{ergs/s/cm^2}$ and using a bolometric correction of 50 from Marconi et al. (2004), we find an Eddington ratio of $\mathcal{L} \approx 0.15$ for Fairall 9. For such an Eddington ratio (and assuming a radiative efficiency of $\eta = 0.1$), standard accretion disk theory (Shakura & Sunyaev, 1973), the inner disk is radiation pressure dominated and has a geometric thickness $h = (3\mathcal{L}/2\eta)R_{\rm g} \approx 2.3\,R_{\rm g}$. Thus, at $r = 10\,R_{\rm g}$, we have $h/r = 0.23$ and a viscous timescale of $t_{\rm visc} \approx 9.4\,\mathrm{Ms}$ (i.e., approximately 110 days).

The most obvious (albeit dramatic) scenario is one in which the innermost parts of the radiatively-efficient optically-thick accretion disk are destroyed/ejected by a dynamical or thermal instability. This is hypothesized to occur in radio-loud BLRGs as part of the process of jet formation (Marscher et al., 2002; Chatterjee et al., 2009; King et al., 2011, Chapter 3). In the BLRGs, a distinct dip in the X-ray flux precedes large radio flares and the creation of a new superluminal knot. Since, as with Seyferts, the X-ray emission in BLRGs is also dominated by the corona of the inner accretion disk (Marshall et al., 2009), this X-ray/radio connection conclusively demonstrates a link between changes in the inner accretion disk structure and powerful jet ejection events. In fact, it is instructive to directly compare Fairall 9 with the BLRG 3C120. 3C120 has a slightly lower-mass black hole, $6 \times 10^7\,M_\odot$ for 3C120 compared to $3 \times 10^8\,M_\odot$ for Fairall 9 (Peterson et al., 2004). However, they possess a very similar Eddington ratio, $\mathcal{L}_{\rm F9} \approx 0.15$ compared to $\mathcal{L}_{\rm 3C120} \approx 0.11$, derived using the bolometric luminosity for 3C120 from Vasudevan & Fabian (2009). Thus, their accretion disks might be expected to be in rather similar regimes of behavior. It is possible that the X-ray dips seen in Fairall 9 have the same physical origin as the ejection-related X-ray dips seen in 3C120 but, for some reason, these disk disruption events lead to the creation of powerful jet outflows in 3C120 but not in Fairall 9 (indeed, Fairall 9 has yet to be detected in the radio band, with an upper limit of $< 36\,\mathrm{mJy}$ at 1.4 GHz, see Whittle, 1992). Either the magnitude/direction of the black hole spin or the magnetic field structure in the inner disk may be the determining factor in deciding whether disk disruptions generate relativistic outflows. For Fairall 9, the black hole spin has already been measured and was found to be moderate (Schmoll et al., 2009, Chapter 2). Observations of Galactic black hole X-ray binaries support this idea of viewing the dips in the context of jet ejections, as some were observed to possess very faint jets, undetectable in case of an AGN (Gallo et al., 2005; Gallo, 2007).

Chapter 5: The fast UV variability of the active galactic nucleus in Fairall 9

5.1 Introduction

After investigating the X-ray variability in the last chapter, this chapter is dedicated to studying the joint UV and X-ray variability of Fairall 9.

It is widely accepted that the optical/UV continuum from radio-quiet AGN is thermal (quasi-blackbody) emission from the radiatively-efficient, optically-thick supermassive black hole accretion disk. Hence, the spectrum and variability of the optical/UV emission gives us a direct window on the accretion process. Prior to the launch of *Swift* and *XMM-Newton*, most studies of the UV variability were performed as part of reverberation mapping campaigns. For example, in the 1990s, the International AGN Watch Consortium (IAWC) used ground-based optical spectroscopy, as well as UV, EUV and X-ray data from a number of space-based observatories, to monitor several Seyfert galaxies including the subject of this chapter, Fairall 9 ($z = 0.047$). In a series of works (e.g. Rodriguez-Pascual et al., 1997; Marshall et al., 1997; O'Brien & Leighly, 1998, and references therein) the IAWC showed that the optical/UV emissions in these sources were often variable down to the sampling timescale. Furthermore, they showed that the optical and UV (and sometimes but not always the X-ray) were highly correlated with no detectable time-lag. Since this implies that emission across an extended region of the disk must be correlated on essentially the light-crossing time, this drove one to a picture whereby the optical/UV emission is reprocessed energy originating from the central-most parts of the accretion disk.

These results were confirmed by later monitoring campaigns based on X-ray monitoring by the *RXTE* satellite and a ground based optical monitoring. For example, Breedt et al. (2009) studied a five year monitoring of Mrk 79 determining that the optical and X-ray are correlated without any lag. In NGC 3516 on the other hand, the results were less conclusive, as X-ray absorption does not give us direct view of the central engine during most of the time (Maoz et al., 2002). A two year monitoring of NGC 3783 by Arévalo et al. (2009) revealed no or a very small lag between the B and V bands, confirming the idea that the UV and optical are originating from adjacent parts of the accretion disk. Between the X-ray band and the UV/optical a 3-9 day lag consistent with the UV being reprocessed emission was detected.

The launches of *Swift* and *XMM*, with their optical/UV telescopes mounted co-axially to their pointed X-ray instruments have also provided powerful new opportunities to study the optical/UV/X-ray variability of AGN. Both UV telescopes (the *Swift* UV-Optical Telescope [UVOT] and the *XMM* Optical Monitor [OM]) have significantly better spatial resolution than IUE, and both observatories automatically provide simultaneous X-ray observations. These instruments provide advantages over ground-based studies even for optical photometry as they are space-based and hence complications such as airmass can be avoided. While *XMM* provides the better X-ray spectrum due to its large effective area in the X-ray band, *Swift* is much more suited for monitoring campaigns because of its shorter slew time and autonomous operation. To a large extent, these studies have confirmed the results of IAWC. For example, Cameron et al. (2012) have presented *Swift* monitoring of the low-mass AGN NGC 4395 and find correlated variability from the optical through into the X-ray. No optical-UV lag is detected, and a very small (400 s) lag between the X-ray and UV is reported.

To date, most of the objects studied with this new generation of observatories are blazars (which are completely jet dominated and hence not useful for accretion disk studies), or highly variable objects such as narrow-line Seyfert-1 galaxies (Alston, Vaughan & Uttley, 2013; Gliozzi et al., 2013; Grupe et al., 2013). Narrow-line Seyfert-1 galaxies are peculiar objects known to possess large soft excesses and mostly accrete at high Eddington rates. Some results have also been reported for "normal" Seyfert galaxies, using these type of instruments.

The goal of this chapter is to shed more light on the UV/optical variability and its relation to the X-ray variability in one of those average Seyfert-like AGN – Fairall 9. The data used in this analysis are a 2.5-month *Swift* monitoring and an archival *XMM* dataset. Given that this AGN hosts a rather massive black hole, $M = (2.55 \pm 0.56) \times 10^8 M_\odot$ (Peterson et al., 2004), we are able to probe timescales down to almost the light crossing time of the black hole. It is not only its high black hole mass that makes Fairall 9 a suitable study target, but it is also unobstructed by any line-of-sight absorption such as warm absorbers (e.g. Emmanoulopoulos et al., 2011, Chapter 2). This lack of line-of-sight absorption offers the possibility to study the continuum and its variability in great detail and excludes absorption as the driver of the variability in this object as it has been previously suggested in some cases (e.g., Grupe et al., 2013).

We discover UV variability on 4 day timescales, the light crossing time of the UV emitting region; we argue that this is strong confirmation that a significant component of the UV is reprocessing of (largely unseen) EUV emission from the central parts of the accretion disk. The *XMM* dataset allows us to study the UV and X-ray variability on the timescales of a few hours. We calculate the Edelson & Krolik discrete correlation function and find two marginally significant correlations. One is a correlation were the UV lags the X-rays by about 1-2 hours. The second is an anti-correlation where again the UV lags the X-rays, this time by about 5 hrs. The 1-2 hrs lag can be explained by reprocessing of the X-ray emission of small, short duration X-ray flares in the accretion disk. The anti-correlation however is hard to explain and will require further investigation.

The outline of this chapter is as follows. First, we describe the datasets used in this work and briefly discuss data reduction techniques (§5.2). After an investigation of the optical/UV variability (§5.3.1), we analyze the UV–X-ray variability (§5.3.2). We end with a discussion of the implications of these results (§5.4).

5.2 Data Reduction

5.2.1 Basic *Swift* data reduction

The *Swift* data presented here are from a 2.5 month campaign from 16-April-2013 to 1-July-2013 designed to search for and further study the X-ray dips first reported in Chapter 4. The XRT data were taken in windowed timing mode and uniformly reduced and analyzed as described in Chapter 3.

UVOT was operated in imaging mode and, for most of the pointings, cycled through all six filters; V, B, U, UW1, UM2, and UW2. The UVOT analysis begins with summing the individual exposures per observation for each individual UVOT filter using the tool `uvotimsum`. The `uvotsource` tool was then used to extract fluxes from the images using aperture photometry, it also corrects for coincidence losses. The source region was selected to be circular with a 5.0 arcsec radius around the coordinates obtained from the NASA Extragalactic Database (NED) —RA 01h23m45.8s, DEC −58d48m20.8s (J2000). For the background extraction, a source-free circular region with 32 arcsec radius close to Fairall 9 was selected.

5.2.2 Basic *XMM* data reduction

The archival *XMM-Newton* dataset considered here was taken 10-December-2009 (ObsID:0605800401). The X-ray data were reduced as described in Chapter 2. We only consider EPIC-pn data for the analysis performed in this chapter, as MOS does not contribute much additional information for this work. The total good on-source exposure is 91 ks. From this, we extract a lightcurve binned to a time resolution of 1 ks. The *XMM*-OM was operated with a single UV-filter (UVW1), and the data were reduced using the `omipipeline`. The resulting count rates where then converted into fluxes as outlined in the XMMSAS User's Guide [1].

5.2.3 Differential Photometry

To enhance the accuracy of the UV/optical photometry and verify the photometric stability during the 2.5 months of monitoring, we perform differential photometry with respect to reference stars in the vicinity of Fairall 9. We consider a total of 6 stars, which were selected from the USNO-A2 guide star catalog. A list of those stars is given in Table 5.1.

Table 5.1: Reference stars selected to monitor the detector variability of *Swift*-UVOT

Source #	USNO A02 identifier	Ra	Dec	Distance [arcmin]
1	0300-00420304	20.944	-58.795	0.62
2	0300-00421798	21.007	-58.829	2.51
3	0300-00422565	21.038	-58.730	5.46
4	0300-00419203	20.894	-58.889	5.20
5	0300-00423563	21.081	-58.732	6.23
6	0300-00419618	20.913	-58.910	6.33

These stars are detectable in every single frame image in all the filters for the UVOT instrument. We then proceed to obtain the fluxes in all filters of all these stars, in case of UVOT, and in case of OM of stars # 1, 2 and 4. For UVOT

---

[1] http://xmm.esac.esa.int/external/xmm_user_support/documentation/sas_usg/USG/ommag.html

this is done by again using a 5 arcsec source radius and making use of the tool `uvotsource`. For OM the photometry results from `omdetect` can be used directly. The stars' average observed B-V color is 0.01, which is somewhat bluer than that of Fairall 9 (0.13) and most likely arises from the requirement of a detection also in the bluer optical bands. Assuming the stars do not vary on the relevant timescales, the attained individual flux values are re-normalized and averaged for each observation. An example of the resulting reference star lightcurves and its average can be seen in Figure 5.1 for the UVOT U-Band. These re-normalized, averaged values now represent the variability due to the detector or other observation related differences. To correct our Fairall 9 flux values by this variability and get the true variability, we divide by the variability seen in the reference stars.

5.2.4 Host Galaxy Subtraction

The detector-variability corrected UV fluxes are corrected for reddening from our Galaxy using a reddening law by Cardelli, Clayton & Mathis (1989) with updates in the near-UV by O'Donnell (1994), assuming E(B-V)=0.03 (Schlegel, Finkbeiner & Davis, 1998). However, the measured flux is not all just nuclear/AGN emission — to obtain the optical/UV lightcurve of the AGN, this lightcurve needs to be corrected for contamination by the host galaxy. In particular, the (time-invariant) host galaxy component can offset the spectral slope and mimic a slope change which is not real. Therefore, a proper host galaxy correction is necessary if we are to study color changes and variability amplitudes in the AGN with any degree of robustness.

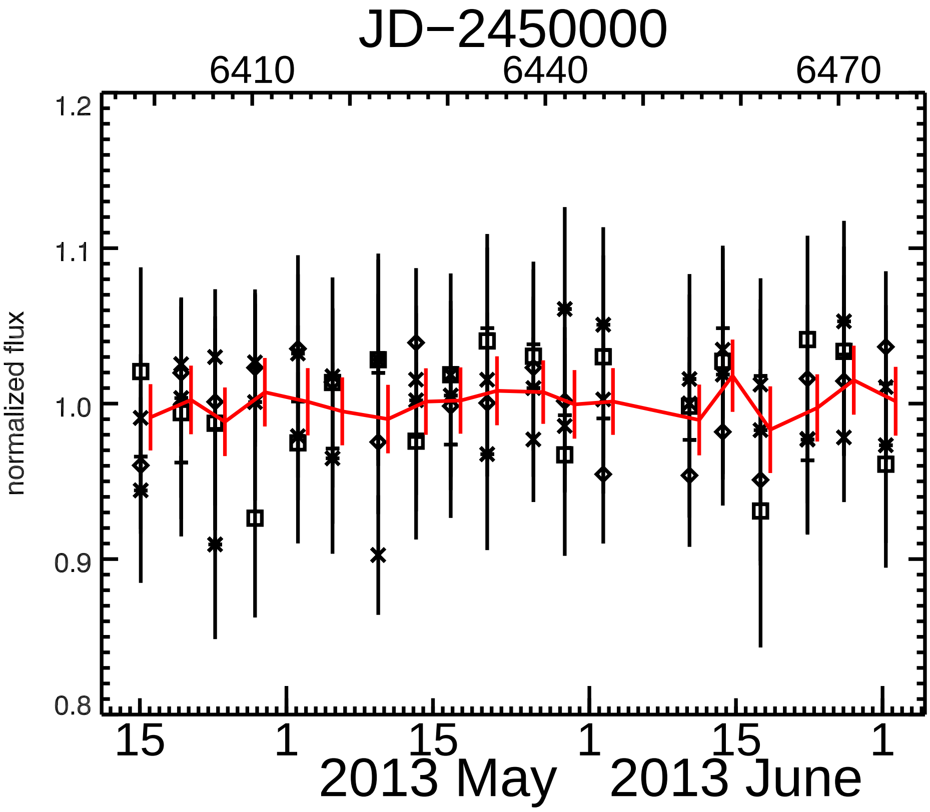

Figure 5.1: Normalized fluxes of reference stars, where each plot symbol corresponds to a different star, and their average flux in U-Band shown in red color. The average, normalized flux is offset in time in the plot for clarity.

The host galaxy contribution to the flux at optical wavelengths was studied with HST by Bentz et al. (2009) and the galaxy classified as a SBa galaxy. By performing a two-dimensional galaxy decomposition they determine the host galaxy flux of Fairall 9 at 5100 Å to be $3.47 \times 10^{-15}\,\mathrm{erg\,s^{-1}\,cm^{-2}\,\AA^{-1}}$. 52 % of this galaxy flux originated from the bulge. As the *Swift*-UVOT and *XMM*-OM have a very limited spatial resolution compared to HST, we cannot perform a detailed study of the host galaxy ourselves, but instead use the HST value to anchor SED templates which can then be used to determine the galaxy contribution to our UVOT/OM light-curves. Galaxy SED templates are preferable as they enable the host galaxy estimation at various wavelengths, while galaxy decompositions are only meaningful at the wavelength performed. The region used for the UVOT photometry is small so we assume that all of the galaxy flux in this central region comes from the bulge. We also verify that this decision, which underestimates the galaxy contribution slightly, yields qualitatively the same results for variability and color changes than overestimating the galaxy contribution by subtracting off the entire galaxy (bulge+disk). We start the galaxy subtraction by renormalizing the bulge template from Kinney et al. (1996) to the bulge flux measured with HST. The host galaxy flux contribution in a given UVOT/OM filter band $F_{\rm filter}$ can then be obtained by convolving the normalized filter function $S_{\rm norm}(\lambda)$ with the re-normalized bulge template $T_{\rm norm}(\lambda)$

$$F_{\rm filter} = \int T_{\rm norm}(\lambda)\, S_{\rm norm}(\lambda) d\lambda \tag{5.1}$$

The so-calculated galaxy fluxes are subtracted from the measured fluxes and we are able to obtain the final UV/optical lightcurves (Fig. 5.2 and Fig. 5.3 [bottom panel]). In all bands, the reddening correction dominates (and grows in importance into the UV). The host galaxy correction is modest in the B-band ($\sim 6\%$), and decreases in importance at shorter wavelengths.

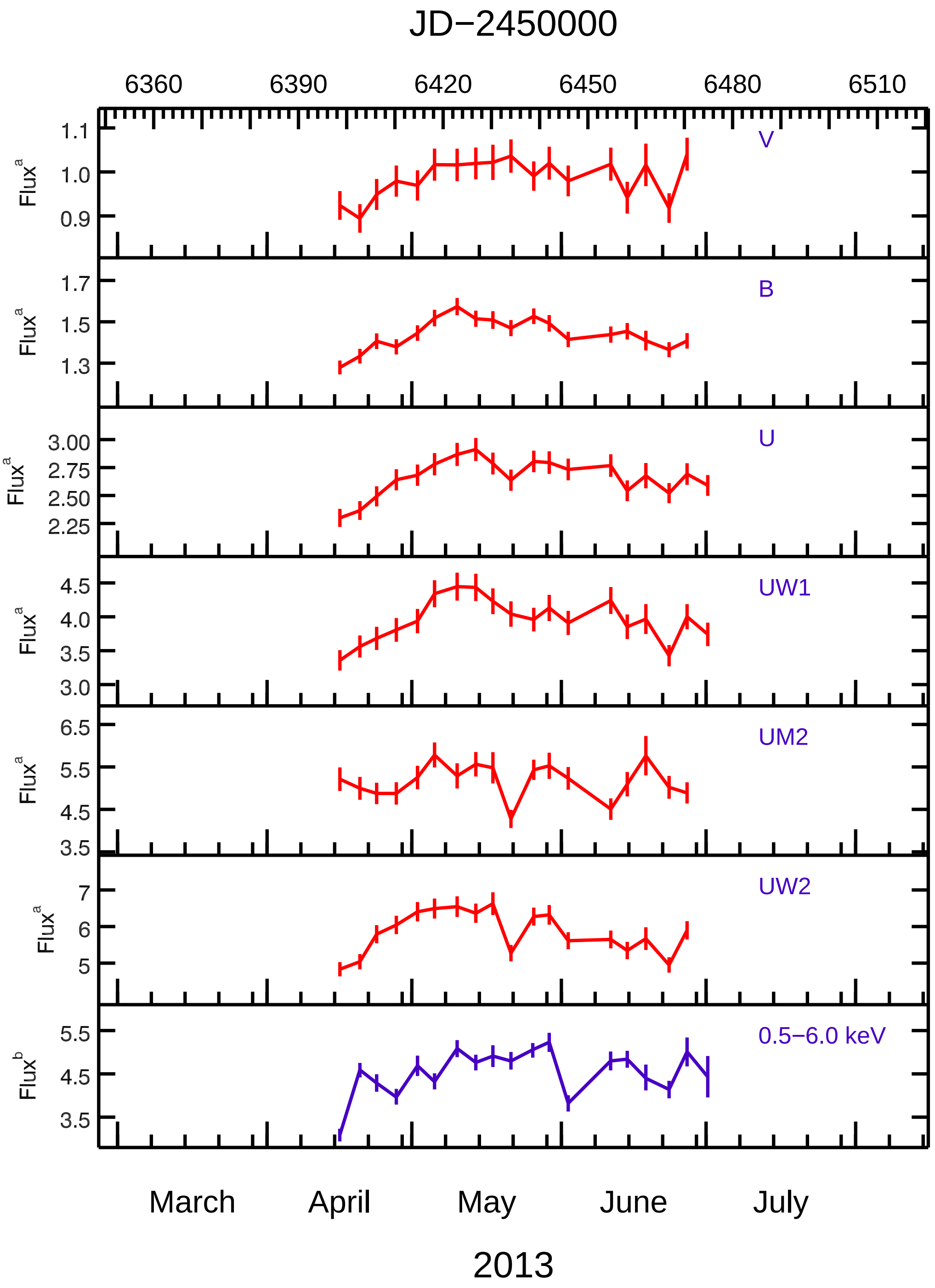

Figure 5.2: Fairall 9 *Swift* lightcurve, with an average 4-day sampling, at selected wavelengths corrected for guide star variability, as well as reddening and host galaxy contribution. [a] Flux in $10^{-14}\,\mathrm{erg\,s^{-1}\,cm^{-2}\,\AA^{-1}}$. [b] Flux in $10^{-11}\,\mathrm{erg\,s^{-1}\,cm^{-2}\,keV^{-1}}$

Table 5.2: Mean AGN fluxes, Galaxy fluxes and normalized excess variances per filter band/center filter wavelength.

Band	λ_{c}	$\bar{F}_{\mathrm{AGN}}$	F_{Gal}	σ^2_{rms}
	Å	$10^{-14}\,\mathrm{erg\,s^{-1}\,cm^{-2}\,Å^{-1}}$	$10^{-16}\,\mathrm{erg\,s^{-1}\,cm^{-2}\,Å^{-1}}$	10^{-3}
V	5468	0.959	15.9	3.6 ± 1.1
B	4392	1.39	8.93	3.9 ± 0.86
U	3465	2.56	3.10	5.3 ± 1.3
UW1	2600	3.76	0.853	8.9 ± 2.2
UM2	2246	4.82	0.460	10 ± 3.1
UW2	1928	5.49	0.601	12 ± 2.6

5.3 Results

5.3.1 Optical/UV Variability

Figure 5.2 shows the optical/UV/X-ray lightcurves from our *Swift* monitoring and indicates variability in all bands. This is verified by a χ^2-test, variability is detected in each band with at least 95 % confidence. The variability increases in amplitude towards the UV bands (Table 5.2) and is clearly correlated between the different bands. For example, we find a correlation coefficient of 0.64 (p-value: 0.004) between the V- and the UW2-band, neglecting the small delay between the observations originating from the filter rotation.

It is interesting that we detect UV variability down to the shortest timescales probed by the *Swift* campaign (4 days). Particularly noteworthy is the UV dip on 22-May-2013. During this event the UW2 (1928Å) flux drops by 20% between two pointings separated by 4-days. This dip is also seen in the UM2 filter (which

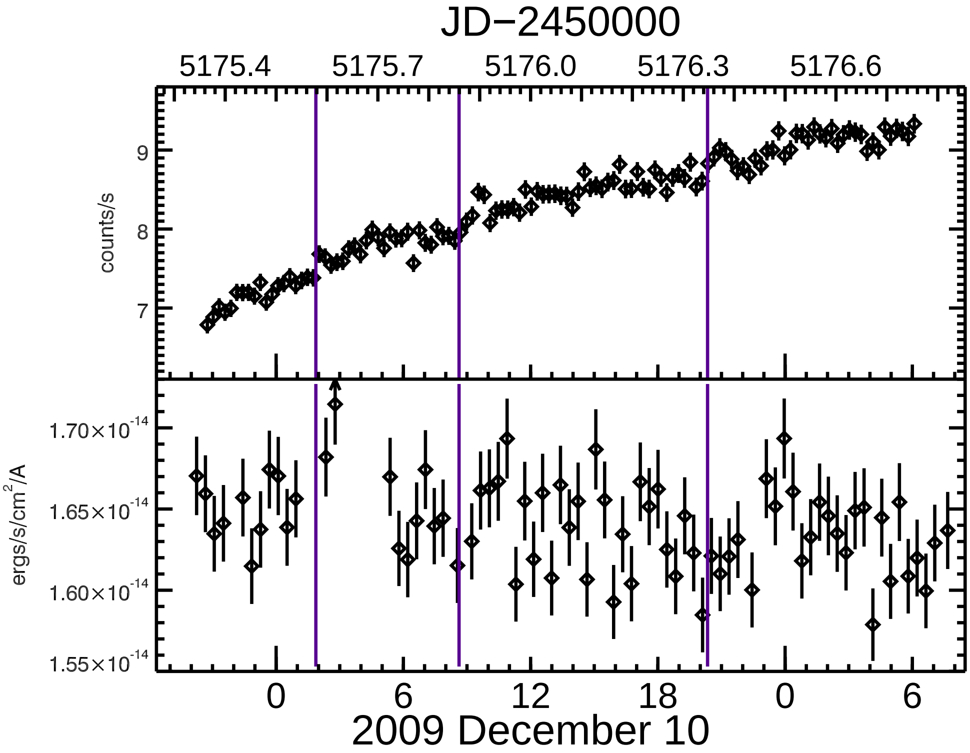

Figure 5.3: Fairall 9 *XMM* X-ray lightcurve (top panel) [0.3-2.0 keV, 1 ks resolution] and UV fluxes (bottom panel) corrected for guide star variability, Galactic reddening and the host galaxy [2910 Å, ∼ 1.8 ks resolution].

possesses a band-pass that overlaps significantly with the UW2), but is essentially absent in the optical bands.

The next question is whether this change in optical/UV flux is accompanied by a change of spectral slope in the optical/UV. Previous analyses of the optical variability have found Fairall 9 to show peculiar spectral behavior in the UV/optical, not hardening when brightening (Recondo-Gonzalez et al., 1997; Santos-Lleo et al., 1997), as is observed in most sources (e.g., Vanden Berk et al., 2004). We therefore investigate whether our pure AGN fluxes show any signs for spectral variability between the optical and UV bands. Figure 5.4 shows the flux ratio between the

UW1-band flux and the V-band flux. Changes in color are clearly detected, with the UV/optical becoming harder when brighter, opposite to the trend observed in the X-ray band (Emmanoulopoulos et al., 2011). The average, measured power law slope during the monitoring was $1.33^{+0.02}_{-0.02}$. The steepest slope measured was $1.48^{+0.07}_{-0.06}$ and the flattest $1.25^{+0.06}_{-0.06}$. The average slope is substantially steeper than the average quasar slope determined by Davis, Woo & Blaes (2007) from the SDSS. While this discrepancy could generally be explained by intrinsic reddening, this is unlikely in case of Fairall 9 as Crenshaw & Kraemer (2001) determined from HST observations it does not possess intrinsic reddening. Our detection of color variation is, on the face of it, at odds with previous studies of this source (Recondo-Gonzalez et al., 1997; Santos-Lleo et al., 1997). The primary culprit appears to be the host galaxy subtraction. Santos-Lleo et al. (1997) essentially assumed that the AGN displayed achromatic variability and used this fact to define a galaxy subtraction. Our analysis appears to suggest that a more realistic galaxy subtraction does indeed result in AGN color changes.

The *XMM-Newton* data considered here give us a view of the UV variability of Fairall 9 on timescales of hours. As can be seen in Fig. 5.3 (bottom panel), the general trend seems to be a flux decline over the length of the observation ($\sim 1\,$day). However, there are a few short and small amplitude flares observed, the beginning of each is marked on Fig. 5.3 by a vertical line. These flares last approximately 10 ks ($\sim$ 3 hours) with an amplitude approximately 2–4% above the quiescent level, i.e., monochromatic flare luminosities of $\Delta L(2920\mathring{A}) = 1-2\times10^{39}\,\mathrm{erg\,s^{-1}}\,\mathring{A}^{-1}$ (although the first flare occurred just as the OM entered a short period of inoperation and may have been brighter).

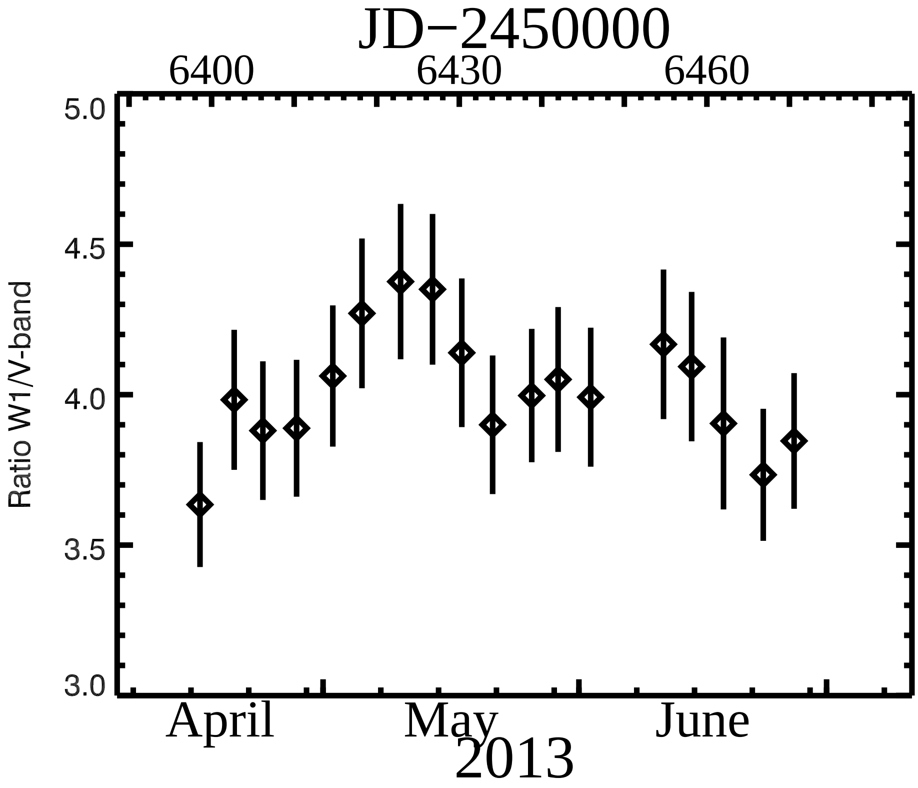

Figure 5.4: UV hardness evolution between the UW1 and V band during the *Swift* monitoring.

5.3.2 X-ray variability and the X-ray/UV connection

After investigating the UV variability we now turn to the X-ray variability of the source as well as the relationship between the X-ray and UV variability.

On the longer timescales probed by our *Swift* monitoring campaign, high amplitude X-ray variability (40%) is clearly seen in the 0.5–6 keV band (Figure 5.2, bottom panel). The general trend is a weak positive correlation between the UV and X-ray bands with a Pearson coefficient of 0.66 and a p-value of 0.002 (Fig. 5.5).

The value for the linear slope is 1.90 ± 0.37. Given the lack of a detailed correspondence between any given optical/UV lightcurve and the X-ray lightcurve, as well as the fact that this monitoring campaign only *just* probes down to the break in the power density spectrum ($f_b \approx 4 \times 10^{-7} \approx 1\,\mathrm{month}^{-1}$; Markowitz et al. (2003)) it is not possible to say from these data to what degree the 0.5–6 keV X-ray flux is truly related with the optical/UV band on these timescales.

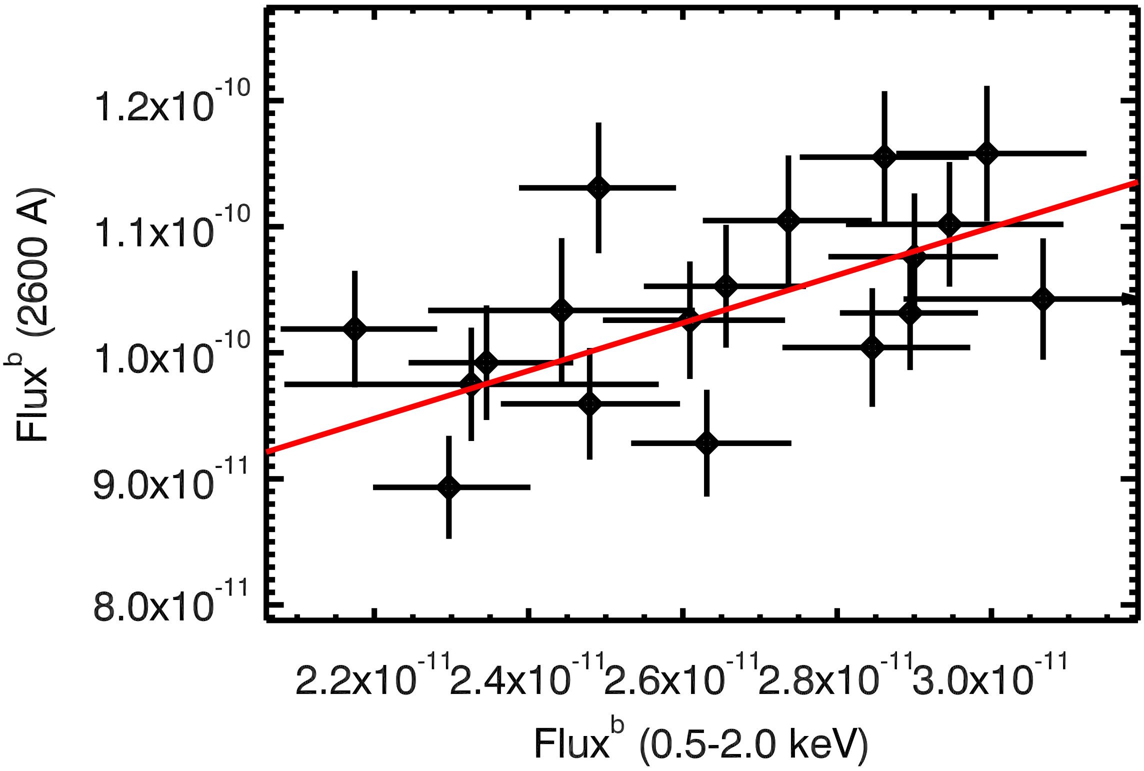

Figure 5.5: The soft, absorbed X-ray (0.5-2.0 keV) flux of Fairall 9 versus its de-reddened UV (2600 Å) flux, a positive correlation is apparent (Pearson coefficient: 0.66 , p-value: 0.002). The red solid line represents the best linear fit. ^{b}Flux in erg s^{-1} cm^{-2}.

As we discuss in more detail in Section 5.4, it is noteworthy that the strong UV-dip on 22-May-2013 is not reflected in the gross X-ray lightcurve. On the other hand, two weeks later (3-June-2013), there is a significant X-ray dip that has no correspondence in any of the optical or UV bands (unfortunately, the observing campaign was briefly interrupted in early June-2013 due to a higher-priority *Swift* target of opportunity, and hence we did not witness the egress from this X-ray dip).

However, the UV-dip may correspond to an X-ray spectral change. Each individual XRT pointing has insufficient counts for detailed spectroscopy, but a crude search for X-ray spectral variability can be conducted using hardness ratios. We choose to examine the ratio of the 0.5–2 keV and 2–5 keV fluxes (derived from the corresponding count spectra with a spectral model consisting of a power-law continuum modified by Galactic absorption, $N_H = 3.2 \times 10^{20}\,\mathrm{cm}^{-2}$). As shown in Fig. 5.6, the X-ray hardness ratio is approximately constant but there is marginal evidence for a rapid hardening at exactly the same time as the UV emission dips.

More rapid X-ray/UV connections can be explored using the *XMM* data. The X-ray variability within this pointing was already discussed in Emmanoulopoulos et al. (2011); they find a gradual softening of the X-ray spectrum, while the flux continuously increases. While there is generally little short term (hour-timescale) variability, we do see small flares that last approximately 2–4 ks with approximately 5% amplitude (Fig. 5.3). Interestingly, from examination of Fig. 5.3, we discover hints that the short-term flares are not random but it appears that the X-ray is leading the UV by 1-3 hours. The three most apparent flares are marked in the lightcurve in Fig. 5.3. To confirm this apparent time lag we calculate the Edelson & Krolik discrete correlation function (DCF) (Edelson & Krolik, 1988) for the *XMM*-pn and *XMM*-OM lightcurves after pre-whitening them with a second order

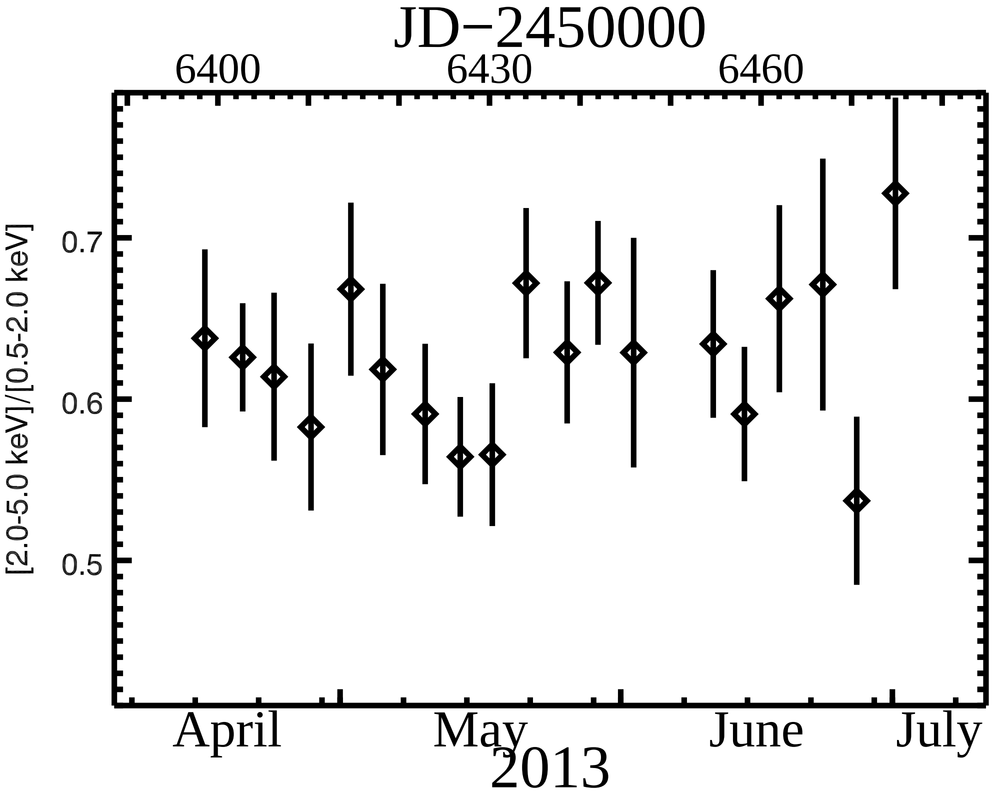

Figure 5.6: X-ray hardness evolution between the 2-5 keV flux and the 0.5-2 keV flux during the *Swift* monitoring.

polynomial (Welsh, 1999). The resulting DCF is shown Fig. 5.7, with $1\,\sigma$ and $2\,\sigma$ confidence levels estimated by model-independent Monte-Carlo simulations. With our interest being focused on the existence of correlations, we simulate 5000 DCFs to estimate the robustness of our potential lags, following these steps:

Step 1) Make a synthetic UV and X-ray lightcurve, by drawing, for each time stamp in the lightcurve, a flux/count rate value from a Gaussian distribution defined by the datapoint from the pre-whitened lightcurves as its mean and the errorbar as its sigma, Step 2) Randomize the values within each synthetic lightcurve but keep the time stamps fixed,

Step 3) Calculate the DCF between the two lightcurves using the same lag bin values as in the actual DCF,

Step 4) After repeating Steps 1-3 5000 times, estimate the confidence levels.

These simulations estimate the statistical errors on the DCF, as well as the strength of the correlations found, by comparing them to how likely it is to get correlations of such strength from randomized lightcurves. A positive lag in the Figure 5.7 means the UV is lagging behind the X-rays, i.e. the X-ray variations leading the UV variations. While there is no correlation or time lag detected with great confidence, we note, a peak at a UV lag time of about 1-2 hours and a potential anti-correlation on a 5 hour timescale. Both peaks are on the $2\,\sigma$ level.

5.4 Discussion

Our most curious finding is the existence and nature of the rapid UV variability. Here, we discuss the implications of these observations for our understanding of the UV continuum in this AGN.

In the standard picture, the optical/UV continuum is thermal (quasi-blackbody) radiation from the optically-thick accretion disk. Adopting the standard model for a geometrically-thin, radiatively-efficient, mass-conserving accretion disk by Shakura

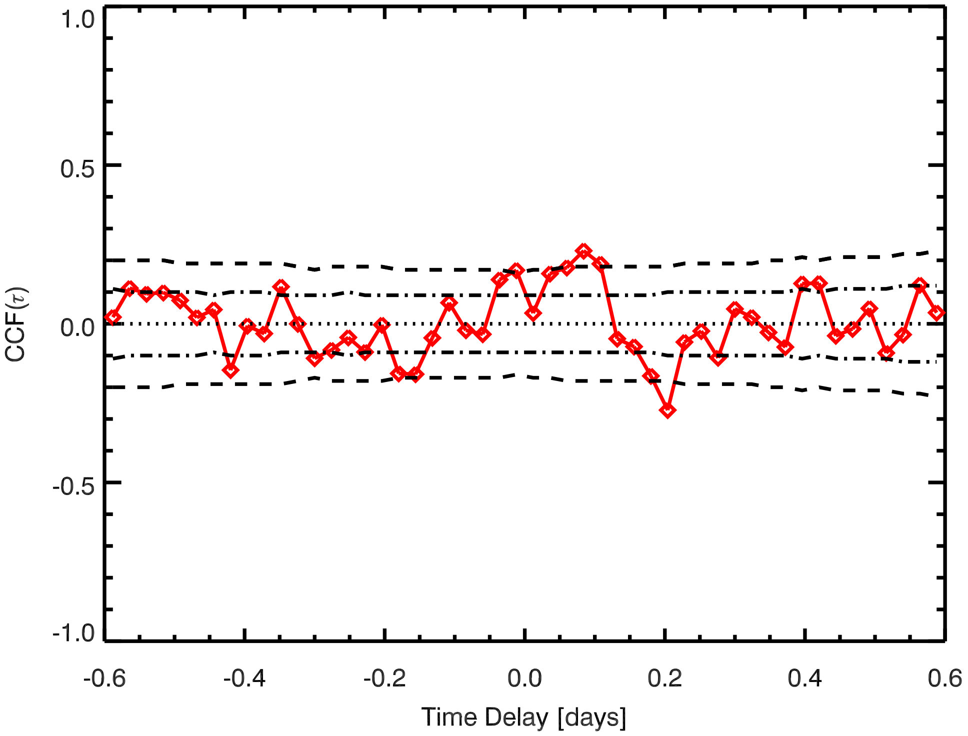

Figure 5.7: DCF for *XMM* X-ray and UV lightcurve (red line). The dot-dashed and dashed lines represent the $1\,\sigma$ and $2\,\sigma$ confidence limits, respectively. In the plot a peak at positive lag times indicates that the UV is lagging the X-rays by this time.

& Sunyaev (1973), the effective temperature profile is given by

$$T_{\text{eff}} = 1.08 \times 10^6\, \mathcal{L}^{1/4} M_8^{-1/4} \eta_{0.1}^{-1/4} r^{-3/4} f\, \text{K}, \tag{5.2}$$

where $\mathcal{L} = L/L_{\text{Edd}}$ is the Eddington ratio assuming a radiative efficiency of $\eta = 0.1\eta_{0.1}$, the black hole has mass $M = 10^8 M_8 M_\odot$, and r is the radius normalized to gravitational units, $r = R/R_g$, $R_g = GM/c^2$. We have also included a factor $f = [1 - (r_{\text{isco}}/r)^{1/2}]^{1/4}$ which encapsulates the affect of the zero-torque boundary condition at the innermost stable circular orbit, $r = r_{\text{isco}}$. Strictly, this form for the temperature profile becomes inaccurate in the innermost disk ($r \lesssim 10$) due to the emergence of relativistic corrections. For Fairall 9, we take $M_8 = 2.55$ (Peterson et al., 2004) and $\mathcal{L} = 0.15$ (Lohfink et al., 2012a) resulting in a temperature profile,

$$T_{\rm eff} = 5.3 \times 10^5 \eta_{0.1}^{-1/4} r^{-3/4} f\,{\rm K}. \tag{5.3}$$

The half-light radius of the thermal emission at some particular wavelength is determined by integrating the thermal emission outwards from the innermost radius of the disk (which we shall take to be $r = 6$). Employing the color-correction factors described by equations (1) and (2) of Done et al. (2012), we find that the half-light radius for the UW2-band emission (with central wavelength $\lambda = 1928$Å and corresponding blackbody temperature $T \approx 1.5 \times 10^4\,{\rm K}$) is $r_{1/2} \approx 52$. Similarly, the half-light radius of the B-band emission (with central wavelength $\lambda = 4392$Å and corresponding blackbody temperature $T \approx 6.6 \times 10^3\,{\rm K}$) is $r_{1/2} \approx 118$. The corresponding light crossing time of the UV (optical) region is $t_{\rm lc} = 2r_{1/2}/c \approx 1.5\,{\rm days}$ ($3.5\,{\rm days}$), the dynamical timescale is $t_{\rm dyn} \equiv (R^3/GM)^{1/2} = 5.5\,{\rm days}$ ($19\,{\rm days}$), the thermal timescale is $t_{\rm th} = t_{\rm dyn}/\alpha = 55\,{\rm days}$ ($190\,{\rm days}$) assuming a Shakura-Sunyaev viscosity parameter of $\alpha = 0.1$, and the viscous timescale is $t_{\rm visc} = t_{\rm th}/(h/r)^2 = 1.5 \times 10^3\,{\rm yr}$ ($5.2 \times 10^3\,{\rm yr}$) assuming a disk aspect ratio of $h/r = 0.01$. A summary of the properties of the optical emission region and the just calculated timescales can be found in Table 5.3.

From these timescales, we can immediately see that most UV variability reported in this chapter occurs on a surprisingly rapid timescale and cannot simply be attributed to accretion rate changes or thermal instabilities in the UV emit-

Table 5.3: Key properties of the optical UV/emission regions (for the B and UW2 band) and the corresponding charateristic timescales. A detailed explanation can be found in the text.

Filter Band	B	UW2
Center wavelength [Å]	4392	1928
Temperature [K]	6.6×10^3	1.5×10^4
Half light radius [r_g]	118	52
light crossing timescale [days]	3.5	1.5
dynamical timescale [days]	19	5.5
thermal timescale [days]	190	55
viscous timescale [years]	5.2×10^3	1.5×10^3

ting region of a standard disk. These possibilities are also unlikely considering the fractional variance of only 6 % (V-Band) to 11 % (W2-Band), implying that only a small part of the total UV/optical emission is actually variable. That a harder-when-brighter trend is still observed (as it is in our monitoring) even when the accretion rate is not the driver has already been noted by Ruan et al. (2014). With the nature of the variability being uncertain, the observed UV changes demand further discussion.

We will begin by addressing the UV variability observed in the *Swift* monitoring. The smooth variations seen in the UV are weakly correlated with the variations seen in the soft X-ray band. This correlation could be explained by two scenarios: either a reprocessing scenario where the X-rays are heating the disk and caused an increase in UV/optical emission; or by the upscattering of the UV/optical photons into X-ray band, as expected to produce the observed X-ray power law. Both scenarios would lead to a delay between the two bands, in case of Comptonization the

UV would be leading the X-ray variability while reprocessing would imply a lag of the UV behind the X-ray band. The shortness of the monitoring however prevents the measurement or even detection of any such delay.

The 4-day UV dip seen in our *Swift* monitoring requires special attention. As discussed in Section 5.3.1, this dip is seen strongly in the UV filters, but not in the optical bands or the (total) X-ray band. Given the strong wavelength dependence of dust extinction, an initially appealing hypothesis is an eclipse of the UV emitting region by a wisp of dusty gas in the circumnuclear environment. However, the short timescales are extremely problematic for this scenario. Given that the UV emitting region should be at least 3.5 light days in diameter, the wisp would need to be moving at relativistic speeds in order to block, and then unblock, the UV source on the observed timescales. Any dusty gas will be confined to beyond the sublimation radius, with corresponding velocities that are at least two orders of magnitude smaller. Thus, we conclude that the UV dip must correspond to a true decrease in the UV emission rather than an absorption event.

If we hold onto the notion that the UV emission has a thermal origin, we see that the observed UV variability occurs on the light crossing timescale. This immediately leads again to a picture whereby a significant fraction of the UV emission is reprocessed energy from the central most regions of the disk or the corona, and the dip corresponds to an abrupt decrease of incident emission from the central disk or corona. Since the X-ray emission remains rather steady during the dip, contrary to what is generally observed, there is no evidence that the central accretion disk emission actually shut off or the coronal emission decreased. Instead, it is possible that a slight change in geometry of the central disk (such as the creation of a transitory equatorial wind) resulted in the shielding of the UV emitting region from the central radiation field and thereby causing this particular type of variability.

The general, anti-correlated flux trends observed in the X-ray and the UV bands during the *XMM* pointing are consistent with reprocessing being the major driver of variability on the timescale of days to a week, as suggested by the *Swift* monitoring. This is because the pointing length of 91 ks ($\sim$ 1.05 days) is shorter than the expected delay between the two bands. Thermal reprocessing of X-ray emission in the disk has also recently been found to drive the short-term UV variability in NGC 4051 (Alston, Vaughan & Uttley, 2013) and PG 1211+143 (Bachev et al., 2009).

On the other hand the very rapid UV flares seen in the *XMM* data are enigmatic. Their rapid timescales and potential association with X-ray flares strongly argues that these UV flares originate from the centralmost regions of the around the black hole. Retaining the assumption that this is still thermal/quasi-blackbody emission, we can use the luminosity and duration of the flares to constrain the temperature of the emitting region. Consider a planar region of area πR^2 and temperature T observed at an angle θ. The monochromatic luminosity at wavelength λ is

$$L_\lambda = \frac{2\pi R^2 \cos\theta h c^2}{\lambda^5 (e^{hc/k_B T\lambda} - 1)}. \tag{5.4}$$

Thus, if we have a flare of amplitude ΔL_λ and duration Δt, we can use the fact that

$R < c\Delta t/\sin\theta$ to deduce that a causal flare requires

$$\Delta t > \left[\frac{\lambda^5 \Delta L_\lambda (e^{hc/k_B T\lambda} - 1)\sin^2\theta}{2\pi h c^4 \cos\theta}\right]^{1/2} . \tag{5.5}$$

Applying this constraint to the rapid UV flares in Fairall 9, we set $\lambda = 2910\text{Å}$, $\Delta t = 10\,\mathrm{ks}$, $\Delta L_\lambda = 2.2\times10^{39}\,\mathrm{erg\,s^{-1}\,Å^{-1}}$ (corresponding to $\Delta F_\lambda = 5\times10^{-16}\,\mathrm{erg\,s^{-1}\,cm^{-2}Å^{-1}}$ at a luminosity distance of 193 Mpc), and $\theta = 48°$ (Chapter 2). We conclude that the temperature of the flare region must be $T > 8 \times 10^4\,\mathrm{K}$. This is comparable to the expected disk temperatures within $r = 15$.

The timescales of these flares (comparable to the light crossing time of $10R_g$) again suggests a reprocessing model. At first sight, it is tempting to consider that the UV flares originate from heating of the central accretion disk by the observed X-ray micro-flares. Our tentative detection of a time delay between the X-ray flares and the UV flares could then be attributed to a reverberation delay provided that the X-ray source is only a few gravitational radii from the disk. However, the energetics of this picture need some consideration. Extrapolating across all wavelengths, the luminosity of the UV flares will be approximately $2 \times 10^{44}\,\mathrm{erg\,s^{-1}}$, peaking in the extreme-UV ($\lambda_{\mathrm{peak}} \approx 360\text{Å}$). On the other hand, the luminosity of the observed X-ray micro-flares is only $8\times10^{42}\,\mathrm{erg\,s^{-1}}$ even when extrapolated from 0.02–100 keV assuming a $\Gamma = 2$ powerlaw. Thus, the X-ray flare heating scenario for the UV flares requires either an additional and very strong soft ($< 0.3\,\mathrm{keV}$) component to the driving flare, and/or strong beaming of the flare emission towards the disk. Such beaming could result from relativistic streaming motions of plasma towards the disk in a magnetic flare-loop (Field & Rogers, 1993; Reynolds & Fabian, 1997) or gravitational light bending in the strong gravity of the black hole (Martocchia & Matt, 1996; Reynolds & Begelman, 1997; Miniutti & Fabian, 2004). Alternatively, a non-thermal origin is also a possibility for the observed microvariability.

The anti-correlation seen in the DCF with the X-rays leading the UV by about 5 hours is very puzzling. The only other reported anti-correlation has been found in NGC 7469 by Nandra et al. (1998) from a 30 day RXTE/IUE monitoring. The determined lag time was 4 days and most likely, if real, this can attributed to complex absorption in the source. With Fairall 9 being unobscured and the lag only 5 hours, this anti-correlation, if it can be substantiated with future observations, would pose serious questions to our current understanding of the geometry and processes in the vicinity of the black hole.

5.5 Conclusions

Using data from *Swift* and *XMM*, we have investigated the optical/UV variability of Fairall 9, and its connection to the X-ray band, over a range of timescales from hours to months. Our *Swift* monitoring finds significant correlated variability in all optical/UV bands with an amplitude that increases towards shorter wavelengths. We also find a correlation between the UV and X-ray lightcurves, although it is clear that the X-rays contain a significant component that is not coherent with the UV-band. In one particularly interesting event, the UW2-band flux is seen to dip by 20% between two pointings separated by just 4 days, and then recover back to its original level 4-days later. This dip is not seen in the optical filters or the total X-ray flux, although there is marginal evidence for an X-ray spectral hardening at the time of the dip. By considering characteristic timescales, we suggest that some significant fraction of the UV emission is reprocessed energy from the central regions of the disk and that the dip corresponds to a temporary shielding of the UV-emission region from the central radiation field.

On the shorter timescales probed by the *XMM* observations, we find rapid (10 ks) and low-amplitude (2–4%) UV-flares that may be associated with microflares seen in the X-ray flux. We use arguments based on the blackbody limit and causality to deduce that the region responsible for these flares must have a temperature of at least 8×10^4 K. We suggest that these UV-flares correspond to the heating of the centralmost parts of the disk by X-ray flares, although these possibility requires either a large EUV soft excess associated with the X-ray flares or strong beaming of the X-ray flare emission towards the accretion disk.

Chapter 6: Conclusions

This thesis explores the central regions of AGN using X-ray spectroscopy and variability studies. Our studies have provided us with some intriguing insights into both the physics of the central regions of AGN as well as the power of multi-epoch and multi-wavelength data.

6.1 Summary and Significance of Results

Chapters 2 and 3 highlight the importance of a unique spectral decomposition in the X-ray band and an explanation for the soft excess as a vital step when working towards understanding the processes taking place in the immediate vicinity of the black hole. Even with the best data available today, this remains challenging. Nevertheless, we were able to obtain dependable spectral decompositions for both Fairall 9 and 3C120 with archival data by using all available CCD data and applying consistency checks. In Chapter 2 we show, for Fairall 9, compelling evidence for an additional soft Comptonization component which extends from the optical/UV into soft X-ray band can be found. Similar results have been obtained for Mrk 509 (Mehdipour et al., 2011) and are hinted at in other cases (Noda et al., 2013; Matt et al., 2014). However, it remains unclear today whether the soft excess is a universal feature of AGN spectra and, if so, whether it is always produced by the same physical mechanism(s).

In Chapter 3, we have presented an analysis of 3C120 strongly supporting the current idea of jet formation, which links the ejection of a new jet knot to a disturbance of the inner parts of the accretion disk. During the *Suzaku* observation the accretion was found to be disrupted within $\sim 38\,R_{\rm g}$. The black hole spin was also determined to be high (with a formal result of $a > 0.99$ although this weakens to $a > 0.95$ when we consider realistic departures from the theoretical assumptions underlying the analysis), suggesting that the rotational energy of the black hole could be used to power the prominent jet in 3C120. Results such as these help anchor the numerical simulations of astrophysical jets and are another step towards understanding AGN feedback.

The findings of Chapters 4 and 5 illustrate how variability studies can significantly contribute to our understanding of the interplay of the different AGN components. The 4–7 day long X-ray dips discovered in Fairall 9 are indicative of variability on very short timescales, especially when considering the high black hole mass of $2.55 \times 10^8\,M_\odot$ (Peterson et al., 2004). Such variability is hard to explain, as most possibilities are ruled out by the speed and strength of the dips.

Chapter 5 outlined the analysis of the UV/X-ray variability in the source confirms the commonly accepted idea that X-ray reprocessing is dominating the fast timescale variability at optical/UV wavelengths (Ulrich, Maraschi, & Urry, 1997). However, a complete understanding can only be reached when the driving X-ray variability is understood. The speed of the microvariability suggests it could be connected to changes in the corona. As the cooling of the corona is thought to be regulated by radiation, i.e. the optical disk emission entering the corona (which contradicts the observations that the X-ray leads the variations), heating could be the driver. Although our understanding of coronal heating is incomplete, it is mostly accepted today that magnetic fields play a crucial role in it (e.g., Di Matteo, 1998). If in fact there is coronal heating on fast timescales, this would suggest that NuSTAR will detect changes in the coronal temperature on these timescales. As of today, such changes are yet to be discovered.

6.2 Brief Outlook

This thesis has helped to improve our understanding of the central regions of AGN. Many questions however remain open, such as:

- Why do powerful jets only appear in some sources?
- Do all AGN possess a soft X-ray excess?
- What are the properties of an AGN corona? What is its geometry?
- What is the origin of the rapid UV variability?

Finding answers to these questions will be the subject of future studies. As already seen in this thesis studying the broad-band spectra of AGN can be a useful tool. The NuSTAR satellite now allows us to measure AGN spectra with great accuracy from single pointing observations up to 50-70 keV. Combining these with soft X-ray observations provides an excellent view of the X-ray band. Although still in the early days, AGN science is already benefiting from this new possibilities (Risaliti et al., 2013; Brenneman et al., 2014; Matt et al., 2014). For example Brenneman et al. (2014) are able to obtain tight constraints on the coronal parameters ($kT_e = 37^{+7}_{-6}\,\mathrm{keV}$, $\tau = 1.25^{+0.20}_{-0.10}$) for a slab geometry from a joint *Suzaku* and *NuSTAR* observation. As we have seen in Chapters 3 and 5 folding in data from other wavelengths can also be of tremendous help, allowing clear choices were the X-ray spectral data alone are ambiguous. One particularly intriguing possibility will be to use the UV/optical detectors on board of *Swift* and *XMM* alongside their X-ray spectra and *NuSTAR*. The UV/optical could then help to constrain the Comptonization models better by putting constraints on the seed photon distribution. The result will be one of the possibly best views of the AGN continuum thoughout the X-ray band. A robust understanding of the X-ray continuum will be crucial to deduce the maximum information from the high resolution spectra becoming available with the launch of *Astro-H* in 2015. These superior *Astro-H* spectra will provide stringent constraints on outflows and their place in AGN feedback.

Bibliography

Ackermann, M., et al., 2011, ApJ, 743, 171

Abdo, A. A., & Fermi/LAT Collaboration, 2009, ApJ, 707, 142

Agudo, I., Gómez, J.-L., Martí, J.-M., Ibáñez, J.-M., Marscher, A. P., Alberdi, A., Aloy, M.-A., Hardee, P. E. 2001, ApJ, 549, L183

Agudo, I., Gómez, J. L., Casadio, C., Cawthorne, T. V., & Roca-Sogorb, M., 2012, ApJ, 752, 92

Alston, W. N., Vaughan, S., & Uttley, P., 2013, MNRAS, 429, 75

Antonucci, R., 1993, ARA&A, 31, 473

Antonucci, R. R. J. and Miller, J. S., 1985, ApJ, 297, 621

Arav, N., Barlow, T. A., Laor, A., & Blandford, R. D., 1997, MNRAS, 288, 1015

Arévalo, P., Uttley, P., Lira, P., Breedt, E., McHardy, I. M., & Churazov, E., 2009, MNRAS, 397, 2004

Arnaud, K. A., 1996, in Astronomical Data Analysis Software and Systems V, ed. G. H. Jacoby & J. Barnes, Vol. 101, 17

Arnaud, K., Smith, R., & Siemiginowska, A., 2011, Handbook of X-ray Astronomy, Cambridge University Press, Cambridge, UK

Bachev, R., Grupe, D., Boeva, S., Ovcharov, E., Valcheva, A., Semkov, E., Georgiev, T., & Gallo, L. C., 2009, MNRAS, 399, 750

Barthel, P. D., ApJ, 1989, 336, 606

Beckmann, V., Courvoisier, T. J.-L., Gehrels, N., Lubiński, P., Malzac, J., Petrucci, P.-O., Shrader, C. R., & Soldi, S., 2008, A&A, 492, 93

Ballantyne, D. R., Fabian, A. C., & Iwasawa, K., 2004, MNRAS, 354, 839

Bardeen, J. M., Petterson, & J. A., 1975, ApJ, 195, 65

Belloni, T. M., 2010, in Lecture Notes in Physics, Berlin Springer Verlag, Vol. 794, 53

Beloborodov, A. M., 1999, ApJ, 510, 123

Bentz, M. C., Peterson, B. M., Netzer, H., Pogge, R. W., & Vestergaard, M., 2009, ApJ, 697, 160

Best, P. N., Kauffmann, G., Heckman, T. M., Brinchmann, J., Charlot, S., Ivezić, Ž., & White, S. D. M., 2005, MNRAS, 362, 25

Blandford, R. D., & Znajek, R. L., 1977, MNRAS, 179, 433

Blandford, R. D., & Payne, D. G., 1982, MNRAS, 199, 883

Bower, R. G., Benson, A. J., Malbon, R., Helly, J. C., Frenk, C. S., Baugh, C. M., Cole, S., & Lacey, C. G., 2006, MNRAS, 370, 645

Breedt, E., et al., 2009, MNRAS, 394, 427

Brenneman, L. W., & Reynolds, C. S., 2006, ApJ, 652, 1028

Brenneman, L. W., et al., 2011, ApJ, 736, 103

Brenneman, L. W., et al., 2014, ApJ, 781, 83

Cackett, E. M., Zoghbi, A., Reynolds, C., Fabian, A. C., Kara, E., Uttley, P., & Wilkins, D. R., 2014, MNRAS, 438, 2980

Cameron, D. T., McHardy, I., Dwelly, T., Breedt, E., Uttley, P., Lira, P., & Arevalo, P., 2012, MNRAS, 422, 902

Cardelli, J. A., Clayton, G. C., & Mathis, J. S., 1989, ApJ, 345, 245

Chartas, G., Kochanek, C. S., Dai, X., Poindexter, S., & Garmire, G., 2009, ApJ, 693, 174

Chatterjee, R., et al., 2011, ApJ, 734, 43

Chatterjee, R., et al., 2009, ApJ, 704, 1689

Chiang, J., Reynolds, C. S., Blaes, O. M., Nowak, M. A., Murray, N., Madejski, G., Marshall, H. L., & Magdziarz, P., 2000, ApJ, 528, 292

Corbel, S., Coriat, M., Brocksopp, C., Tzioumis, A. K., Fender, R. P., Tomsick, J. A., Buxton, M. M., & Bailyn, C. D., 2013, MNRAS, 428, 2500

Cowperthwaite, P. S., & Reynolds, C. S., 2012, ApJ, 752, 21

Crenshaw, D. M., & Kraemer, S. B., 2001, ApJ, 562, L29

Croft, S., et al., 2006, ApJ, 647, 1040

Croton, D. J., et al., 2006, MNRAS, 365, 11

Crummy, J., Fabian, A.C., Gallo, L., & Ross, R.R, 2006, MNRAS, 365, 1067

Daly, R. A., & Marscher, A. P. 1988, ApJ, 334, 539

Dauser, T., Wilms, J., Reynolds, C. S., & Brenneman, L. W., 2010, MNRAS, 409, 1534

Davis, S. W., Woo, J.-H., & Blaes, O. M., 2007, ApJ, 668, 682

De Marco, B., Ponti, G., Cappi, M., Dadina, M., Uttley, P., Cackett, E. M., Fabian, A. C., & Miniutti, G., 2013, MNRAS, 431, 2441

de Rosa, A., et al., P., 2012, MNRAS, 420, 2087

Dewangan, G. C., Griffiths, R. E., Dasgupta, S., & Rao, A. R., 2007, ApJ, 671, 1284

Di Matteo, T., 1998, MNRAS, 299, 15

Done, C., Davis, S. W., Jin, C., Blaes, O., & Ward, M., 2012, MNRAS, 420, 1848

Dove, J. B., Wilms, J., Maisack, M., & Begelman, M. C., 1997, ApJ, 487, 759

Dugan, Z., Bryan, S., Gaibler, V., Silk, J., & Haas, M., 2014, ArXiv e-prints

Edelson, R. A., & Krolik, J. H., 1988, ApJ, 333, 646

Edwards, A. C., 1980, MNRAS, 190, 757

Elvis, M., Wilkes, B. J., & Lockman, F. J., 1989, AJ, 97, 777

Emmanoulopoulos, D., Papadakis, I. E., McHardy, I. M., Nicastro, F., Bianchi, S., & Arévalo, P., 2011, MNRAS, 415, 1895

Emmanoulopoulos, D., McHardy, I. M., & Papadakis, I. E., 2011, MNRAS, 416, 94

Fabian, A. C., Rees, M. J., Stella, L., & White, N. E., 1989, MNRAS, 238, 729

Fabian, A. C., Nandra, K., Reynolds, C. S., Brandt, W. N., Otani, C., Tanaka, Y., Inoue, H., & Iwasawa, K., 1995, MNRAS, 277, 11

Fabian, A. C., et al., 2009, Nature, 459, 540

Fabian, A. C., et al., 2011, MNRAS, 418, 2154

Fabian, A. C., et al., 2012, MNRAS, 424, 217

Fabian, A. C., 2013, ARA&A, 50, 455

Fabian, A. C., et al., 2013, MNRAS, 429, 2917

Fender, R. P., Belloni, T. M., & Gallo, E., 2004, MNRAS, 355, 1105

Fender, R., Koerding, E., Belloni, T., Uttley, P., McHardy, I., & Tzioumis, T., 2007, ArXiv e-prints

Fender, R. P., Homan, J.,& Belloni, T. M., 2009, MNRAS, 396,1370

Feruglio, C., Maiolino, R., Piconcelli, E., Menci, N., Aussel, H., Lamastra, A., & Fiore, F., 2010, A&A, 518, 155

Field, G. B., & Rogers, R. D., 1993, ApJ, 403, 94

Gallo, E., Fender, R., Kaiser, C., Russell, D., Morganti, R., Oosterloo, T., & Heinz, S., 2005, Nature, 436, 819

Gallo, E., 2007, in The Multicolored Landscape of Compact Objects and Their Explosive Origins, ed. T. di Salvo, G. L. Israel, L. Piersant, L. Burderi, G. Matt, A. Tornambe, & M. T. Menna, Vol. 924, 715

Gallo, L. C., Miniutti, G., Miller, J. M., Brenneman, L. W., Fabian, A. C., Guainazzi, M., & Reynolds, C. S., 2010, MNRAS, 1686

García, J., Dauser, T., Reynolds, C., Kallman, T., Wilms, J., & McClintock, J., 2012, X-ray Reflected Spectra from Accretion Disks: The Impact of Ionization Gradients, Energetic Astronomy Conference

García, J., Dauser, T., Reynolds, C. S., Kallman, T. R., McClintock, J. E., Wilms, J., & Eikmann, W., 2013, ApJ, 768, 146

García-Lorenzo, B., Sánchez, S. F., Mediavilla, E., González-Serrano, J. I., & Christensen, L., 2005, ApJ, 621, 146

Gaskell, C. M., & Klimek, E. S., 2003, Astronomical and Astrophysical Transactions, 22, 661

George, I. M., & Fabian, A. C., 1991, MNRAS, 249, 352

George, I. M., Turner, T. J., Netzer, H., Nandra, K., Mushotzky, R. F., & Yaqoob, T., 1998, ApJS, 114, 73

Gierliński M., Done C., 2004, MNRAS, 349, 7

Gliozzi, M., Papadakis, I. E., Grupe, D., Brinkmann, W. P., & Räth, C., 2013, MNRAS, 433, 1709

Gofford, J., et al., 2011, MNRAS, 414, 3307

Gómez, J. L., Martí, J. M., Marscher, A. P., Ibáñez, J. M., & Alberdi, A. 1997, ApJ, 482, 33

Gondoin, P., Lumb, D., Siddiqui, H., Guainazzi, M., & Schartel, N., 2001, A&A, 373, 805

Groves, B. A., Heckman, T. M., & Kauffmann, G., 2006, MNRAS, 371, 1559

Grupe, D., Komossa, S., Scharwächter, J., Dietrich, M., Leighly, K. M., Lucy, A., & Barlow, B. N., 2013, AJ, 146, 78

Guainazzi, M., Bianchi, S., Matt, G., Dadina, M., Kaastra, J., Malzac, J., & Risaliti, G., 2010, MNRAS, 406, 2013

Haardt, F., & Maraschi, L., 1991, ApJ, 380, 51

Heisler, C. A., Lumsden, S. L., & Bailey, J. A., 1997, Nature, 385, 700

Higginbottom, N., Proga, D., Knigge, C., Long, K. S., Matthews, J. H., & Sim, S. A., 2014, ArXiv e-prints

Ho, L. C., & Ulvestad, J. S., 2001, ApJS, 133, 77

Houck, J. C., & Denicola, L. A., 2000, in Astronomical Data Analysis Software and Systems IX, ed. N. Manset, C. Veillet, & D. Crabtree, Vol. 216, 591

Jorstad, S. G., et al. 2005, AJ, 130, 1418

Jorstad, S. G., et al. 2010, ApJ, 715, 362

Kalberla, P. M. W., Burton, W. B., Hartmann, D., Arnal, E. M., Bajaja, E., Morras, R., & Pöppel, W. G. L., 2005, A&A, 440, 775

Kallman, T., & Mushotzky, R., 1985, ApJ, 292, 49

Kara, E., Fabian, A. C., Cackett, E. M., Uttley, P., Wilkins, D. R., & Zoghbi, A., 2013, MNRAS, 434, 1129

Kataoka, J., et al., 2007, PASJ, 59, 279

Kataoka, J., et al., 2011, ApJ, 740, 29

Kellermann, K. I., Sramek, R., Schmidt, M., Shaffer, D. B., & Green, R., 1989, AJ, 98, 1195

King, A. R., Pringle, J. E., West, R. G., & Livio, M., 2004, MNRAS, 348, 111

King, A. L., et al., 2011, ApJ, 729, 19

Kinney, A. L., Calzetti, D., Bohlin, R. C., McQuade, K., Storchi-Bergmann, T., & Schmitt, H. R., 1996, ApJ, 467, 38

Komatsu, E., et al., 2011, ApJS, 192, 18

Korista, K. T., & Goad, M. R., 2000, ApJ, 536, 284

Kormendy J., Gebhardt K., 2001, In: Wheeler J.C., Martel H. (eds.) 20th Texas Symposium on relativistic astrophysics, Vol. 586. American Institute of Physics Conference Series, p.363

Koyama, K., et al., 2007, PASJ, 59, 23

Laor, A., Barth, A. J., Ho, L. C., & Filippenko, A. V., 2006, ApJ, 636, 83

Livio, M., Pringle, J. E., & King, A. R., 2003, ApJ, 593, 184

Lohfink, A. M., Reynolds, C. S., Mushotzky, R. F., & Wilms, J., 2012a, ApJ, 749, 31

Lohfink, A. M., Reynolds, C. S., Miller, J. M., Brenneman, L. W., Mushotzky, R. F., Nowak, M. A., & Fabian, A. C., 2012b, ApJ, 758, 67

Lohfink, A. M., et al., 2013, ApJ, 772, 83

Magdziarz, P., & Zdziarski, A. A., 1995, MNRAS, 273, 837

Maiolino, R., et al., 2010, A&A, 517, A47

Maoz, D., Markowitz, A., Edelson, R., & Nandra, K., 2002, AJ, 124, 1988

Marconi, A., Risaliti, G., Gilli, R., Hunt, L. K., Maiolino, R., & Salvati, M., 2004, MNRAS, 351, 169

Markoff, S., Nowak, M. A., & Wilms, J., 2005, ApJ, 635, 1203

Markowitz, A., & Edelson, R., 2001, ApJ, 547, 684

Markowitz, A., et al., 2003, ApJ, 593, 96

Maraschi, L., Chiappetti, L., Falomo, R., Garilli, B., Malkan, M., Tagliaferri, G., Tanzi, E. G., & Treves, A., 1991, ApJ, 368, 138

Marscher, A. P., Jorstad, S. G., Gómez, J.-L., Aller, M. F., Teräsranta, H., Lister, M. L., & Stirling, A. M., 2002, Nature, 417, 625

Marshall, H. L., et al., 1997, ApJ, 479, 222

Marshall, K., Ryle, W. T., Miller, H. R., Marscher, A. P., Jorstad, S. G., Chicka, B., & McHardy, I. M., 2009, ApJ, 696, 601

Martocchia, A., & Matt, G., 1996, MNRAS, 282, L53

Matt, G., et al., 2014, MNRAS, 439, 3016

McHardy, I. M., Koerding, E., Knigge, C., Uttley, P., Fender, R. P., 2006, Nature, 444, 730

McKinney, J. C., & Blandford, R. D., 2009, MNRAS, 394, 126

Mehdipour, M. et al., 2011, A&A, 534, 39

McKinney, J. C., Tchekhovskoy, A., & Blandford, R. D., 2012, MNRAS, 423, 3083

Merloni, A., Heinz, S., di Matteo, T., 2003, MNRAS, 345, 1057

Miller, J. M., 2007, ARA&A, 45, 441

Miller, J. M., Reynolds, C. S., Fabian, A. C., Miniutti, G., & Gallo, L. C., 2009, ApJ, 697, 900

Miller, L., Turner, T. J., & Reeves, J. N., 2008, A&A, 483, 437

Miller, L., & Turner, T. J., 2013, ApJ, 773, 5

Miller-Jones, J. C. A., et al., 2012, MNRAS, 421, 468

Miniutti, G., & Fabian, A. C., 2004, MNRAS, 349, 1435

Miniutti, G., Panessa, F., de Rosa, A., Fabian, A. C., Malizia, A., Molina, M., Miller, J. M., & Vaughan, S., 2009, MNRAS, 398, 255

Mirabel, I. F., & Rodríguez, L. F., 1999, ARA&A, 37, 409

Molina, M., Bassani, L., Malizia, A., Stephen, J. B., Bird, A. J., Bazzano, A., & Ubertini, P., 2013, MNRAS, 433, 1687

Mor, R., Netzer, H., & Elitzur, M., 2009, ApJ, 705, 298

Moran, E. C., Barth, A. J., Kay, L. E., & Filippenko, A. V., 2000, ApJ, 540, 73

Murray, N., Quataert, E.,& Thompson, T. A., 2005, ApJ, 618, 569

Mushotzky, R. F., Fabian, A. C., Iwasawa, K., Kunieda, H., Matsuoka, M., Nandra, K., & Tanaka, Y., 1995, MNRAS, 272, 9

Nagao, T., Maiolino, R., & Marconi, A., 2006, A&A, 459, 85

Nandra, K., George, I. M., Mushotzky, R. F., Turner, T. J., & Yaqoob, T., 1997, ApJ, 477, 602

Nandra, K., Clavel, J., Edelson, R. A., George, I. M., Malkan, M. A., Mushotzky, R. F., Peterson, B. M., & Turner, T. J., 1998, ApJ, 505, 594

Nandra, K., O'Neill, P. M., George, I. M., & Reeves, J. N., 2007, MNRAS, 382, 194

Nardini, E., Fabian, A. C., Reis, R. C., & Walton, D. J., 2011, MNRAS, 410, 1251

Nenkova, M., Sirocky, M. M., Nikutta, R., Ivezić, Ž., & Elitzur, M., 2008, ApJ, 685, 160

Noda, H., Makishima, K., Yamada, S., Torii, S., Sakurai, S., & Nakazawa, K., 2011, PASJ, 63, 925

Noda, H., Makishima, K., Nakazawa, K., Uchiyama, H., Yamada, S., & Sakurai, S., 2013, PASJ, 65, 4

Nowak, M. A., et al., 2011, ApJ, 728, 13

O'Brien, P. T., & Leighly, K. M., 1998, Advances in Space Research, 21, 67

O'Donnell, J. E., 1994, ApJ, 422, 158

Ogle, P. M., Davis, S. W., Antonucci, R. R. J., Colbert, J. W., Malkan, M. A., Page, M. J., Sasseen, T. P., & Tornikoski, M., 2005, ApJ, 618, 139

Papadakis I.E., et al., 2010, A&A, 510, 65

Patrick, A. R., Reeves, J. N., Porquet, D., Markowitz, A. G., Lobban, A. P., & Terashima, Y., 2011, MNRAS, 411, 2353

Penston, M. V., 1988, MNRAS, 233, 601

Perola, G. C., Matt, G., Cappi, M., Fiore, F., Guainazzi, M., Maraschi, L., Petrucci, P. O., & Piro, L., 2002, A&A, 389, 802

Peterson, B. M., et al., 2004, ApJ, 613, 682

Peterson, B. M., 2006, The Broad Line Region, Lecture Notes in Physics, Berlin Springer Verlag, 693, 77

Petrucci, P.-O., et al., 2013, A&A, 549, 73

Poutanen, J., & Svensson, R., 1996, ApJ, 470, 249

Pozo Nuñez, F., Ramolla, M., Westhues, C., Bruckmann, C., Haas, M., Chini, R., Steenbrugge, K., & Murphy, M., 2012, A&A, 545, 84

Rafferty, D. A., McNamara, B. R., Nulsen, P. E. J., Wise, M. W., 2006, ApJ, 652, 216

Recondo-Gonzalez, M. C., Wamsteker, W., Clavel, J., Rodriguez-Pascual, P. M., Vio, R., Ting-Gui, W., Santos-Lleo, M., & Makino, F., 1997, A&AS, 121, 461

Reis, R. C., & Miller, J. M., 2013, ApJ, 769, 7

Remillard, R. A. & McClintock, J. E., 2006, ARA&A, 44, 49

Reeves, J. N., Nandra, K., George, I. M., Pounds, K. A., Turner, T. J., & Yaqoob, T., 2004, ApJ, 602, 648

Reynolds, C. S., 1997, MNRAS, 286, 513

Reynolds, C. S., & Begelman, M. C., 1997, ApJ, 488, 109

Reynolds, C. S., & Fabian, A. C., 1997, MNRAS, 290, 1

Reynolds, C. S., & Nowak, M. A., 2003, Phys. Rep., 377, 389

Reynolds, C. S., Garofalo, D., & Begelman, M. C., 2006, ApJ, 651, 1023

Reynolds, C. S., & Fabian, A. C., 2008, ApJ, 675, 1048

Reynolds, C. S., Fabian, A. C., Brenneman, L. W., Miniutti, G., Uttley, P., & Gallo, L. C., 2009, MNRAS, 397, 21

Reynolds, C. S., Brenneman, L. W., Lohfink, A. M., Trippe, M. L., Miller, J. M., Fabian, A. C., & Nowak, M. A., 2012, ApJ, 755, 88

Risaliti, G., Nardini, E., Salvati, M., Elvis, M., Fabbiano, G., Maiolino, R., Pietrini, P., & Torricelli-Ciamponi, G., 2011, MNRAS, 410, 1027

Risaliti, G, et al., 2013, Nature, 494, 449

Rodriguez-Pascual, P. M., et al., 1997, ApJS, 110, 9

Rivers, E., Markowitz, A., & Rothschild, R., 2011, ApJS, 193, 3

Ross R.R., et al., 1992, MNRAS 258, 189

Ross, R. R., & Fabian, A. C., 2005, MNRAS, 358, 211

Ruan, J. J., Anderson, S. F., Dexter, J., & Agol, E., 2014, ApJ, 783, 105

Rybicki, G. B., & Lightman, A. P., 1979, Radiative processes in astrophysics, New York, Wiley-Interscience

Santos-Lleo, M., et al., 1997, ApJS, 112, 271

Schlegel, D. J., Finkbeiner, D. P., & Davis, M., 1998, ApJ, 500, 525

Schmoll, S., et al., 2009, ApJ, 703, 2171

Shakura, N. I., & Sunyaev, R. A., 1973, A&A, 24, 337

Silk J.,& Rees M.J., 1998, A&A, 331, 1

Silk J., 2013, ApJ, 772, 112

Singh, V., Shastri, P., & Risaliti, G., 2011, A&A, 532, 84

Smith, R., & Vaughan, S., 2007, MNRAS, 375, 1479

Snedden, S. A., & Gaskell, C. M., 2007, ApJ, 669, 126

Sturm, E., et al., 2011, ApJ, 733, 16

Takahashi, T., et al., 2007, PASJ, 59, 35

Tanaka, Y., et al., 1995, Nature, 375, 659

Tanaka, Y., & Shibazaki, N., 1996, ARA&A, 34, 607

Tatum, M. M., Turner, T. J., Sim, S. A., Miller, L., Reeves, J. N., Patrick, A. R., & Long, K. S., 2012, ApJ, 752, 94

Thorne, K. S., 1974, ApJ, 191, 507

Titarchuk, L., 1994, ApJ, 434, 570

Tombesi, F., Sambruna, R. M., Reeves, J. N., Reynolds, C. S., & Braito, V., 2011, MNRAS, 418, 89

Tombesi, F., Sambruna, R. M., Marscher, A. P., Jorstad, S. G., Reynolds, C. S., & Markowitz, A., 2012, MNRAS, 424, 754

Peng, Y.-j., et al., 2010, ApJ, 721, 193

Sobolewska, M. A., & Papadakis, I. E., 2009, MNRAS, 399, 1597

Ulrich, M.-H., Maraschi, L., & Urry, C. M., 1997, ARA&A, 35, 445

Uttley, P., McHardy, I. M., & Vaughan, S., 2005, MNRAS, 359, 345

Urry, C. M., & Padovani, P., 1995, PASP, 107, 803

Vanden Berk, D. E., et al, 2004, ApJ, 601, 692

Vasudevan, R., & Fabian, A.C., 2009, MNRAS, 392, 1124

Veilleux, S., Cecil, G.,& Bland-Hawthorn, J., 2005, ARA&A 43, 769

Volonteri, M., 2010, A&A Rev., 18, 279

Volonteri, M., Sikora, M., Lasota, J.-P., & Merloni, A., 2013, ApJ, 775, 94

Warner, C., Hamann, F., & Dietrich, M., 2004, ApJ, 608, 136

Welsh, W. F., 1999, PASP, 111, 1347

Whittle, M., 1992, ApJS, 79, 49

Wilms, J., Allen, A., & McCray, R., 2000, ApJ, 542, 914

Wilms, J., Nowak, M. A., Pottschmidt, K., Pooley, G. G., & Fritz, S., 2006, A&A, 447, 245

Zoghbi, A., Reynolds, C., Cackett, E. M., Miniutti, G., Kara, E., & Fabian, A. C., 2013, ApJ, 767, 121